Targeted Gene Delivery to Astrocytes Using Intelligent Phagemid-Assembled Gene Expression (iPhAGE) Technology for Neuronal Regeneration

by

Anna Ffrench

A thesis

presented to the University of Waterloo

in fulfilment of the

thesis requirement for the degree of

Master of Science

in

Pharmacy

Waterloo, Ontario, Canada, 2026

© Anna Ffrench 2026

AUTHOR'S DECLARATION

This thesis consists of material all of which I authored or co-authored: see Statement of Contributions included in the thesis. This is a true copy of the thesis, including any required final revisions, as accepted by my examiners.

I understand that my thesis may be made electronically available to the public

STATEMENT OF CONTRIBUTIONS

Rohini Prakash and Julia Lumini contributed to the design of the precursor constructs used for miniphagemid production, and Rohini Prakash, together with Deborah Pushparajah, provided some positive control plasmids. Assistance with select agarose gel electrophoresis experiments for restriction digest analysis was provided by Kate Nagge, co-op student in the Slavcev Lab. Assistance with select agarose gel electrophoresis experiments for restriction digest analysis, miniphagemid production and characterization through spot plate, MADLS and OD were provided by Max Chiao, co-op student in the Slavcev Lab.

Immature neuronal cultures were provided by James Livingstone, and neural stem cell derived astrocyte cultures were provided by Kartar Singh and Adam Falah from the Beazely Lab. These cultures were used as experimental inputs for downstream analyses conducted by the author. Assistance with harvesting cells for protein extraction, performing western blots, and interpreting the results was provided by Mehraveh Hossainali, James Livingstone, and Kartar Singh.

All other experimental procedures, including miniphagemid production, cell culture experiments, data acquisition, data analysis, interpretation of results, and preparation of the written thesis were performed by the author. Any omissions are unintentional, and the author is grateful to all individuals who contributed to this work.

ABSTRACT

Neurodegenerative diseases, stroke, and brain injuries lead to progressive neuronal loss, with limited treatment options focused mainly on symptom management rather than regeneration. A major challenge in developing effective therapies is the lack of safe and efficient gene delivery systems capable of targeting cells in the central nervous system. This project addresses this gap by developing a novel gene therapy approach using the Intelligent Phagemid-Assembled Gene Expression (iPhAGE) platform, an innovative bacteriophage-based system designed to deliver reprogramming transcription factors to astrocytes. The iPhAGE system, derived from M13 miniphagemids, offers high transfection efficiency, large cargo capacity, low immunogenicity, and blood-brain barrier permeability**,** making it an ideal tool for targeted gene delivery. This research involves constructing plasmids carrying the *NeuroD1* gene under astrocyte-specific and universal promoters, producing and characterizing miniphagemids, and evaluating their transfection efficiency in resting and activated A7 cells**.** Neuronal reprogramming is assessed through PSA-NCAM neuronal marker analysis, a marker associated with early neuronal differentiation used to evaluate phenotypic changes following NeuroD1 delivery. Key methodologies include designing and validating precursor and helper plasmids, producing miniphagemids, and characterizing them using restriction digestion, MADLS, and transfection assays. The outcome of this project was the establishment and initial evaluation of the iPhAGE-based gene delivery framework for astrocyte-to-neuron reprogramming. This work assesses main components of the iPhAGE system, including vector construction, miniphagemid production, and astrocyte reprogramming using neuronal markers, therefore establishing a groundwork for future optimization.

ACKNOWLEDGEMENTS

I would like to express my sincere gratitude to my supervisor for their guidance, support, and encouragement throughout the course of this research. Their insight and expertise were invaluable in shaping this work. I greatly appreciate the contributions of my committee members for their constructive feedback and thoughtful suggestions. I am also thankful to the select members of my lab for their collaboration, helpful discussions, and ongoing support. Finally, I would like to thank my family and friends for their support and encouragement throughout my academic journey.

TABLE OF CONTENTS

AUTHOR'S DECLARATION ..... *ii*

STATEMENT OF CONTRIBUTIONS ..... *iii*

ABSTRACT ..... *iv*

ACKNOWLEDGEMENTS ..... *v*

LIST OF TABLES ..... *xi*

LIST OF FIGURES ..... *xii*

TABLE OF ABBREVIATIONS ..... *xv*

TABLE OF SYMBOLS ..... *xx*

1. Introduction *1*

1.0 Perspective **1**

1.1 Molecular Biology of Astrocytes and Neurons **2**

1.1.1 Cell Fate Specification in the Developing CNS 2

1.1.2 Astrocytes 3

1.1.3 NeuroD1 Transcription Factor as a Reprogramming Agent 6

1.1.4 Neurons 7

1.1.5 Reprogrammed Neurons 7

1.2 Challenges and Advances in Gene Therapy for CNS Disorders **9**

1.2.1 Gene Therapy Approaches and Delivery Challenges 11

1.3 Bacteriophage-Based Gene Therapy as an Alternative **13**

1.3.1 Bacteriophages as Therapeutic Non-Viral Vectors 13

1.3.2 Filamentous M13 Bacteriophage for CNS Therapeutic Applications 14

1.3.3 Use of Filamentous Bacteriophages in Gene Therapy 17

1.3.4 Limitations and Challenges of Filamentous Bacteriophages in Gene Therapy 19

1.4 Intelligent Phagemid-Assembled Gene Expression (iPhAGE) Technology 20

2. Rationale, Hypothesis & Objectives 24

2.1 Rationale 24

2.2 Hypothesis 25

2.3 Objectives 26

3. Materials and Methods 27

3.1 Construct Design and Validation 27

3.1.1 Construction of the Precursor Plasmids 29

3.1.2 Construction of the Helper Plasmids 34

3.1.3 Restriction Digest Analysis of Plasmid Constructs 39

3.1.4 Co-Transformation of Competent *E. coli* Cells by Precursor and Helper Plasmids 40

3.1.5 Miniphagemid Production and Purification 41

3.1.6 Dot Blot Analysis for Miniphagemids 45

3.1.7 Purification of the Single-Stranded Miniphagemid DNA 46

3.1.8 Quantifying Miniphagemids via Multi-Angle Dynamic Light Scattering 46

3.1.9 Quantifying Miniphagemids via OD 48

3.1.10 Assessing Miniphagemid Backbone DNA Contamination 48

3.2 Assessment of Gene Delivery Efficiency and Targeting Specificity of Miniphagemid Vectors 51

3.2.1 Maintaining Immortalized Cell Lines 51
3.2.2 Astrocyte Differentiation and Maintenance 53
3.2.3 Cell Transfection with Precursor Constructs 54
3.2.4 Activation of A7 Cells.....57
3.2.5 Transfection of Cells by Miniphagemids 61
3.2.6 Assessing Cell Viability 62
3.3 Evaluate Astrocyte Differentiation into Neurons Using Neuronal Marker PSA-NCAM 63
3.4 Statistical Analysis.....65
***4. Results and Discussion*.....66**
4.1 Objective #1: Design, Construct and Characterise Miniphagemid Vectors Carrying *NeuroD1* Transcription Factor, Tissue-Specific Promoter, and Targeting Peptides.....66
4.1.1 Plasmid Sequence Verification 66
4.1.2 Immunoblot Analysis for Miniphagemids 68
4.1.3 Purification of the single-stranded Miniphagemid DNA 71
4.1.4 Quantifying Miniphagemids via Multi-Angle Dynamic Light Scattering and UV–Visible Spectrophotometry.....74
4.1.5 Assessing Backbone Contamination via Colony Assay.....77
4.1.6 Summary of Results for Objective 1: Design, Construct and Characterise Miniphagemid Vectors Carrying *NeuroD1* Transcription Factor, Tissue-Specific Promoter, and Targeting Peptides. 80

4.2 Objective #2: Assess the Gene Delivery Efficiency to Target Cells by Quantifying Reporter Gene Activity. 81

4.2.1 Transfection of A7 Astrocyte Cells with Plasmids Containing Transcription Factor Genes for Astrocyte Reprogramming 81

4.2.2 Assessing DNA Uptake by A7 Cells During Transfection 85

4.2.3 Assessing Activation of A7 Cells Through Morphological Changes 88

4.2.4 Assessing Activation of A7 Cells via Western Blot 92

4.2.5 Assessing Transfection Efficiency in Reactive A7 Cells with Miniphagemids 94

4.2.6 Assessing Cell Viability After Miniphagemid Treatment 102

4.2.7 Summary of Results for Objective 2: Assess the Gene Delivery Efficiency to Target Cells by Quantifying Reporter Gene Activity. 104

4.3 Objective #3: Evaluate the Ability of *NeuroD1* Constructs to Initiate Astrocyte-to-Neuron Reprogramming 105

4.3.1 Assessing Transfection Efficiency in Astrocytes 105

4.3.2 Detection of PSA-NCAM Proteins of Reprogrammed Astrocytes 106

4.3.3 Summary of Results for Objective 3: Evaluate the Ability of *NeuroD1* Constructs to Initiate Astrocyte-to-Neuron Reprogramming. 109

5. Future Directions 110

5.1 Future Miniphagemid Purification and Characterization Steps 110

5.2 Assessing Endotoxin Levels in Miniphagemids 111

5.3 Optimizing Miniphagemids for Enhanced BBB Penetration 113

5.4 Further Assessing Astrocytes Reprogramming into Neurons 113

6. Summary and Significance *115*

References *116*

Appendix A: Media and Buffer Compositions *132*

Appendix B: Restriction Digestion Enzymes *135*

Appendix C: Phage Display Sequences *136*

Appendix D: Supplementary AGE Data *137*

D-1 Restriction Digest Analysis of Plasmid Constructs **137**

D-2 Additional Restriction Digest on Precursor and Helper Constructs **145**

D-3 Extraction of the Double-Stranded Plasmid DNA from the *E. coli* Pellet **147**

Appendix E: Assessing DNA Uptake by A7 Cells During Transfection Through PI Staining *156*

LIST OF TABLES

Table 1: Key Features of Viral and Non-Viral Gene Therapy Vectors 12

Table 2: Summary of M13 Bacteriophage Protein Functions 16

Table 3: Plasmids Used in This Project 27

Table 4: Miniphagemids Produced in This Project 28

Table 5: Bacterial Strains Used in This Project 39

Table 6: Design and Components of iPhAGE Miniphagemid Constructs 43

Table 7: Summary of Mammalian Cell Lines Used in This Project 51

Table 8: Plasmid DNA Sequence Local Alignment Scores 67

Table 9: Expected Sizes of Miniphagemid Genomes 71

Table 10: Miniphagemid Size and Concentration Estimated Using MADLS 76

Table 11: Contamination Efficiency of Miniphagemids Based on the Colony Assay 79

Table 12: Summary of Post-hoc Pairwise Chi-square Tests 90

Table 13: Summary of Restriction Enzymes 135

Table 14: Expected Fragment Sizes from Double Restriction Digest of Plasmids 138

LIST OF FIGURES

Figure 1: Structure of Bacteriophage M13 17

Figure 2: Workflow for M13 Miniphagemid Characterization 23

Figure 3: Overview of Astrocyte Reprogramming Using iPhAGE Technology 25

Figure 4: Miniphagemid Precursor Plasmid Constructs 34

Figure 5: Miniphagemid Helper Plasmids Constructs 37

Figure 6: p326, EF-1α-dTomato and pM13ori2-cmv-luc Plasmids 38

Figure 7: Production of *NeuroD1*-encoding M13 Miniphagemids from Precursor and Helper Plasmids 42

Figure 8: Dot Blot on Miniphagemids Staining for EGF Display and M13 Capsid Protein pIII 70

Figure 9: Agarose Gel Electrophoresis of Extracted Single-Stranded DNA from All Produced Miniphagemids 73

Figure 10: Visualizing *GFP* and *dTomato* Expression in A7 Cells Transfected with Precursor Plasmids 82

Figure 11: Percentage of Fluorescent Marker-Positive A7 Cells 83

Figure 12: Firefly Luciferase Reporter Activity in A7 Cells 84

Figure 13: DNA Uptake and Reporter Gene Expression in A365 and A7 Cells 87

Figure 14: A7 Cells Treated with LPS at 24 h 89

Figure 15: Effect of LPS Treatment on Circularity of A7 Cells 89

Figure 16: Effect of LPS Treatment on A7 Cell Size 91

Figure 17: Levels of GFAP Protein in A7 Cells Following LPS Treatment 93

Figure 18: dTomato Signal in Reactive vs Resting A7 Cells and A375 Cells Infected with Miniphagemids 96

Figure 19: Luciferase Signal in Reactive vs Resting A7 Cells and A375 Cells Infected with Miniphagemids 98
Figure 20: A7 Cells Treated with LuNe Miniphagemids 100
Figure 21: Assessment of A7 Cell Viability Following Miniphagemid Treatments 103
Figure 22: *GFP* Expression in NSC Derived Astrocytes 106
Figure 23: PSA-NCAM Receptors on Astrocytes and Neurons 106
Figure 24: PSA-NCAM Ab Binding in Immature Neurons 107
Figure 25: PSA-NCAM Ab Signal in NSC-Derived Astrocytes at Day 7 and 14 Post-Transfection 108
Figure 26: Quantification of Endotoxin in Miniphagemid Samples Using Chromogenic Assay 112
Figure 27: Agarose Gel of Restriction Digest of AI Plasmid DNA for Verification 139
Figure 28: Agarose Gel of Restriction Digest of JL Plasmid DNA for Verification 140
Figure 29: Agarose Gel of Restriction Digest of Flex Switch and pLuNe Plasmid DNA for Verification 141
Figure 30: Agarose Gel of Restriction Digest of SW8-EGF and SW8-IRL1620 Plasmid DNA for Verification 142
Figure 31: Agarose Gel of Restriction Digest of SW8-SF, SW8-SG, SW8-SL, and SW8-EGFSF Plasmid DNA for Verification 143
Figure 32: Agarose Gel of Restriction Digest of SW8-EGF Plasmid DNA for Plasmid Verification 145
Figure 33: Agarose Gel of Restriction Digest of AI Plasmids DNA for Plasmid Verification ... 146
Figure 34: Agarose Gel of Restriction Digest of AI with SW8-EGF Plasmid DNA from Miniphagemid Production 148

Figure 35: Agarose Gel of Restriction Digest of JL with SW8-EGF Plasmid DNA from Miniphagemid Production 149
Figure 36: Agarose Gel of Restriction Digest of JL with SW8-IRL1620 Plasmid DNA from Miniphagemid Production 150
Figure 37: Agarose Gel of Restriction Digest of Flex Switch with SW8-EGF and Flex Switch with SW8-IRL1620 Plasmid DNA for Miniphagemid Production 151
Figure 38: Agarose Gel of Restriction Digest of JL with SW8-SF, SW8-SG and SW8-SL Plasmid DNA for Miniphagemid Production 153
Figure 39: Agarose Gel of Restriction Digest of JL and SW8-EGFSF Plasmid DNA for Miniphagemid Production 154
Figure 40: Agarose Gel of Restriction Digest of pLuNe with SW8-SF, SW8-SG, and SW8-SL Plasmid DNA for Miniphagemid Production 155
Figure 41: Assessing DNA Uptake by A7 Cells Through PI-Staining 157

TABLE OF ABBREVIATIONS

AAV	Adeno-Associated Virus
Ab	Antibody
AD	Alzheimer's Disease
AGE	Agarose Gel Electrophoresis
AGS	Astrocyte Growth Supplement
AM	Astrocyte Media
Amp	Ampicillin
APC	Allophycocyanin
APS	Ammonium Persulfate
BBB	Blood Brain Barrier
BCA	Bicinchoninic Acid
BDNF	Brain-Derived Neurotrophic Factor
bHLH	Basic Helix-Loop-Helix
bp	Base Pair
BSA	Bovine Serum Albumin
CFU	Colony Forming Unit
CMV	Cytomegalovirus
CNS	Central Nervous System
CpG	Cytosine-Guanine Dinucleotide
CpG-DNA	DNA Containing Unmethylated CpG Patterns
CRISPR	Clustered Regularly Interspaced Short Palindromic Repeats

DALYs	Disability-Adjusted Life Years
DNA	Deoxyribonucleic Acid
DMEM	Dulbecco's Modified Eagle's Medium
dsDNA	Double-stranded DNA
E. coli	*Escherichia coli*
EF-1α	Elongation Factor-1 alpha
EGF	Epidermal Growth Factor
EGFR	Epidermal Growth Factor Receptor
EGR	Early Growth Response Protein
ETBR	Endothelin B Receptor
EU	Endotoxin Units
FBS	Fetal Bovine Serum
FDA	Food and Drug Administration
Ff	F Specific Filamentous
FGF2	Fibroblast Growth Factor
FITC	Fluorescein Isothiocyanate
FM	Fei Mao
Fndc3c1	Fibronectin type III domain-containing 3C1
FSC	Forward Scatter
GFAP	Glial Fibrillary Acidic Protein
GFP	Green Fluorescent Protein
HD	Huntington's Disease
HFV	Human Foamy Virus

HRP	Horseradish Peroxidase
ICC	Immunocytochemistry
IHC	Immunohistochemistry
iPhAGE	Intelligent Phagemid-Assembled Gene Expression
IR	Intergenic Region
Kan	Kanamycin
LAL	Limulus Amebocyte Lysate
LB	Luria-Bertani
LPS	Lipopolysaccharides
MADLS	Multi-Angle Dynamic Light Scattering
MEAs	Multi-Electrode Arrays
MOI	Multiplicity of Infection
mRNA	Messenger Ribonucleic Acid
NC	Negative Control
NDD	Neurodegenerative Diseases
NeuroD1	Neurogenic Differentiation Factor 1
NPM	Neural Progenitor Media
NSCs	Neural Stem Cells
NTFs	Neurotrophic Factors
NT-3	Neurotrophin-3
OD	Optical Density
OR	Olfactory Receptor
OXPHOS	Oxidative Phosphorylation System

PBS	Phosphate-Buffered Saline
PC	Positive Control
PD	Parkinson's Disease
PDI	Polydispersity Index
PE	Phycoerythrin
PEG	Polyethylene Glycol
PI	Propidium Iodide
PS	Packaging Signal
PSA-NCAM	Polysialylated Neuronal Cell Adhesion Molecule
qPCR	Quantitative Polymerase Chain Reaction
RE	Restriction Enzyme
RF DNA	Replicative Form DNA
RLU	Relative Luminescence Units
RNA	Ribonucleic Acid
ROS	Reactive Oxygen Species
rpm	Revolutions Per Minute
SDS	Sodium Dodecyl Sulfate
SEC	Size Exclusion Chromatography
ssDNA	Single-stranded DNA
Sseq	SuperSequences
Ssh	Sonic hedgehog
SUP	Super High Accuracy
TAE	Tris-Acetate-EDTA

TBS-T	Tris-Buffered Saline with Tween 20
TEMED	N,N,N′,N′-Tetramethylethylenediamine
TN	Tris-NaCl
TRITC	Tetramethylrhodamine
tPA	Tissue Plasminogen Activator
TTV	Torque Teno Virus
UTR	Untranslated Region
VP	Viral Particles

TABLE OF SYMBOLS

D	Diffusion coefficient
kB	Boltzmann constant
T	Temperature in Kelvin
η	Viscosity of the fluid
r	Radius of the particle
A_{269}	Absorbance at 269 nm
A_{320}	Absorbance at 320 nm
α	Alpha level
ρ	p-value
X^2	Chi-square

1. Introduction

1.0 Perspective

Neurons and astrocytes are two of the most critical cell types in the brain, with neurons responsible for transmitting information throughout the nervous system [1] and astrocytes providing structural and metabolic support to neurons [2].

In 2026 over 3 billion people worldwide are living with a neurological condition, making it the leading cause of disability globally. Disability-adjusted life years (DALYs) caused by these conditions have increased by 18% since 1990 [3]. Notably, more than 80% of neurological deaths and health losses occur in low- and middle-income countries, where access to treatment is significantly lower compared to high-income countries [3]. There is an urgent need for targeted interventions to provide cost effective quality care, treatment, and rehabilitation for the growing number of people with neurological conditions.

Neurodegenerative diseases (NDDs) such as Alzheimer's (AD), Parkinson's (PD), and Huntington's (HD) diseases are characterised by the progressive loss of neurons, initially in specific regions, and later spreading throughout the central nervous system (CNS). This neuronal loss leads to a range of devastating clinical outcomes such as memory loss, and cognitive or functional decline, greatly impacting the lives of affected individuals and their families [4]. Despite the increase in neurodegenerative diseases, current therapeutic methods are mostly limited to symptom management and do not address the loss of neurons, highlighting a gap in safe and scalable regenerative treatments. Therefore, there is a need for innovative, non-invasive strategies to regenerate lost neurons and restore neural function in patients. The Intelligent Phagemid-Assembled Gene Expression (iPhAGE) system presents a novel approach to overcoming these challenges. Derived from M13 filamentous bacteriophages, iPhAGE enables the targeted delivery of reprogramming transcription factors to astrocytes, reprogramming them into neurons. Unlike

viral vectors, iPhAGE offers low immunogenicity, high cargo capacity, and efficient penetration of the BBB, allowing for safe and effective gene delivery [5]. Additionally, iPhAGE eliminates bacterial backbone sequences, reducing the risk of insertional mutagenesis and immune activation, which are major concerns in gene therapy.

Therefore, this project focused on the establishment and evaluation of an iPhAGE based gene delivery approach for astrocyte to neuron reprogramming. While a fully functional reprogramming system was not achieved within the scope of this study, the work represents an important step in identifying key technical challenges and critical parameters requiring optimization. Addressing these limitations in future studies may enable successful astrocyte reprogramming and support the development of iPhAGE-based strategies for neural repair, offering a scalable, minimally invasive approach with the potential to advance regenerative medicine for currently incurable neurological conditions.

1.1 Molecular Biology of Astrocytes and Neurons

1.1.1 Cell Fate Specification in the Developing CNS

The cellular diversity of the CNS arises from neural stem cells (NSCs) that originate as neuroepithelial cells within the neural tube. During development, these NSCs transition into radial glial cells, which serve as the primary progenitor cells for neurons and macroglia, including astrocytes and oligodendrocytes. In early development, these radial glial cells divide to produce neuronal cells, later shifting toward glial cell generation [6,7]. This transition is known as the gliogenic switch, it marks the change from neurogenesis to gliogenesis [8]. This process is triggered by the downregulation of proneural factors such as neurogenins, which suppress gliogenesis during early stages of development [6]. Whether a neural stem cell stays a stem cell or turns into a specific

brain cell is controlled by helix-loop-helix (bHLH) transcription factors. When these proteins (such as Ascl1, Hes1, and Olig2) are cycling on and off, the cell stays in an immature state. When one of these proteins is turned on continuously, the cell commits to becoming a specific type of brain cell.

Neurons are typically the first cell type generated from NSCs, with sustained expression of the Ascl1 transcription factor that promotes neuronal differentiation [7,8]. As development progresses, more cells become glial cells, with oligodendrocyte formation influenced by Sonic hedgehog (Shh) signaling, which activates expression of the transcription factors Olig1 and Olig2 [6].

Following the completion of neurogenesis, radial glial cells begin differentiating into astrocytes. This process is guided by external signals and cytokines that activate the JAK–STAT signaling pathway, leading to the expression of astrocyte-specific genes such as *GFAP*, while transcription factors such as NFIA, NFIB, and SOX9 further support astrocyte development [6]. In contrast, microglia do not arise from neural stem cells. Instead, they originate from extra-embryonic mesodermal progenitors that migrate into the CNS early in embryonic development [8].

1.1.2 Astrocytes

Astrocytes are star-shaped glial cells which are one of the most functionally diverse and abundant groups of mammalian brain cells. In humans, astrocytes outnumber neurons and make up 25% to 50% of the tissue volume in some areas of the brain [9]. Astrocytes are essential for the CNS function due to their ability to offer a diverse range of supporting activities to neurons such as guiding them through development, providing nutritional and metabolic support to neurons throughout life, regulating synaptic activity and immune responses, recycling of neurotransmitters, maintaining selective permeability of the BBB, as well as aiding in higher cognitive functions, involving learning and memory [10].

Due to their star-shaped structure and multiple processes, astrocytes can simultaneously interact with numerous neurons and blood vessels. The terminating processes of astrocytes, endfeet, surround neurons and blood vessels and are essential for BBB function and nutrition transfer [9]. The intermediate filaments that make up the astrocytic cytoskeleton, like glial fibrillary acidic protein (GFAP), offer structural support and are commonly used as markers of astrocyte activation [9].

Astrocytes play a key role in various CNS disorders. Abnormal astrocyte functions after stroke or injury can affect neuron survival. They also influence neurite growth, synaptic plasticity, and neuron regeneration by releasing trophic factors and expressing surface molecules. After brain injury, astrocytes can become reactive, which may lead to both helpful and harmful effects, such as neuroinflammation [11].

It is possible to directly reprogram human astrocytes into neurons through the introduction of specific transcription factors, such as NeuroD1. In contrast, astrocytes can also be converted into neural stem cells (NSCs), which can subsequently differentiate into multiple neural cell types. Direct reprogramming does not require a pluripotent or stem cell stage, thereby reducing the risk of tumor formation or immune rejection [12]. The goal of reprogramming astrocytes is to produce cells that exhibit characteristics similar to native neurons, including the ability to differentiate into neuronal subtypes.

Male and female astrocytes show distinct genetic and functional characteristics shaped by sex chromosomes and hormonal signaling, leading to differences in gene expression, intracellular signaling, and responses to CNS injury [13]. These differences are particularly relevant during neuroinflammation, as reactive astrocytes are the primary cell population targeted for astrocyte-to-neuron reprogramming. Male and female astrocytes activate different gene programs, respond differently to inflammatory signals, use distinct intracellular pathways such as calcium signaling,

and may remain in reactive states for different lengths of time following injury [13]. As a result, male astrocytes often exhibit stronger or more persistent inflammatory and stress-related responses, whereas female astrocytes tend to show more controlled or hormone-modulated activation [14]. Hormonal factors such as estrogen can dampen inflammatory signaling in female astrocytes, while differences in chromosomal composition and cellular metabolism may prime male astrocytes toward prolonged reactivity [15]. This means that astrocytes targeted for reprogramming may exist in different baseline molecular states, even following the same injury.

Because NeuroD1 functions by activating neuronal gene programs while suppressing astrocytic identity genes, astrocytes that remain highly inflamed, strongly express markers such as GFAP, and actively engage immune signaling pathways may present greater resistance to lineage conversion [16]. Consequently, reprogramming may be slower, less efficient, or incomplete in strongly reactive astrocytes [17]. Studies suggest that male astrocytes may remain reactive for longer periods following inflammatory triggers, while female astrocytes may resolve inflammation more rapidly depending on the hormonal environment, potentially leading to sex-dependent differences in reprogramming efficiency, neuronal maturation, and subtype specification [14].

Reprogramming astrocytes into neurons offers a promising strategy for addressing neuronal loss in neurodegenerative diseases by potentially restoring neural circuits and improving functional outcomes, thereby addressing limitations of current therapies [18]. In addition to generating new neurons, astrocyte reprogramming may also reduce the harmful effects of chronically reactive astrocytes, including prolonged inflammation and astrocyte hypertrophy. By shifting astrocytes away from detrimental reactive states, this approach could improve the local brain environment while further supporting neural circuit repair [18].

Given their abundance, functional versatility, and capacity to respond to injury, astrocytes represent an accessible and promising target for reprogramming into neurons [9]. Their ability to be

converted via transcription factors such as NeuroD1, without the stem cell stage, reduces risks associated with tumor formation or immune rejection [12]. Collectively, these features make astrocytes an ideal target for regeneration of neural circuits as a therapy for neurodegenerative diseases.

1.1.3 NeuroD1 Transcription Factor as a Reprogramming Agent

NeuroD1 is a basic helix–loop–helix (bHLH) transcription factor that plays a central role in neuronal differentiation during development. It binds to E-box motifs (CANNTG) in the promoters and enhancers of neuronal genes, directly activating transcription programs that define neuronal identity [19,20]. Key target genes include those involved in neuronal cytoskeleton organization, synaptic formation, and neurotransmitter machinery, promoting a switch from a glial to a neuronal transcriptional profile. In addition to activating neuronal genes, NeuroD1 indirectly suppresses glial-specific gene expression, facilitating exit from the astrocytic program and promoting a neuron-like phenotype [21,22].

Astrocytes are particularly receptive to NeuroD1-mediated reprogramming because of their shared developmental origin with neurons and the accessibility of neuronal gene loci in their chromatin landscape. When *NeuroD1* is ectopically expressed in astrocytes, it binds neuronal gene regulatory regions, recruits co-activators, and remodels chromatin to initiate neuronal gene expression, while simultaneously downregulating glial genes. This dual action effectively converts astrocytes into functional neuron-like cells without passing through a pluripotent or stem cell intermediate, reducing risks associated with tumor formation or uncontrolled proliferation [23,24].

NeuroD1 was chosen for this study over other transcription factors such as Ascl1 or Ngn2 because it has been shown to efficiently induce glutamatergic neuronal fate in human astrocytes and has a robust ability to activate late neuronal gene networks required for synaptic maturation.

Unlike Ascl1, which often generates immature neurons or requires combinatorial TF expression, NeuroD1 alone is sufficient in many contexts to initiate both early and late neuronal programs [24]. These properties make it a suitable candidate for evaluating astrocyte-to-neuron reprogramming using targeted gene delivery systems like iPhAGE.

1.1.4 Neurons

Neurons are the primary signaling cells in the CNS; they are responsible for transmitting signals throughout the body via electrical and chemical signals. They communicate with each other and effector organs via synapse, a process where neurotransmitters are released at neuroeffector junctions to propagate signals. Neuronal communication happens through the propagation of electrical signals via ion movement across the membranes [1]. Proper neuronal function is critical for cognition, movement, and overall brain function. Neurons consist of a cell body known as soma that has dendrites and an axon extending from it. Dendrites are long projections that receive afferent signals while axon propagates efferent signals by releasing neurotransmitters at the terminal [1].

In the adult brain, the full set of neurons is formed during embryonic development, and mature neurons do not undergo division. However, neurogenesis where new neurons are integrated into already existing neural circuits can occur in certain regions of the brain. This process is limited to the olfactory bulb and the dentate gyrus of the hippocampus. In these areas, new neurons can be produced from neural stem cells that can self-renew and differentiate into neurons and glial cells when exposed to signals resembling the ones occurring during normal development [25].

1.1.5 Reprogrammed Neurons

Reprogrammed neurons are neurons that have been created through the conversion of non-neuronal cells into mature neurons [26]. In this project, astrocyte cells are being reprogrammed into

neuron cells as a potential treatment of neurodegenerative diseases. However, it also raises some questions regarding the functional and physiological characteristics of new neurons compared to the naturally-developed ones.

Previously it has been shown that reprogrammed neurons are able to express neuron-specific genes, form synapses, and generate action potential [27,28]. However, it is still unclear whether they are able to fully integrate into the existing neural circuits [29]. Natural neurons generate complex connections based on genetic signals and environmental inputs over long periods of time during brain development [30]. Reprogrammed neurons, on the other hand, could skip some elements of typical neurodevelopment since they are being artificially created in a post-developmental environment [31]. Therefore, one of the main obstacles to neural reprogramming in vivo is figuring out how to produce the right neuronal subtypes and properly integrate them into preexisting circuits [32]. For now, it is still unclear whether regenerated neurons can reconstruct brain networks and recover lost function, largely due to the difficulty in producing fully functional target neurons and specific neuronal subtypes, as neurosuppressive factors released by surrounding glial and immune cells can inhibit the development of newly formed neurons [32].

Another significant obstacle for this method is generating sufficient neurons. For treating different diseases, the quantity of live neurons is crucial, but equally important is their spatial arrangement and coordinated activity with neighbouring cells. Neurons must not only survive but also properly position themselves and form functional connections within existing circuits to restore meaningful neural activity [33]. It was shown in a prior clinical trial involving fetal tissue transplantation that PD treatment required about 100,000 surviving dopaminergic cells; however, the effectiveness also depended on how well these neurons integrated into the existing circuit. Therefore, reprogramming efficiency needs to be maximized to generate a sufficient number of neurons capable of cooperating with native cells [32].

It is important to be able to assess the functional integrity of developing neurons, therefore it would be helpful to establish an assessment system. The evaluation metric can test synapse formation with other neurons, functionality of sodium and potassium ion transport, and the creation of a local circuit with electrodes [32].

1.2 Challenges and Advances in Gene Therapy for CNS Disorders

Gene therapy is the introduction of engineered genetic material into cells to alter their gene expression and treat disease. The first successful gene therapy procedure in humans was conducted in 1990, targeting a severe combined immunodeficiency disorder. Subsequently, gene therapy has shown immense potential to treat previously untreatable diseases, but decades of clinical trials have revealed serious limitations, including treatment-related deaths and tumor formation, which continue to challenge its safe and effective implementation [34,35].

Stable integration of genetic material into host cells and targeted distribution to other host cells or tissues are necessary for successful gene delivery [36]. Current gene therapy techniques face several challenges, including safety concerns such as immunogenicity or genotoxicity. There is a concern that performing gene therapy can trigger immune responses posing a risk to the patient and therefore reducing the effectiveness and safety of the treatment. Other challenges faced by gene therapy limiting this treatment include excessive costs, complex product production, variability in outcomes observed in patients, as well as transitioning from development to widespread clinical use and scalability. Additionally, current gene delivery systems lack control over patient dosing, limiting their potential for universal use [37], as many patients previously exposed to viral vectors are excluded from treatment due to pre-existing immunity, which affects roughly 40% of the population [38,39]. Gene expression system, therapeutic gene, and delivery vector are the three primary parts of gene delivery systems [36]. These challenges are more pronounced in

the CNS, where the BBB restricts access, cell turnover is limited, and neural tissue is highly sensitive to immune-mediated toxicity. In CNS applications, immune responses are particularly concerning due to the limited regenerative capacity of neural tissue and the potential for irreversible neurological damage [40].

Gene delivery systems can be broadly categorized into viral and non-viral vectors. Viral vectors use customised mammalian viruses to deliver genes to host cells, while non-viral vectors use physical and chemical methods to deliver genes without using mammalian viruses [36]. Non-viral vectors, such as polymers and polysaccharides, have safety advantages such as low immunogenicity as well as no restriction on the size of DNA inserts, and ease of manufacturing. However, non-viral vectors generally suffer from low transfection efficiency and poor transgene expression. Simpler versions of nonviral complexes may also be immunogenic and limited in redosability potential. Improved nonviral vectors are possible and many nucleic acid minivectors have been produced and dramatically improve immunogenic profile but are expensive to manufacture and often suffer from fidelity issues. Conversely, viral vectors, such as adenoviruses, provide high transfection efficiencies since they are biological gene delivery systems; they can also target specific tissues, integrate chromosomes at specified sites, and effectively infect both dividing and non-dividing cells over an extended period. However, viral vectors pose risks such as immunogenicity and insertional mutagenesis, which have been clinically associated with adverse immune reactions, reduced treatment durability, and, in some cases, the development of malignancies [41,35]. Table 1 summarizes the features of viral and non-viral vectors, comparing the two types.

1.2.1 Gene Therapy Approaches and Delivery Challenges

Gene therapy has been explored using both viral and non-viral delivery systems, each offering distinct advantages and limitations. Viral vectors are generally associated with high transduction efficiency but raise concerns related to immunogenicity, insertional mutagenesis, limited cargo capacity, and patient exclusion due to pre-existing immunity. Non-viral systems offer improved safety profiles and manufacturing flexibility but typically suffer from low delivery efficiency, particularly in post-mitotic tissues such as the central nervous system (CNS). While these platforms have been extensively reviewed, their application in the CNS presents unique challenges that have limited clinical translation [36].

Non-viral vectors refer to delivery systems that do not rely on human viruses. Non-viral gene delivery systems include two main classes: physical methods and chemical methods. Physical methods involve the use of physical forces to introduce genetic material into cells. Some of the examples of physical mechanisms for gene delivery are direct injection via needle, ballistic DNA injection by forcing gold coated DNA into cells, electroporation that creates pores in cell membranes using electrical pulses, sonoporation that creates pores in cell membranes using sound waves, photoporation that creates pores in cell membrane using laser pulses, magnetofection concentrates magnetic particles with DNA into the cells, and hydroporation that alters cell permeability [36]. Chemical methods involve the formation of compound complexes with DNA that are then able to enter the target cell via endocytosis making this method suitable for delivery of large genes. The examples of chemical mechanisms for gene delivery are liposomes which form lipoplexes with DNA molecules, and polymers which form polyplexes with DNA molecules [36]. Most non-viral gene transport is episomal, meaning it stays inside the eukaryotic genome without integrating, and it hasn't been linked to insertional mutagenetic processes in most cases [42]. Moreover, non-viral gene delivery techniques offer a far higher safety profile than viral vectors

since they are less immunogenic. Additionally, there are no genetic capacity restrictions for non-viral gene transgenic vectors [43]. Notwithstanding these safety benefits, low transfection efficiency, especially when compared to viral vectors, remains the primary barrier to the development of non-viral gene vectors [36]. In 2025, only 0.1% of all documented vectors used for gene therapy clinical trials worldwide are non-viral [44].

Table 1: Key Features of Viral and Non-Viral Gene Therapy Vectors

Feature	Viral Vectors	Non-Viral Vectors
Efficiency	High efficiency in delivering genetic material into cells	Lower efficiency compared to viral vectors, especially for in vivo delivery
Immunogenicity	Can trigger immune responses, potentially limiting repeated administration	Less immunogenic, lower risk of immune reaction
Capacity	Limited cargo capacity	Larger cargo capacity, can deliver larger genes or multiple genes
Safety	Potential for insertional mutagenesis, leading to unintended genetic alterations	Lower risk of insertional mutagenesis
Production	Complex and expensive production processes	Simpler and less expensive production methods
Examples	Adeno-associated viruses (AAV), lentiviruses, adenoviruses	Liposomes, naked DNA, nanoparticles, bacteriophages

1.3 Bacteriophage-Based Gene Therapy as an Alternative

1.3.1 Bacteriophages as Therapeutic Non-Viral Vectors

Conventional non-viral DNA vectors, like plasmids, are not ideal due to their bacterial backbones, which contain unmethylated CpG motifs. These motifs, recognized by the innate immune system as pathogen-associated molecular patterns, can trigger immune responses and lead to transgene silencing [45,46]. CpG immunostimulation is thought to play a key role in suppressing transgene expression over time [45].

Minivectors, or vectors lacking bacterial backbones, are linear covalently closed or circular covalently closed double-stranded molecules that only carry the gene expression cassette. They have demonstrated increased transfection efficiency, extended gene expression, and enhanced cytoplasmic distribution due to their reduced size which could improve gene transfer through better nuclear transport [47].

Bacteriophages/phages are viruses that specifically infect bacterial cells and are the most abundant biological entities on Earth. Bacteriophages have diverse sizes, shapes, and genomes, but all share a structure where a nucleic acid genome is encapsulated in a protein shell known as capsid. Phages are species-specific and infect only certain bacterial species or strains [48]. They can serve as a tool in gene therapy since phages can be used as vehicles for delivering genetic material to human cells. Bacteriophage-mediated gene therapy has numerous advantages over traditional viral vectors, including lower immunogenicity, increased specificity, and large DNA capacity [43]. It has been already established that viral vectors can trigger strong immune responses in patients [46]. However, bacteriophages are a lot less likely to be recognized and attacked by the immune system. This makes them a safer and perhaps more effective option due to the possibility of repeated administrations. Additionally, engineered bacteriophage vectors can select for certain types of cells

to perform targeted gene transfer. Cell specificity is also essential for reducing off-target effects and increasing therapeutic efficacy [43]. In addition, phages can carry larger genetic cargos compared to the viral vectors, making them suitable for delivering multiple genes or complex cassettes [49]. There are various possible strategies to adapt phages for gene therapy, one of the options is to alter the phage's coat proteins allowing them to be recognized in human cells and letting them bind receptors. Phage display is a critical technology since it allows phages to interact with desired molecular tags. Peptide expression can be altered through genetic engineering or chemical conjugation with targeting ligands [43].

1.3.2 Filamentous M13 Bacteriophage for CNS Therapeutic Applications

Filamentous bacteriophages belong to the family *Inoviridae* and are characterised by a single-stranded DNA (ssDNA) genome encapsulated within a long, filamentous protein coat. These phages are typically 1–2 μm in length and 6–7 nm in diameter, with virion length directly proportional to genome size, such that longer genomes result in longer phage particles [50]. Among filamentous phages, the F-specific filamentous (Ff) phages that infect male (F+) strains of *Escherichia coli* (*E. coli*) are the most extensively studied. Unlike lytic bacteriophages, filamentous phages do not kill their host cells upon infection; instead, newly assembled phage particles are continuously extruded through the bacterial membrane, allowing the host cell to survive and proliferate [50]. The bacteriophage used in this project is M13, one of the most well-characterised and functionally versatile members of the Ff phage family [51]. M13 phage infects *E. coli* cells carrying the F-episome and produces progeny phages without lysing host cell. Structurally, the M13 phage particle consists of a ssDNA genome surrounded by approximately 2,700 copies of the major coat protein, pVIII, along with five copies each of four minor coat proteins: pIII and pVI at one end of the filament, and pVII and pIX at the opposite end [51].

The coat protein pIII mediates the phage genome's entry into a host cell, marking the start of the M13 life cycle. Although the precise mechanism of phage genome entry into the host is not well understood, host replication enzymes transform the ssDNA genome into a double-stranded form after entry. The constitutive promoters on the double-stranded replicative form DNA (RF DNA) drive transcription of mRNA encoding all 11 phage proteins, as summarized in Table 2 [52]. Using the RF DNA as a template, rolling circle replication creates more single-stranded copies of the M13 genome which are then sequestered by pV for packaging into progeny phages [52]. The membrane-imbedded phage assembly complex recognizes the genome and assembles coat proteins around the DNA as it passes through the cell membrane. The phage particle is then freed from the cell [52]. The schematic representation of M13 bacteriophage is shown in Figure 1.

Its nanoscale dimensions, genetic flexibility, and modular structure allow for genetic modification of the phage capsid and genome [53], making M13 particularly interesting for gene delivery and targeting applications in mammalian systems, including the CNS. In CNS-related applications, M13 has mainly been investigated as a delivery vehicle, where surface-displayed ligands enable targeted interaction with specific neural or glial cell populations [54]. These properties make M13 a promising candidate for CNS gene therapy strategies that require cell-type specificity, controlled gene expression, and improved safety profiles compared to conventional viral vectors [54].

Table 2: Summary of M13 Bacteriophage Protein Functions

Protein	Group	Function
pI	Assembly & Extrusion	Inner membrane protein that connects the assembly machinery to the membrane [55]
pII	Replication	Initiates ssDNA replication by making a nick in the M13 RFDNA [56]
pIII	Coat Protein	Minor coat protein that determines host specificity of the phage by enabling the phage to enter the bacterial host [51]
pIV	Assembly & Extrusion	Creates channels in bacterial membrane allowing the phage to exit [57]
pV	Replication	Coats the newly replicated ssDNA and guides it towards the assembly complex to be packaged [58]
pVI	Coat Proteins	Minor coat protein that connects pIII to the major coat protein, pVIII providing stability [59]
pVII	Coat Proteins	Minor coat protein at the tip of the phage particle that maintains correct DNA orientation during assembly [60]
pVIII	Coat Proteins	Major coat protein that wraps around the phage ssDNA [51]
pIX	Coat Proteins	Minor coat protein at the tip of the phage particle [60]
pX	Replication	Regulates the balance between RFDNA and ssDNA [56]
pXI	Assembly & Extrusion	Membrane-associated protein that helps in the phage release process[55]

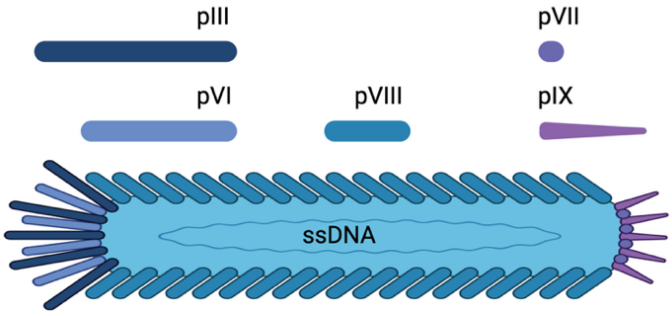


Figure 1: Structure of Bacteriophage M13

This figure shows the arrangement of M13 coat proteins around its ssDNA genome (6407 nt). Coat proteins include around 2000 pVIII proteins that surround the genome (Made with BioRender).

1.3.3 Use of Filamentous Bacteriophages in Gene Therapy

Advancements in phage technology have made bacteriophages more useful in medicine and gene delivery research, largely because Ff phages can display proteins on their surface using phage display technology. By linking a gene for a phage capsid protein with DNA for a specific polypeptide, the target protein can be presented on the surface of the phage [61]. Filamentous bacteriophages such as M13 are well suited for gene delivery due to their genetic simplicity, ease of modification, and ability to display foreign proteins on their surface for targeting specific cell types [62]. Targeting specificity is determined by ligands that bind receptors on the target cell surface, either genetically encoded within the phage genome or associated noncovalently after assembly [62].

Genetically encoded targeting ligands are incorporated into phage coat proteins, most commonly pIII or pVIII, enabling uniform surface display and efficient receptor-mediated binding to target cells [62]. Filamentous phages lack intrinsic tropism for mammalian cells, making them safer for gene transfer [63], but they can be engineered for targeted delivery. By displaying specific ligands on the surface, phages can bind targeted cells and deliver therapeutic agents precisely, reducing side effects and increasing treatment efficacy [64].

Capsid of filamentous bacteriophages is a helical array composed of repeating alpha-helical protein units which results in a rod-shaped structure [65]. This elongated shape and nanoscale dimensions allow filamentous phages, such as M13, to cross the BBB and deliver genes to the cells

in the central nervous system [66]. The blood-brain barrier is a membrane separating the blood from the brain's interstitium, it has very selective permeability that allows cerebral blood vessels to control the flow of ions and molecules into the brain [67]. The BBB is made up of astrocyte end-feet, pericytes, endothelial cells, and capillary membrane. It protects the brain from toxins, by removing dangerous substances from the bloodstream, and supplying nutrients to brain tissue [67]. The rod shape of filamentous phages allows them to diffuse through the tight junctions between endothelial cells in the BBB unlike other, circular or bulky bacteriophages [66]. In addition, this capsid structure theoretically allows filamentous phages to package unlimited DNA inserts. Phage capsid coat can elongate via addition of new protein units and accommodate the gene size [63].

In addition, unlike most bacteriophages, filamentous phages do not burst the host cell when exiting; they bud out individually one by one as they are produced. Therefore, they can be continuously produced by their hosts over many generations allowing to harvest large amounts of phage particles and achieve high titres [64].

Since bacteriophages did not evolve to infect mammalian cells their components are not typically recognized by the mammalian immune system as harmful, making these vectors less immunogenic compared to the viral vectors. This makes them safer, especially for repeated administrations, and reduces the risk of the therapy neutralization [43].

Like many other gene delivery methods, phage-mediated gene transfer shows time- and dose-dependency, which means that the length of exposure to the phage particles and the phage concentration employed affect how efficient the gene delivery is. The success of transfection is largely dependent on the time of gene transfer. It takes some time for phage particles to attach to the cell surface receptors, enter, and transfer genetic material [52]. According to previous studies, transfected cells usually start expressing the new reporter gene after 48 h [62]. This delay is due to the time required for the phage to be internalized and for the phage's ssDNA to be transformed into

dsDNA, which is required for transcription in mammalian cells and the subsequent production of proteins [68]. The percentage of transgene-expressing cells increases with time, suggesting that prolonged phage particle exposure can boost transduction efficiency. However, more exposure time does not substantially improve transduction after 96 h [68].

Another important aspect that significantly affects the success of transfection is the dose of phage particles utilized. It has been shown that transfection by phage can happen at as little as 100 phage particles/cell. But the efficacy of gene delivery improves with higher doses; larger concentrations of up to 1×10^6 phage particles per cell lead to highly efficient internalization, where almost all targeted cells express phage proteins [62]. This is because at higher concentrations more phage particles are available to bind target cells, increasing the chances that all cells will be transfected [68].

Overall, bacteriophage vectors provide a more stable platform for gene delivery which allows to incorporate large DNA inserts and can adapt for multifaceted display [62]. Gene inserts up to 10 kb in size, including the mammalian expression cassette and the targeting ligand sequence, can now be carried by phagemid vectors. This ability is important because it makes it possible to deliver complicated genetic constructs which are frequently needed for complex gene therapy applications [62]. Multifaceted display of phagemids refers to the display of multiple copies of a targeting ligand on the phage particle. This raises the binding affinity to the target cells, which is crucial when high binding specificity is required when the ligand-receptor interaction is poor [69].

1.3.4 Limitations and Challenges of Filamentous Bacteriophages in Gene Therapy

Some of the challenges in use of bacteriophages as gene therapy vectors include delivery efficiency, permanent gene expression, and immune system avoidance. Gene delivery efficiency is limited by biological barriers, as phages have a natural tropism for bacterial cells, not mammalian

ones. They evolved to bind bacterial receptors, which differ structurally from mammalian surface proteins [48]. Thus, genetic modifications are needed for phages to recognize and enter mammalian cells [43].

Achieving long-term expression of the delivered gene is another challenge [43]. For permanent expression, the gene must integrate into the host genome, ensuring replication and inheritance during cell division. However, it is difficult to achieve stable gene integration without disrupting other host genes since random integration can cause mutagenesis, potentially leading to detrimental consequences such as cancer. If the gene remains episomal, it may be lost during cell division as it might not replicate with the host genome. In addition, episomal DNA is more susceptible to degradation, leading to reduced gene expression over time [70].

Another challenge for the use of bacteriophages in gene therapy is immune system avoidance because although phages are less immunogenic than viral vectors, there is still risk of immune detection and clearance [43]. The immune system can target and degrade the phage vector before it can perform gene delivery to the target cell [70,71]. Immune system avoidance is especially important if the delivered gene is being expressed long-term because it is more likely to trigger an immune response, particularly if the encoded protein is foreign to the host [70]. If the immune system starts attacking cells expressing the gene, the overall therapeutic effect will be greatly reduced [43]. In addition, the immune system may become sensitized to the phage vector or the gene product, provoking rapid immune response and making repeated administration less effective [43].

1.4 Intelligent Phagemid-Assembled Gene Expression (iPhAGE) Technology

The Intelligent Phagemid-Assembled Gene Expression (iPhAGE) system is a platform designed to address challenges in treating neurodegenerative diseases. Utilizing bacteriophage-based technology, specifically M13 miniphagemids, it enables the targeted delivery of large,

complex genetic constructs with high specificity and efficiency [5,72]. The system produces DNA minivectors by cloning genes of interest, flanked by signals for rolling-circle amplification. These constructs are packaged into miniphagemids through a streamlined one step process using a helper plasmid in *E. coli* cells, avoiding contamination with prokaryotic sequences like antibiotic resistance genes, thus increasing its safety [5,72].

iPhAGE miniphagemids can be engineered with targeting molecules, such as EGF, for selective delivery to receptor-expressing cells like EGFR-positive astrocytes. Using astrocyte-specific promoters, such as GFAP, the platform drives the expression of reprogramming transcription factors like NeuroD1, enabling astrocyte-to-neuron conversion. Its key advantages include high transfection efficiency, large cargo capacity, low immunogenicity, and the ability to cross the BBB, addressing the limitations of current therapies like poor BBB penetration, limited specificity, immunogenicity, and insufficient capacity for complex constructs [5,72].

The iPhAGE system's scalable, safe, and precise delivery mechanism minimizes off-target effects while ensuring therapeutic precision. iPhAGE technology offers a transformative solution for neurodegenerative diseases filling existing gaps in therapy with a high-capacity platform capable of reprogramming astrocytes into neurons.

M13 modified phage is used in this project as a vector for delivery of transcription factor genes to astrocyte cells. Bacteriophage was chosen for this project due to its unique properties that make it an ideal gene delivery vector for astrocyte reprogramming.

It is possible for M13 bacteriophages to exist as virions outside of *E. coli*, their natural host cell. But to replicate, M13 must first infect a bacterial host, multiply inside the cell, and then assemble its progeny that will exit without bursting the cell [52]. All 11 of the proteins required for this are encoded in the phage genome and are regulated by signalling structures found in a non-coding intergenic region (IR). A phagemid is a plasmid that only includes the sequences within the

IR, also known as the f1 functional origin (f1 ori) [63]. It contains both plasmid and a phage origin and can be replicated by the phage machinery independent of its plasmid origin [73]. The prokaryotic backbone has unmethylated CpG motifs, which can reduce gene expression and trigger immune responses [46,64]. It also contains an antibiotic resistance gene that could contribute to antibiotic resistance in the environment [45]. To avoid these issues, this project uses miniaturized phagemids to target astrocytes. These are hybrid vectors that combine features of plasmids as well as phages[62]. Traditional phage vectors contain the entire phage genome, while miniphagemids carry only necessary phage DNA sequences. Miniphagemids rely on DNA supplied by a helper plasmid for viral protein production and DNA packaging into the capsids [62]. Another advantage of M13 is its large ssDNA capacity, which makes it suitable for carrying complex genetic constructs such as the NeuroD1 reprogramming gene. Furthermore, M13 has low immunogenicity and does not integrate into the host genome, reducing the risk of insertional mutagenesis compared to viral vectors [43]. These features make M13 miniphagemids a safer, more efficient alternative to traditional vectors for delivering reprogramming transcription factors to astrocytes. In this project, M13 miniphagemids are produced by co-transfecting *E. coli* JM109 with precursor and helper plasmids. Once generated, miniphagemids are characterised based on their genetic composition, backbone contamination, size, and concentration. Genetic composition is assessed by visualizing miniphagemid ssDNA via AGE. Backbone contamination is evaluated using a colony assay, where untransformed *E. coli* cells are infected with the produced miniphagemids and plated on selective media to determine if resistance gene transfer has occurred. Finally, miniphagemid size and concentration are analyzed using light scattering techniques. The workflow for characterization of M13 miniphagemids is illustrated in Figure 2.

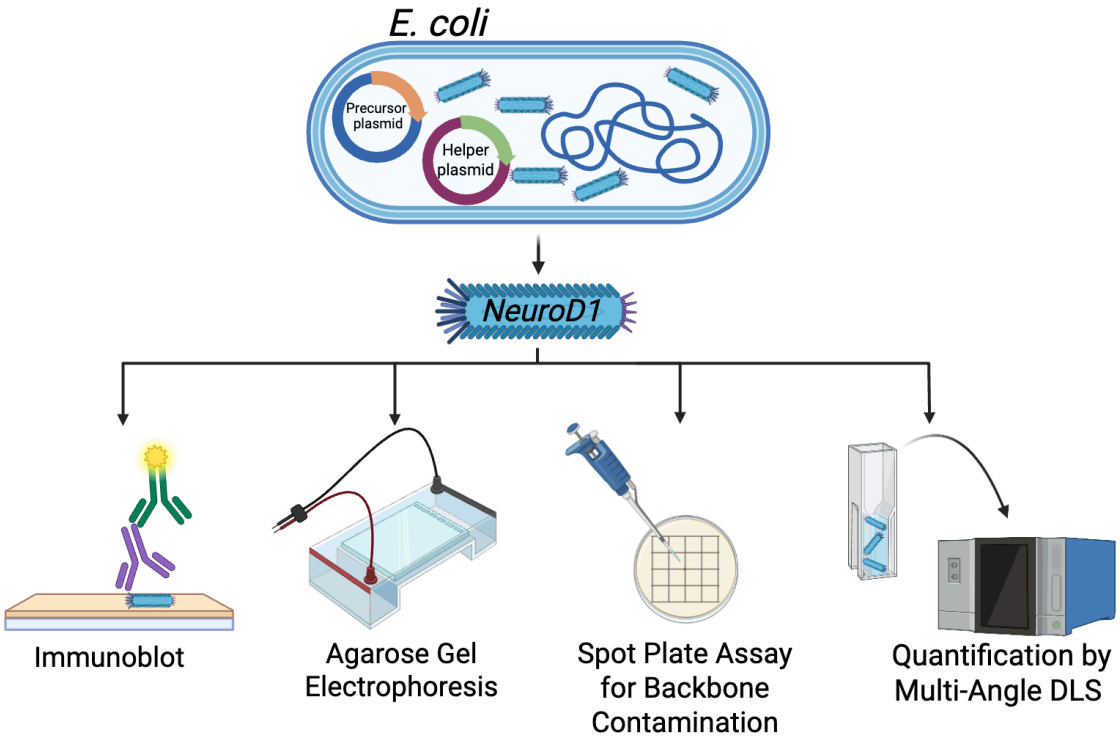


Figure 2: Workflow for M13 Miniphagemid Characterization

Process for assessing M13 miniphagemids, including characterization of genetic integrity, backbone contamination, and physical properties (Made with BioRender).

The iPhAGE system offers a highly advantageous platform for gene delivery, particularly for CNS applications like astrocyte reprogramming. Unlike viral vectors, it has low immunogenicity, doesn't contain prokaryotic sequences, and causes no insertional mutagenesis [35,43]. Miniphagemids can carry large and complex genetic constructs, enabling efficient delivery of reprogramming factors such as NeuroD1 [5,49,72], while displayed ligands allow specific targeting of reactive astrocytes and reduce off-target effects [74,75], which can be further enhanced using astrocyte-specific promoters like GFAP [76]. Its production is cost-effective and adaptable, relying on bacterial hosts rather than expensive mammalian cell culture [77,78]. These features make iPhAGE a safer, more efficient, and versatile tool for gene therapy in neurodegenerative diseases.

2. Rationale, Hypothesis & Objectives

2.1 Rationale

Neurodegenerative diseases are characterised by progressive neuronal loss, leading to severe cognitive, motor, and functional impairments [4]. Despite recent advancements in symptom management, effective treatments for regenerating lost neurons and restoring neural function remain limited, creating an urgent need for new regenerative therapies [79,80]. Astrocytes, protective glial cells in the CNS, offer a promising target for reprogramming into neurons through the expression of specific transcription factors like NeuroD1 [9,81,82]. This approach provides a non-invasive alternative to stem cell therapies, avoiding risks such as tumor formation and immune rejection [12]. This project aimed to overcome the limitations of current gene therapies by developing filamentous bacteriophage vectors with enhanced targeting and transfection capabilities to efficiently deliver transcription factor genes to astrocytes for their reprogramming into neurons. A schematic overview of this approach is presented in Figure 3, illustrating the key steps involved in gene delivery, astrocyte targeting, and neuronal conversion. Using the iPhAGE technology, the project introduces a novel gene delivery platform suited for CNS applications [5]. Compared to traditional viral vectors, bacteriophage-based vectors offer lower immunogenicity, higher cargo capacity for complex genetic constructs, and enhanced specificity for targeting reactive astrocytes. Its ability to cross the BBB and deliver therapeutic constructs directly to astrocytes addresses significant challenges in current therapies [72]. By combining the potential of astrocyte reprogramming with the delivery capabilities of bacteriophage vectors, this project established and initially evaluated an iPhAGE-based gene delivery method for astrocyte to neuron reprogramming.

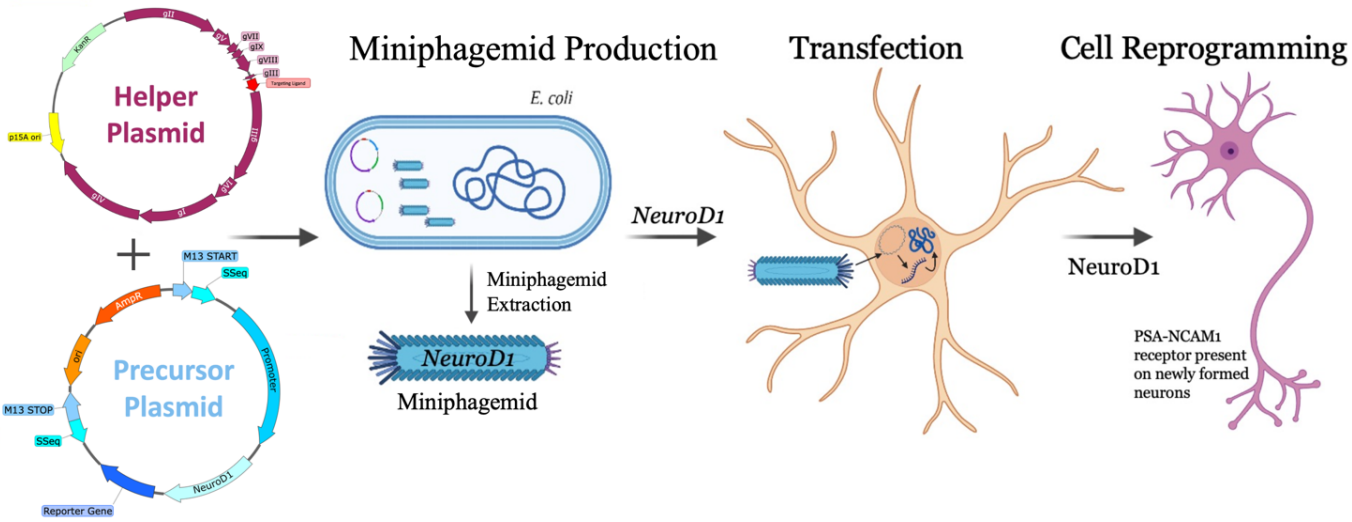


Figure 3: Overview of Astrocyte Reprogramming Using iPhAGE Technology

Figure illustrates a schematic overview of iPhAGE-mediated astrocyte reprogramming for neurodegenerative disease therapy. A bacterial host is transfected with the precursor and helper plasmids to produce M13 miniphagemid vectors, which deliver the transcription factor gene *NeuroD1* to astrocytes. Upon successful gene expression, astrocytes undergo reprogramming into neurons (Made with BioRender).

2.2 Hypothesis

This work proposes that the iPhAGE system can effectively deliver ssDNA constructs encoding the *NeuroD1* transcription factor gene to astrocytes, including LPS-activated astrocytes, in a targeted manner. Successful delivery of a *NeuroD1*::reporter construct will produce detectable reporter gene expression in both resting and activated A7 cells and induce early molecular markers of neuronal reprogramming.

2.3 Objectives

1) Design, construct and characterise iPhAGE vectors carrying (a) *NeuroD1* transcription factor, (b) tissue-specific promoter, (c) and targeting peptides.
    a. Incorporate the *NeuroD1*::marker gene and a marker gene control.
    b. Utilize the GFAP astrocyte-specific promoter, alongside a constitutive CMV promoter as a positive control.
    c. Include targeting peptides for activated astrocytes, using an EGF peptide as a positive control.
2) Assess the gene delivery efficiency to target cells by quantifying reporter gene activity.
    a. Measure reporter gene activity from *NeuroD1*-targeted miniphagemids in resting A7 cells relative to control vectors.
    b. Measure reporter gene activity from *NeuroD1*-targeted miniphagemids in LPS-treated (reactive) A7 cells relative to control vectors.
3) Evaluate the ability of *NeuroD1* constructs to initiate astrocyte-to-neuron reprogramming.
    a. Measure PSA-NCAM expression in treated astrocytes relative to positive (neuronal) and negative (untreated astrocyte) controls.

3. Materials and Methods

3.1 Construct Design and Validation

Table 3: Plasmids Used in This Project

Plasmid	Features	Size (kbp)	Source
pAI1	P_{hGFAP}-NeuroD1-P2A-GFP	7.9	This Study
pAI2	P_{CMV}-NeuroD1-P2A-GFP	6.8	This Study
pAI3	P_{hGFAP}-2A-GFP	6.8	This Study
pJL1	P_{hGFAP}-NeuroD1-P2A-F.Luciferase	8.9	This Study
pJL2	P_{CMV}-NeuroD1-P2A-F.Luciferase	7.7	This Study
pJL3	P_{hGFAP}-NeuroD1-P2A-F.Luciferase	7.7	This Study
Flex Switch	P_{hGFAP}-NeuroD1-Cre-loxP-$P_{EF\text{-}1\alpha}$-dTomato	9.5	This Study
pLuNe	$P_{EF\text{-}1\alpha}$-F.Luciferase-P2A-mNeonGreen	8.1	This Study
p326	$P_{EF\text{-}1\alpha}$-N.Luciferase-P2A-EGFP	6.8	This Study
EF-1α-dTomato	$P_{EF\text{-}1\alpha}$-dTomato	6.8	Addgene plasmid #67527
pM13ori2-cmv-luc	P_{CMV}-F.Luciferase	5.1	Wong, 2023
SW8-IRL1620	pI – pXI, IRL 1620	8.3	This Study
SW8-EGF	pI – pXI, EGF	8.4	Wong, 2023
SW8-EGFSF	pI – pXI, EGF SFSNIAIR	8.4	This Study
SW8-SF	pI – pXI, SFSNIAIR	8.3	This Study
SW8-SG	pI – pXI, SGNSTSNA	8.3	This Study
SW8-SL	pI – pXI, SLSAVDVS	8.3	This Study

Table 4: Miniphagemids Produced in This Project

Miniphagemid	Plasmids Used in Production	Features
AI1-EGF	pAI1 + SW8-EGF	GFP tag and EGF ligand
AI2-EGF	pAI2 + SW8-EGF	
AI3-EGF	pAI3 + SW8-EGF	
JL1-EGF	pJL1 + SW8-EGF	Firefly luciferase marker and EGF ligand
JL2-EGF	pJL2 + SW8-EGF	
JL3-EGF	pJL3 + SW8-EGF	
JL1-IRL1620	pJL1 + SW8-IRL1620	Firefly luciferase marker and IRL1620 ligand
JL2-IRL1620	pJL2 + SW8-IRL1620	
JL3-IRL1620	pJL3 + SW8-IRL1620	
Flex-EGF	Flex Switch + SW8-EGF	dTomato tag and EGF ligand
Flex-IRL1620	Flex Switch + SW8-IRL1620	dTomato tag and IRL1620 ligand
JL1-SF	pJL1 + SW8-SF	Firefly luciferase marker and SFSNIAIR ligand
JL2-SF	pJL2 + SW8-SF	
JL3-SF	pJL3 + SW8-SF	
JL1-SG	pJL1 + SW8-SG	Firefly luciferase marker and SGNSTSNA ligand
JL2-SG	pJL2 + SW8-SG	
JL3-SG	pJL3 + SW8-SG	
JL1-SL	pJL1 + SW8-SL	Firefly luciferase marker and SLSAVDVS ligand
JL2-SL	pJL2 + SW8-SL	
JL3-SL	pJL3 + SW8-SL	
JL1-EGFSF	pJL1 + SW8-EGFSF	Firefly luciferase marker, EGF ligand and SFSNIAIR ligand
JL2-EGFSF	pJL2 + SW8-EGFSF	
JL3-EGFSF	pJL3 + SW8-EGFSF	
LuNe-SF	pLuNe + SW8-SF	Firefly luciferase and mNeonGreen markers and SFSNIAIR ligand

LuNe-SG	pLuNe + SW8-SG	Firefly luciferase and mNeonGreen markers and SGNSTSNA ligand
LuNe-SL	pLuNe + SW8-SL	Firefly luciferase and mNeonGreen markers and SLSAVDVS ligand

3.1.1 Construction of the Precursor Plasmids

The construction of miniaturized phagemid vector starts with the design of a precursor vector, where a mammalian transgene cassette is flanked by M13 start and stop sequences that allow initiation and termination of the translation of the coding region (Figure 7). The cassette is also flanked by the SuperSequences (SSeq) which is a short DNA element added to the construct to help the delivered DNA reach the cell nucleus for expression. SSeq is made from SV40 enhancer sequences that bind nuclear localization proteins, and when those attach, DNA is carried through the nuclear membrane [47]. This is especially important for astrocytes, which divide slowly and cannot rely on cell division for nuclear entry of DNA. In this project, SSeq increases the likelihood that miniphagemid-delivered *NeuroD1* reaches the nucleus for expression. This system has potential to increase *NeuroD1* expression enough to make it sufficient for CNS applications. Outside of the cassette, it contains the origin of replication, f1 *ori*, an ampicillin resistance (Ap^R) gene (*bla*) for selection, and a gene for green fluorescent protein (GFP) or luciferase for screening. As shown in Table 3, in this project eight precursor plasmids were constructed: pAI1, pAI2, pAI3, pJL1, pJL2, pJL3, Flex Switch, and pLuNe. The sequences for all eight plasmids are shown in Figure 4. They were designed using SnapGene 7.2 (https://www.snapgene.com/) and synthesized by Genscript (Genscript Inc., Piscataway, USA).

The pAI1 and pJL1 plasmids both act as test vectors aimed at a target delivery of transcription factor gene, *NeuroD1*, to astrocyte cells but they differ in their reporter systems for monitoring expression. The pAI1 plasmid contains a *GFP* reporter, allowing *NeuroD1* expression

in target cells to be tracked through GFP fluorescence. In contrast, the pJL1 plasmid utilizes *firefly luciferase* (*luc*) reporter gene, enabling *NeuroD1* expression to be assessed through luciferase activity using a luminescence assay. Both plasmids employ the human astrocyte-specific promoter, glial fibrillary acidic protein (GFAP), to drive the *NeuroD1* expression. GFAP is an intermediate-filament protein that is abundantly and exclusively expressed in astrocytes in the CNS. Its expression is one of the hallmarks of astrocytic differentiation during development as well as reactive gliosis that follows a numerous types of CNS damage [76]. It has been previously demonstrated that the expression of GFAP can be regulated by the growth factors and hormones independently of cell division, and it has a half-life of approximately 7.5 days, indicating its stability [83]. Glial filaments accumulate in astrocytes during their development and significantly increase in reactive astrocytes, which hypertrophy in response to numerous traumas to the CNS [83]. In this project GFAP promoter is being used for the expression of transcription factor gene, *NeuroD1* in astrocytes.

Neurogenic Differentiation Factor 1 (NeuroD1) is a transcription factor from the basic helix-loop-helix (bHLH) family needed for neural development and differentiation. It also plays a role in adult neurogenesis, and if its expression is decreased it might lead to the reduction of functional neurons generated from adult neural precursors [84]. NeuroD1 regulates the expression of genes involved in neural development, and in this project NeuroD1 is used for astrocyte reprogramming, where it acts as a pro-neuronal transcription factor to convert reactive astrocytes into neurons [81,82]. In the context of this project, pAI1 and pJL1 enable comparative assessment of *NeuroD1* expression through different detection methods, GFP fluorescence for pAI1 and luciferase activity for pJL1.

The second set of precursor plasmids, pAI2 and pJL2, both act as a positive control for the expression of *NeuroD1* gene but differ in their reporter systems. The AI2 plasmid includes the

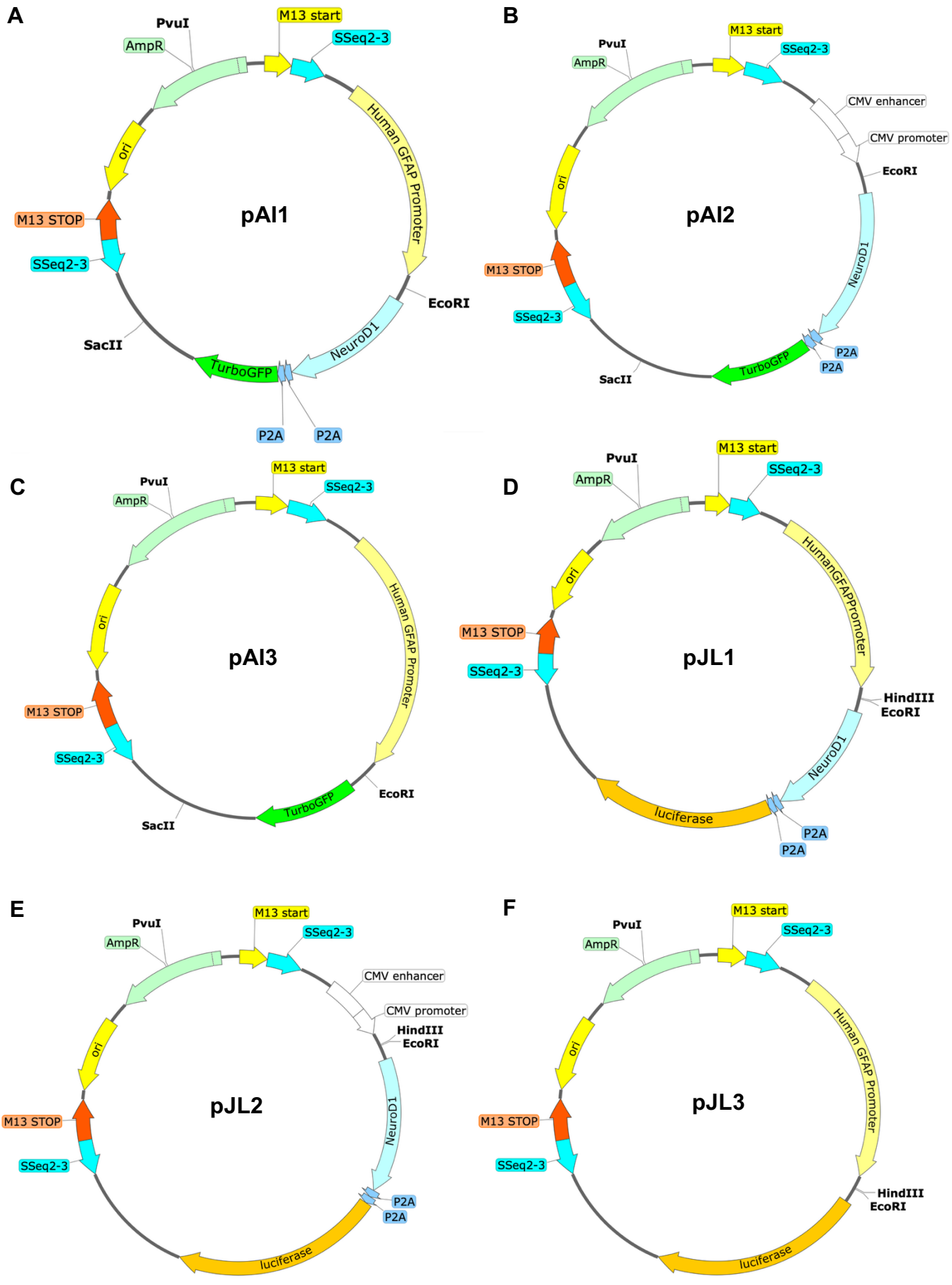
NeuroD1 and *GFP* genes under a universal promoter cytomegalovirus (CMV). CMV is a strong non-specific promoter that allows for stable and constitutive transgene expression in various eukaryotic cells [85]. In this project, pAI2 will allow *NeuroD1* expression to be confirmed by directly observing GFP fluorescence in target cells to verify that they can successfully express the *NeuroD1* gene. In contrast, the pJL2 plasmid also serves as a positive control for *NeuroD1* expression but instead uses the *luc* reporter gene. With pJL2, *NeuroD1* expression will be monitored through luciferase activity, measured by a luciferase assay.

The third set of precursor plasmids, pAI3 and pJL3, both act as a positive control for the GFAP astrocyte specific promoter, but they differ in their reporter systems. The pAI3 plasmid contains the GFAP promoter as well as the *GFP* gene, without the *NeuroD1* gene. In this project, pAI3 will confirm that the GFAP promoter can successfully drive *GFP* expression in astrocyte cells, verifying the promoter's functionality and astrocyte specificity under the experimental conditions. pJL3 also serves as a positive control for the GFAP promoter but utilizes *luc* reporter gene instead of *GFP*. The expression in cells transfected with pJL3 will be measured through a luciferase assay.

This project also uses the Flex Switch precursor plasmid, which serves as a test vector designed to deliver the *NeuroD1* transcription factor gene specifically to astrocytes. Unlike other precursor plasmids, this vector places its genes under two different promoters: *NeuroD1* is driven by the astrocyte-specific GFAP promoter, while the *dTomato* reporter is controlled by the universal EF-1α promoter. The plasmid also includes a *cre* recombinase gene within the same GFAP-regulated cassette, enabling *cre* to be transcribed directly once the plasmid enters an astrocyte. When the target cell recognizes the GFAP promoter and initiates *NeuroD1* expression, *cre* is expressed at the same time. As Cre accumulates, it acts on the *loxP* sites flanking the *dTomato* reporter gene, shown in Figure 4. This excises the gene, flips it into the correct orientation, and

ligates it back into place. After this recombination event, the cell can use the EF-1α promoter to express the *dTomato* reporter. This dual-promoter system allows us to track astrocytes after they convert into neurons. In other precursor plasmids, both *NeuroD1* and the reporter gene are driven by the GFAP promoter. Because GFAP activity is lost as astrocytes transition into neurons, expression of both *NeuroD1* and the reporter gene eventually stops. This makes it difficult to distinguish newly reprogrammed neurons from existing neurons in the tissue. In contrast, Flex Switch preserves reporter expression even after cells lose GFAP activity. Since the *dTomato* reporter is placed under the universal EF-1α promoter, it continues to be expressed once reprogrammed astrocytes become neurons. This enables long-term tracking of converted cells.

This project also uses the pLuNe plasmid, which differs from the other precursor plasmids. pLuNe does not encode our gene of interest, *NeuroD1*, and instead serves as a positive control for the miniphagemid delivery system. It carries *firefly luciferase* and *mNeonGreen* reporter genes under the Elongation Factor-1 alpha (EF-1α) promoter. EF-1α is a strong, constitutive, and universal human promoter that is helpful in cases where viral promoters such as CMV become silenced, providing stable and long-term gene expression [86]. In this plasmid, *GFP* was replaced with *mNeonGreen* because *mNeonGreen* is significantly brighter, matures more quickly, remains stable, and has good photostability, making it superior for detecting low-abundance proteins [87]. Additionally, pLuNe incorporates a feature not present in the other precursor plasmids: the Torque Teno Virus (TTV) 19 UTR. This non-coding regulatory sequence acts as a transcriptional enhancer, increasing promoter activity, mRNA production, and transcript stability, which collectively enhance protein expression without adding immunogenic or protein-coding elements [88,89].



(Continued on the next page)

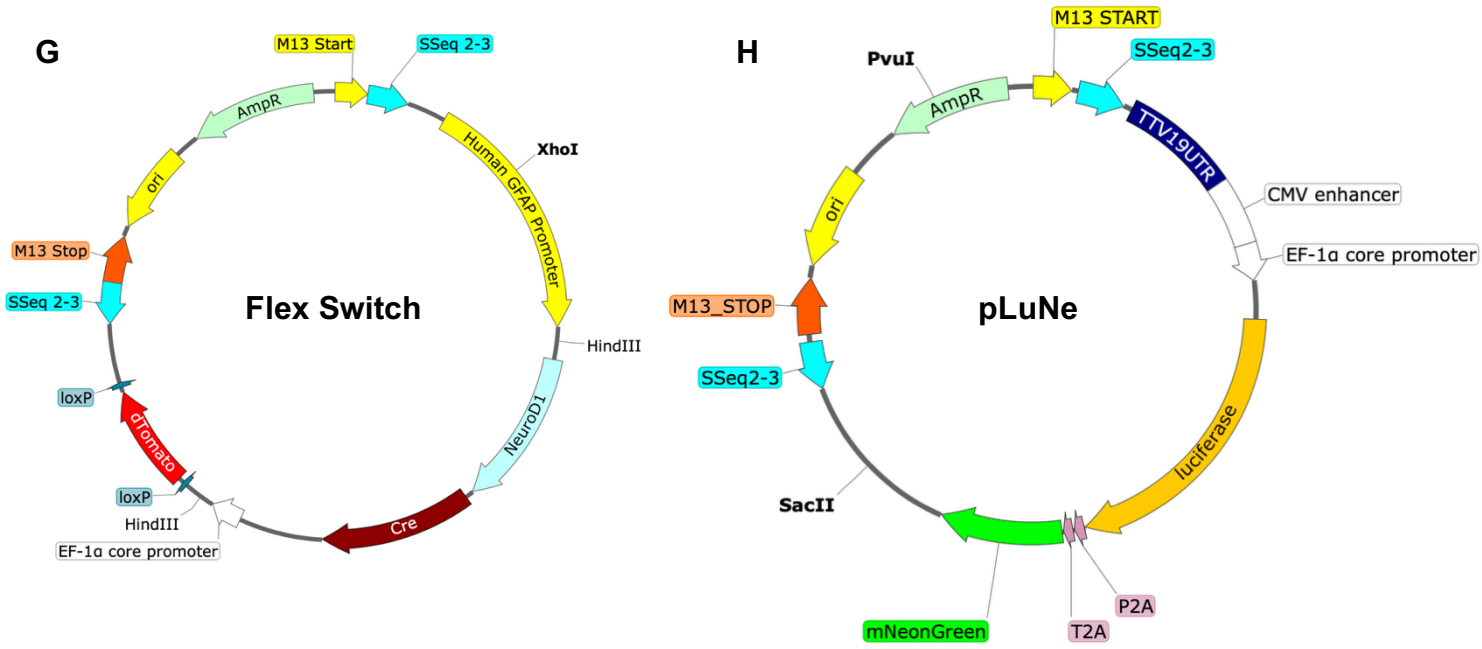


Figure 4: Miniphagemid Precursor Plasmid Constructs

Reporter gene *GFP*, and transcription factor gene *NeuroD1* were inserted between M13 START and M13 STOP in pAI1 under the control of the astrocyte specific promoter, GFAP (A). Reporter gene *GFP*, and transcription factor gene *NeuroD1* were inserted between M13 START and M13 STOP in pAI2 under the control of the universal promoter, CMV (B). Reporter gene *GFP* was inserted between M13 START and M13 STOP in pAI3 under the control of the astrocyte specific promoter, GFAP (C). Reporter gene *firefly luciferase*, and transcription factor gene *NeuroD1* were inserted between M13 START and M13 STOP in pJL1 under the control of the astrocyte specific promoter, GFAP (D). Reporter gene *firefly luciferase*, and transcription factor gene *NeuroD1* were inserted between M13 START and M13 STOP in pJL2 under the control of the universal promoter, CMV (E). Reporter gene *firefly luciferase* was inserted between M13 START and M13 STOP in pJL3 under the control of the astrocyte specific promoter, GFAP (F). Transcription factor gene *NeuroD1* under the control of the astrocyte specific promoter, GFAP, and the reporter gene *dTomato* under the control of the universal promoter, EF-1α were inserted between M13 START and M13 STOP in Flex Switch (G). Reporter genes *mNeonGreen* and *firefly luciferase* were inserted between M13 START and M13 STOP in pLuNe under the control of the universal promoter, EF-1α (H).

3.1.2 Construction of the Helper Plasmids

In addition to the precursor plasmid, a helper plasmid is required for miniphagemid production. It contains all the necessary phage proteins to replicate the cassette and assemble the viral capsid [63]. This design allows the phage proteins, supplied *in trans* by the helper plasmid, to excise and re-circularize the transgene cassette, creating a miniphagemid free from the bacterial backbone (Figure 7). Additionally, the helper plasmids contain a Kn^R gene (*nptII*), enabling the selection of successful transformants. The sequences of the helper plasmids depicted in Figure 5,

were designed in SnapGene 7.2 (https://www.snapgene.com/) and synthesized by Genscript (Genscript Inc., Piscataway, USA) [63].

SW8-EGF, SW8-IRL1620, SW8-EGFSFSNIAIR, SW8-SFSNIAIR, SW8-SGNSTSNA, and SW8-SLSAVDVS helper plasmids contains all 11 M13 proteins, functions are summarized in Table 2. Notably, these helper plasmids are self-packaging deficient, meaning they are not packaged into the miniphagemid along with the precursor plasmids. This was achieved by deleting the packaging signal (PS) and replacing it with a *trp* terminator that forms a hairpin loop, physically preventing the helper plasmid from being packaged. SW8-EGF incorporates the *epidermal growth factor* (*EGF*) gene into M13 *gIII* for targeted delivery. EGF, a growth factor regulating proliferation and survival, binds the epidermal growth factor receptor (EGFR), a tyrosine kinase receptor highly expressed in epithelial cells [90,91]. Displayed on the pIII protein, EGF facilitates miniphagemid attachment to EGFR, enabling genetic cargo delivery to mammalian cells, particularly in epithelial tissues [92,93]. SW8-IRL1620 translationally fuses the *IRL-1620* gene to the N-terminal end of the N2 domain of the M13 *gIII*, enabling astrocyte targeting by displaying IRL-1620 as a N-terminal fusion to the pIII protein. As a selective endothelin B receptor (ETBR) agonist, IRL1620 binds the overexpressed receptor on reactive astrocytes [74]. This interaction facilitates miniphagemid attachment and genetic cargo delivery [75]. The SW8-EGFSFSNIAIR construct incorporates the *EGF* gene into the M13 *gIII* coat protein and the SFSNIAIR peptide sequence into M13 *gIIX*, enabling dual-display on the phage particle. The helper plasmids SW8-SFSNIAIR, SW8-SGNSTSNA, and SW8-SLSAVDVS each encode their respective peptide sequences into M13 *gIII*, facilitating targeted delivery to reactive astrocytes. These artificial peptides were identified from a family of peptides with specificity for neuroinflammatory states in brain microglia and astrocytes. The peptides SFSNIAIR, and SLSAVDVS, are predicted to selectively bind undetermined receptors on reactive astrocytes, providing a strategy for precise targeting of these cells in

pathological contexts. While SGNSTSNA is expected to bind receptors on resting astrocytes and be used as a negative control against the other 2 peptides [94]. The peptides SFSNIAIR, and SLSAVDVS have been derived from early growth response (EGR) protein and olfactory receptor (OR), while SGNSTSNA has been derived from fibronectin type III domain-containing 3C1 (Fndc3c1) [94]. DNA sequences for those peptides can be found in Appendix C: Phage Display Sequences.

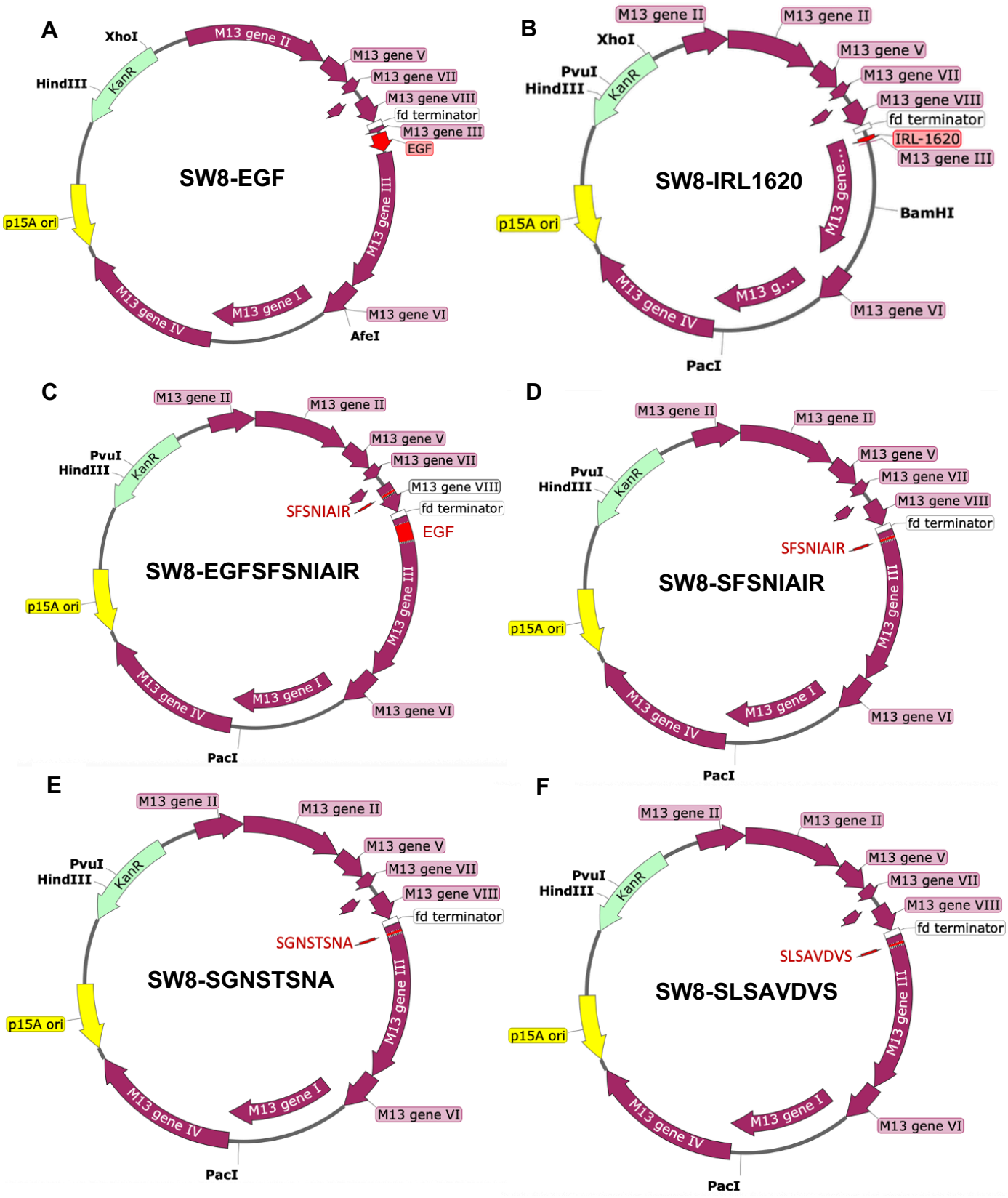


Figure 5: Miniphagemid Helper Plasmids Constructs

SW8-EGF is a helper plasmid deficient in self-packaging that contains all the genes necessary for M13 phage replication, transcription, assembly and packaging along with *EGF* gene for general mammalian cell targeting (A). SW8-IRL1620 is a helper plasmid deficient in self-packaging that contains all the genes necessary for M13 phage

replication, transcription, assembly and packaging along with *IRL 1620* gene for reactive astrocyte targeting (B). SW8-EGFSFSNIAIR is a helper plasmid that encodes both EGF and SFSNIAIR peptides for reactive astrocyte targeting (C). SW8-SFSNIAIR is a helper plasmid that encodes SFSNIAIR peptide for reactive astrocyte targeting (D). SW8-SGNSTSNA is a helper plasmid that encodes SGNSTSNA peptide for resting astrocyte targeting (E). SW8-SLSAVDVS is a helper plasmid that encodes SLSAVDVS peptide for reactive astrocyte targeting (F).

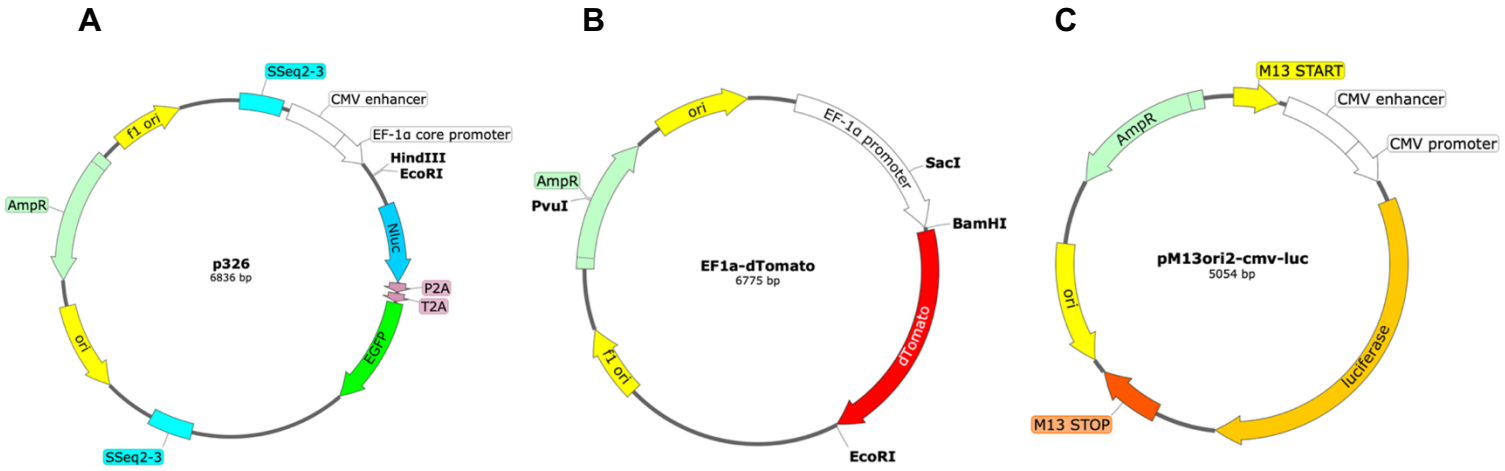


Figure 6: p326, EF-1α-dTomato and pM13ori2-cmv-luc Plasmids

Plasmid p326 is used as a positive control for transformations, restriction digests, and transfections with *GFP* carrying plasmids and miniphagemids. It is detected via GFP reporter and Ap^R marker. EF-1α-dTomato is used as a positive control for transfections with Flex Switch and miniphagemids derived from it. It is detected via dTomato reporter and Ap^R marker. pM13ori2-cmv-luc is used as a positive control for transfection with *F. luciferase* carrying plasmids and miniphagemids. It is detected via luciferase assay and Ap^R marker.

3.1.3 Restriction Digest Analysis of Plasmid Constructs

Table 5: Bacterial Strains Used in This Project

Bacterial Strain	Genotype	Description	Application	Source
E. coli JM109	FtraD36 proAB+ lacig lacZ_M15/ _(lac-proAB) endAl glnV44 thi-1 e14 (McrA:) recAl gyrA96 relAl hsdR17	- Fast growing, high rate of phage assembly - Best-performing strain for phagemid purity	- Amplification of all constructs (except for Flex Switch construct) - Production of miniphagemids - Miniphagemid purity testing	NEB
E. coli Stbl4	F- morA (mcrCB-hsdSMR-mrr) recAl endAl gyrA96 relAl thi-1 supE44 N; optimized for stability of direct repeats	- Slow growing, low rate of phage assembly - Recommended for the propagation of unstable inserts	- Amplification of Flex Switch construct - Production of Flex Switch miniphagemids - Long term storage of all constructs	NEB

NEB: New England BioLabs (Ipswich, USA)

To confirm that the plasmids used in this experiment are correct and behave as expected, the helper and precursor plasmids have been individually transformed into the *E. coli* JM109 or Stbl4 (Table 5) cells and then plasmid DNA was extracted from the cells. dsDNA was extracted from the cells using the Monarch Plasmid Miniprep Kit (Catalog # T1110S, NEB, Ipswich, USA). Bacterial transformation process is described in more detail in section 3.1.4 Co-Transformation of Competent *E. coli* Cells by Precursor and Helper Plasmids. The concentration and purity of the extracted DNA were measured using the NanoDrop 2000 spectrophotometer (Thermo Fisher Scientific, Waltham, USA). Plasmid extracts were then subjected to a double restriction digest, where the DNA was cut using two restriction enzymes.

Enzyme selection is performed by identifying two unique restriction sites on the target plasmid that generate two fragments of different sizes between 500 and 10,000 bp. For each 20 µL reaction, 2 µL of rCutSmart buffer (Catalog # B6004S, NEB, Ipswich, USA), 1 µL of restriction enzyme (NEB, Ipswich, USA), and 500 ng of DNA are combined in a microcentrifuge tube with the calculated volume of nuclease-free water to reach the final volume of 20 µL. The reaction is then incubated at 37 °C for 30 min. After incubation, 4 µL of 6x purple gel loading dye (Catalog # B7024S, NEB, Ipswich, USA) is added to the reaction. Samples can then be stored at -20 °C or loaded onto a gel immediately.

Each DNA sample was visualized via agarose gel electrophoresis (AGE) using Tris-Acetate-EDTA (TAE) buffer (Catalog # BP1332500, Thermo Fisher Scientific, Waltham, USA). To prepare a 0.8% agarose gel, 100 mL of 1X TAE buffer was mixed with 0.8 g of agarose powder in the designated flask. The mixture was then heated until the agarose fully dissolved and 3 µL of ethidium bromide were added, carefully mixed, and poured into the casting tray with a comb. Gel was then allowed to solidify for ~ 30 minutes. Afterwards, the gel was placed in the electrophoresis chamber with 1X TAE buffer, and 20 µL of DNA samples were loaded in addition to 2 µL of 1 kb Plus DNA ladder (Catalog # N3200S, NEB, Ipswich, USA). The gel was run at 100 V for ~1 h and then imaged via transilluminator AlphaImager HP (Cell Biosciences, San Leandro, USA).

3.1.4 Co-Transformation of Competent *E. coli* Cells by Precursor and Helper Plasmids

All miniphagemids and plasmid constructs were produced using freshly cultured *E. coli* JM109 grown in Luria-Bertani (LB) broth base (Catalog # 12795027, Thermo Fisher Scientific, Waltham, USA) diluted in dH_2O to make liquid media. The cells were co-transformed via heat-shock with 100 ng of precursor plasmids, JL and AI, containing transcription factor genes and 100 ng of the SW8-EGF helper plasmid, generating multiple types of miniphagemids, as shown in

Table 4. Calcium chloride competent JM109 *E. coli* cells were thawed on ice for 30 min before carrying out the co-transformation. DNA samples were then added to the competent cells and incubated on ice for 30 min. The cells were then transformed via heat shock at 42 °C for 90 s and immediately placed back on ice for 3 min. 1000 µL of LB broth was added, and then cells were incubated in a 37 °C shaking incubator at 250 RPM (revolutions per minute) for 1 h to allow recovery and expression of antibiotic resistance genes. The cells were plated on LB agar plates containing kanamycin (Kan) (Catalog # 11815024, Thermo Fisher Scientific, Waltham, USA) and ampicillin (Amp) (Catalog # AC611770250, Thermo Fisher Scientific, Waltham, USA) and incubated overnight in a 37 °C incubator. Amp and Kan antibiotics were added to the media to maintain selective pressure on the successfully transformed cells, since the precursor plasmids contained an ampicillin-resistance (Ap^R) gene (*bla*), and the SW8-EGF helper plasmid contained a kanamycin-resistance (Kn^R) gene (*nptII*). A negative control and positive control were also transformed into JM109 competent cells. The negative control was plated on LB + Kan and Amp plate using competent cells without the addition of DNA samples to detect any contamination. The positive control was plated on LB + Amp plate using competent cells transformed with 100 ng of p326 plasmid.

3.1.5 Miniphagemid Production and Purification

Following transformation, the precursor plasmid is amplified in the bacterial host in its original full plasmid form and produces an intermediate dsRFx DNA through cassette excision. Phage machinery then directs the synthesis of ssDNA from this RF intermediate which composes the miniphagemid genome (Figure 7). The ssDNA is then packaged by phage assembly proteins encoded by the helper plasmid. The resulting ssDNA-containing miniphagemids are assembled at the bacterial membrane and secreted. Produced miniphagemids are summarized in Table 6.

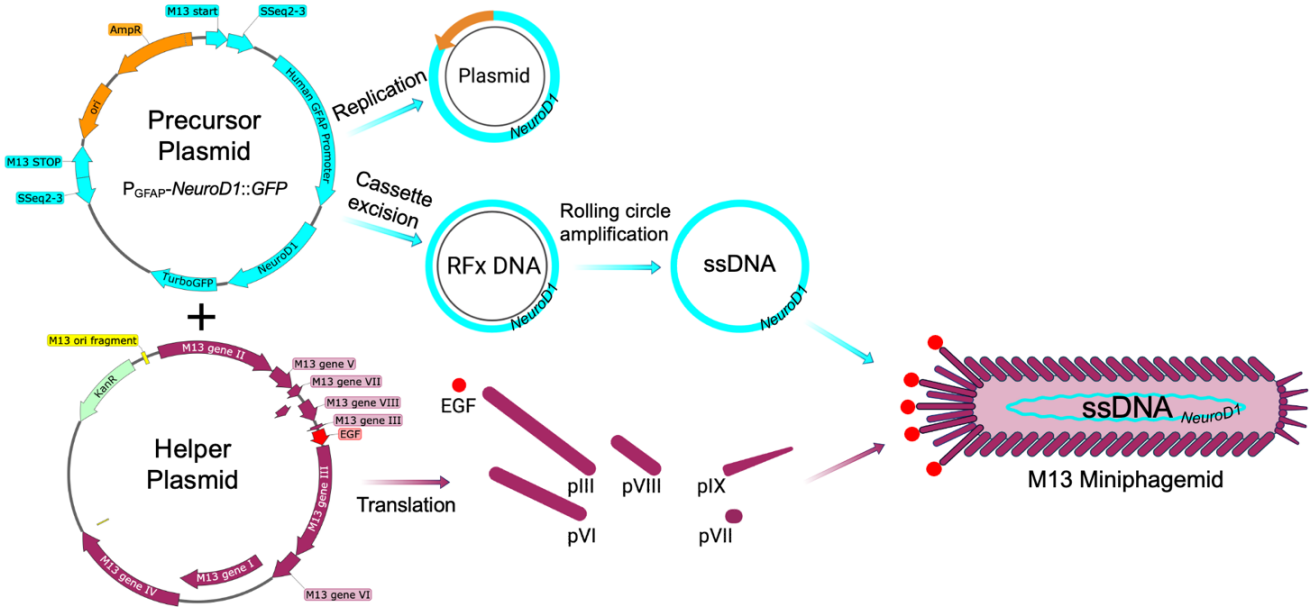


Figure 7: Production of *NeuroD1*-encoding M13 Miniphagemids from Precursor and Helper Plasmids

Schematic illustrating the production of a *NeuroD1*-encoding M13 miniphagemid. The helper plasmid supplies the proteins required for miniphagemid assembly. The precursor plasmid encodes the M13 origin of replication and packaging signal flanking the P_{GFAP}–*NeuroD1*::*GFP* cassette. Once miniphagemid production is initiated in the host, multiple DNA species are generated, including the full-length precursor plasmid, RF DNA, and the single-stranded miniphagemid genome. The miniphagemid DNA is selectively packaged into M13 particles, while the helper plasmid and non-packaged DNA forms remain excluded. The final product is an M13 miniphagemid carrying the *NeuroD1* transgene (Made with BioRender).

Table 6: Design and Components of iPhAGE Miniphagemid Constructs

Miniphagemid	Targeting		Promoter	Cargo Gene
	Peptide	Receptor		
AI1-EGF	EGF	EGFR	GFAP	*NeuroD1::GFP*
AI2-EGF	EGF	EGFR	CMV	*NeuroD1::GFP*
AI3-EGF	EGF	EGFR	GFAP	*GFP*
JL1-EGF	EGF	EGFR	GFAP	*NeuroD1::luc*
JL2-EGF	EGF	EGFR	CMV	*NeuroD1::luc*
JL3-EGF	EGF	EGFR	GFAP	*luc*
JL1-IRL1620	IRL1620	ETBR	GFAP	*NeuroD1::luc*
JL2-IRL1620	IRL1620	ETBR	CMV	*NeuroD1::luc*
JL3-IRL1620	IRL1620	ETBR	GFAP	*luc*
Flex-EGF	EGF	EGFR	GFAP	*NeuroD1::dTom*
Flex-IRL1620	IRL1620	ETBR	GFAP	*NeuroD1::dTom*
JL1-SF	SF	Unknown	GFAP	*NeuroD1::luc*
JL2-SF	SF	Unknown	CMV	*NeuroD1::luc*
JL3-SF	SF	Unknown	GFAP	*luc*
JL1-SG	SG	Unknown	GFAP	*NeuroD1::luc*
JL2-SG	SG	Unknown	CMV	*NeuroD1::luc*
JL3-SG	SG	Unknown	GFAP	*luc*
JL1-SL	SL	Unknown	GFAP	*NeuroD1::luc*
JL2-SL	SL	Unknown	CMV	*NeuroD1::luc*
JL3-SL	SL	Unknown	GFAP	*luc*
JL1-EGFSF	EGFSF	EGFR +EGR	GFAP	*NeuroD1::luc*
JL2-EGFSF	EGFSF	EGFR +EGR	CMV	*NeuroD1::luc*
JL3-EGFSF	EGFSF	EGFR +EGR	GFAP	*luc*
LuNe-SF	SF	Unknown	EF-1α	*luc::mNeonGreen*
LuNe-SG	SG	Unknown	EF-1α	*luc::mNeonGreen*
LuNe-SL	SL	Unknown	EF-1α	*luc::mNeonGreen*

Following the transformation of host cells with the precursor and helper plasmids, the produced miniphagemids must be separated from the bacterial culture. The transformed cells, carrying the precursor plasmid and helper plasmid, are grown in a shaking incubator at 30 °C, at 250 rpm in 50 mL of fresh LB broth supplemented with 70 μg/mL Kan, 100 μg/mL Amp, and 5 mM $MgSO_4$ until the optical density reaches $0.01 < OD_{600} < 0.5$. At this stage, the miniphagemids have already extruded from the bacterial cells into the culture medium. To separate the miniphagemids from the bacterial cells, the culture is centrifuged for 10 min at 8000 × g at 4 °C. This step pellets the larger bacterial cells, leaving the smaller miniphagemids in the supernatant. The supernatant is carefully transferred to a new tube to avoid disturbing the bacterial pellet. To remove any remaining bacterial debris, the supernatant containing miniphagemids is passed through a 0.22 μM filter (Catalog # SF0.22PES, FroggaBio, Toronto, Canada). The filtered solution is then concentrated by precipitating the miniphagemids by adding 1/5th the volume of polyethylene glycol (PEG)/NaCl solution and incubated at 4 °C for 48 h. Then, the lysate was centrifuged for 5 min at 12,000 × g at 4 °C to separate the PEGylated miniphagemids from the media. The pellet was then re-suspended in a small volume of ice-cold Tris-NaCl (TN) buffer, 1 mL TN buffer per 25 mL of lysate, and another PEG precipitation was performed to further concentrate the miniphagemids by adding 1/5th the volume of PEG/NaCl solution, incubated at 4 °C for 48 h, followed by another round of centrifugation. The pellet was then re-suspended in 200 μL ice-cold TN buffer. To eliminate any extraneous phage or bacterial DNA, the sample is treated with DNase I (Promega, Madison, USA). After purification, the concentrated miniphagemids are stored in TN buffer at 4 °C [95].

3.1.6 Dot Blot Analysis for Miniphagemids

To confirm the presence of miniphagemids, a dot blot was performed on all the produced miniphagemid samples. Nitrocellulose membrane was cut to size and spotted with 5 µL of each PEG precipitated miniphagemid sample including TN buffer as a negative control. After air drying for 15 min, membrane was blocked with 10 mL of SuperBlock™ buffer (Catalog # 37535, Thermo Fisher Scientifics, Waltham, USA) for 1.5 h on a rocker, followed by three 5-minute washes with TBS-T (Tris-Buffered Saline with Tween 20) buffer. Primary antibody, M13 phage coat protein monoclonal mouse antibody (Catalog # MA1-34468, Invitrogen, Carlsbad, USA), was then diluted in 10 mL of blocking buffer to a 1:1000 dilution and incubated with the membrane overnight on a rocker. The following day, membrane was washed three times with TBS-T buffer, then incubated with horseradish peroxidase (HRP)-conjugated anti-mouse secondary antibody (Catalog # 1706516, Bio-Rad, Hercules, USA), diluted in 10 mL of blocking buffer for 1.5 h in the dark. After three additional 5 min TBS-T washes, 2 mL of Immobilon® Crescendo Western HRP Substrate (Catalog # WBLUR0100, Millipore, Burlington, USA) was added and incubated for 2 min in on a rocker in the dark before visualization via iBright 1500 imaging system (Catalog #: A44240, Invitrogen, Carlsbad, USA).

To confirm the EGF display on miniphagemids, a dot blot was performed on all the produced EGF displaying miniphagemids. Nitrocellulose membrane was cut to size and spotted with 5 µL of each EGF displaying miniphagemid sample including non-display miniphagemids and TN buffer as negative controls. Similarly to the dot blot above, the membrane was first blocked and then treated with EGF Receptor XP rabbit monoclonal primary antibody (Catalog # 6937, Cell Signalling Technology, Danvers, USA), followed by a secondary HRP-conjugated anti-rabbit antibody (Catalog # 31430, Thermo Fisher Scientific, Waltham, USA). Similarly, the membrane

was then visualised via iBright 1500 imaging system (Catalog #: A44240, Invitrogen, Carlsbad, USA).

3.1.7 Purification of the Single-Stranded Miniphagemid DNA

To further assess the produced miniphagemids, ssDNA was extracted from the samples using phenol-chloroform extraction and ethanol precipitation [95]. Phenol-chloroform was added to 50 µL of miniphagemid sample at a 1:1 ratio and mixed by vortexing until complete emulsification and then centrifuged at 16.4 rpm for 5 min at 4 °C to separate the phases. The upper aqueous phase was transferred to a new tube and 2 volumes of cold 100% ethanol were added, then the sample was vortexed and incubated at room temperature for 2 min to precipitate the DNA. Following centrifugation at 16.4 rpm for 5 min at 4 °C, the supernatant was carefully removed, and the pellet was washed with 1 mL of cold 70% ethanol and centrifuged again for at 16.4 rpm 5 min at 4 °C. After removing the supernatant, the tube was inverted and air-dried for 10 min. The DNA pellet was then resuspended in 10 µL of DNase- and RNase-free molecular-grade water (Catalog # TMS-011-A, Millipore Sigma, Burlington, USA), and DNA concentration was measured using the Thermo Fisher Scientific (Waltham, USA) NanoDrop 2000 spectrophotometer. For analysis, samples were mixed with loading dye and ran on a 0.8% agarose gel at 100 V for 1 h.

3.1.8 Quantifying Miniphagemids via Multi-Angle Dynamic Light Scattering

The next step in miniphagemid characterisation is to assess their concentration and size. This was done using multi-angle dynamic light scattering (MADLS) (Zetasizer, Malvern Panalytical, Worcestershire, UK). In MADLS, a 633 nm laser wave shines through the sample, and the scattered light is detected at multiple angles [96]. By analyzing the fluctuations in the intensity of scattered light over time, which arise from Brownian motion of the particles, the diffusion

coefficient (D) is calculated. The diffusion coefficient is a measure of how fast particles move through a medium due to their Brownian motion. It depends on the size of the particle and therefore can be used to calculate their hydrodynamic diameter based on the Stokes-Einstein equation: $D_h = \frac{k_B T}{6\pi\eta r}$, where k_B is a Boltzmann constant, T is temperature in Kelvin, η is viscosity of the fluid, in this case water (η = 0.89 mPas), and r is the radius of the particle. The hydrodynamic diameter is the size of a particle when it is moving through a fluid, it accounts for the particle as well the surrounding fluid that moves with it [96,97]. Therefore, it does not represent the true dimensions of the particles, but the diameter corresponding to their diffusion in solution. This is important for filamentous phages which are elongated because, even though, miniphagemids have physical lengths of around 1 μm, their measured hydrodynamic diameters are much smaller.

By incorporating the data from multiple scattering angles, MADLS also allows to detect polydispersity of the sample. Polydispersity describes the variation of the particle sizes in the sample. High polydispersity indicates a wide range of sizes, while low polydispersity indicates a uniform size. Polydispersity can be expressed as the polydispersity index (PDI). PDI of up to 0.3 is considered to be monodispersed, while PDI of 0.7 is considered to be highly polydispersed [96,97]. In addition, the scattering intensity is correlated to particle concentration since the amount of light scattered by a sample is directly proportional to the number of particles, since as the number of particles increases, more light is scattered, resulting in a higher scattering intensity [96].

The miniphagemid samples from (Table 4) were diluted 100-fold in 990 μL of ultra-pure water and transferred, in triplicate, to a 12 mm square cuvette (Catalog # FSTP9775594, Thermo Fisher Scientific, Waltham, USA) for measurement via MADLS to determine particle counts per mL and particle size (nm). 100-fold dilution of TN buffer in ultra-pure water was used to blank the instrument before taking the sample measurement.

3.1.9 Quantifying Miniphagemids via OD

To corroborate values obtained through MADLS, miniphagemid concentrations were also measured by UV–visible spectrophotometry using a NanoDrop 2000 spectrophotometer (Thermo Fisher Scientific, Waltham, USA). Measurements were performed in UV-Vis mode using 1 µL sample volumes with the TN buffer used as a blank. Absorbance spectra were recorded without automatic baseline correction, and absorbance values at 269 nm (A269) and 320 nm (A320) were collected. Filamentous phage particles exhibit maximal ultraviolet absorbance at 269 nm due to their ssDNA genome, whereas no phage-associated absorbance is expected at 320 nm; therefore, A320 was subtracted from A269 to correct for any background noise [98]. Phage particle concentration (phage/mL) was calculated using the corrected absorbance and normalized to the number of DNA bases per phage genome using this formula [99]:

$$phage/mL = \frac{(6 \times 10^{16}) \times (A_{269} - A_{320})}{\#\ DNA\ bases}$$

3.1.10 Assessing Miniphagemid Backbone DNA Contamination

The next step in miniphagemid characterisation is to assess their prokaryotic contamination via a colony assay. This assay is used to identify whether miniphagemids have packaged non-target genetic material. While the helper plasmids are designed to be self-packaging deficient, there is still a possibility that they could be packaged along with the precursor plasmid DNA. The presence of this plasmid backbone contributes to prokaryotic contamination, making conventional phagemids unsuitable for therapeutic use. This emphasizes the importance of assessing whether miniphagemid might be a safer alternative. To screen for this, the produced miniphagemids are serially diluted (10^{-1}-10^{-8}) and plated on agar supplemented with kanamycin and fresh *E. coli* cells. Since the *nptII* is encoded only in helper plasmids, bacterial cells infected with properly packaged

miniphagemids should not grow on these plates. The presence of colonies on these plates indicates that *E. coli* was infected with miniphagemids that carry the *nptII*, allowing infected bacteria to survive.

Regarding the precursor plasmids, they are expected to be packaged into the miniphagemids, but only the portion between the M13 start and stop codons, which contains the target gene, *NeuroD1*. The precursor plasmids also encode *bla*, but this gene is located outside of the transgene cassette and is not expected to be packaged into the miniphagemids. However, replication machinery can sometimes read through the stop codon, resulting in the unintended packaging of the entire plasmid. To detect this, the miniphagemids are serially diluted (10^{-1}-10^{-8}) and plated on agar supplemented with ampicillin and *E. coli*. Cells infected with properly packaged miniphagemids should not grow on these plates, as the *bla* should not be part of the genome. The appearance of colonies would suggest that *E. coli* was infected with miniphagemids carrying *bla*, allowing for the survival on the plate.

To screen for miniphagemids that have packaged both the helper plasmid and the entire precursor plasmid or a recombinant of those plasmids, the miniphagemids are serially diluted (10^{-1}-10^{-8}) and plated on agar supplemented with kanamycin, ampicillin, and *E. coli*. Properly packaged miniphagemids should not grow on these plates, as they should lack both the *nptII* and *bla*. If colonies appear, it indicates that *E. coli* was infected with miniphagemids containing both genes, allowing the bacteria to survive.

This backbone contamination assay evaluates the packaging of genetic material in miniphagemids by screening for the presence of non-target genetic material. The absence of colony growth on kanamycin and/or ampicillin plates suggests that miniphagemids are free of detectable backbone DNA, while the presence of colonies indicates contamination.

To perform a colony assay, a susceptible *E. coli* host strain (free of any phagemid or plasmid) was grown on a new LB plate overnight in 37 °C incubator. The next day, 5-10 mL of LB broth is inoculated with a colony from the streak plate and grown to early log phase, defined as an optical density at 600 nm (OD600) ≤ 0.4, at which point the culture becomes slightly turbid. During this time, top agar was supplemented with 5 mM $MgSO_4$ and maintained molten at 50–60 °C by storing it in a 55 °C water bath. LB plates supplemented with Amp, Kan, and Amp and Kan antibiotics are pre-warmed in a 37 °C incubator to prevent premature hardening of the top agar. For each assay plate, 200 µL of early log-phase host cells are added to a sterile test tube, followed by 3 mL of molten top agar. The mixture is quickly poured onto pre-warmed LB plates, evenly spread by tilting, and allowed to cool. A serial dilution of phage stock is then prepared in TN buffer, starting with 90 µL of TN buffer in each tube and 10 µL of the phage stock to create the first (10^{-1}) dilution. This is mixed by pipetting, and subsequent dilutions are made by transferring 10 µL from the preceding tube into the next, continuing to 10^{-8}. For colony assay, 5 µL of each phage dilution and a TN buffer negative control are spotted onto the agar plates, which are left to dry near a Bunsen burner flame before incubating overnight at 37 °C. JM109 *E. coli* cells co-transformed with pJL3 and SW8-EGF plasmids (resistant to ampicillin and kanamycin) were used as a positive control. The next day, plates are examined for colony formation. The backbone contamination efficiency was calculated based on the CFUs observed on the colony plate for the concentration of miniphagemids. The contamination efficiencies of miniphagemids were reported as percentages using this formula:

$$\text{Contamination Efficiency (\%)} = \frac{\text{CFU/mL}}{\text{Concentration (Miniphagemids/mL)}} \times 100$$

Contamination efficiency percentages for each miniphagemid type are summarized in Table 11, where "<" indicates that no colonies were observed on the plates, suggesting that prokaryotic backbone contamination in the miniphagemids is below the detection limit of this assay.

3.2 Assessment of Gene Delivery Efficiency and Targeting Specificity of Miniphagemid Vectors

Table 7: Summary of Mammalian Cell Lines Used in This Project

Cell Line	Cell Type	Application	Source
A7	- Immortalized optic nerve astrocytes of embryonic Sprague-Dawley rats - Unspecified sex*	- Expression of precursor plasmids, and miniphagemids - LPS activation	ATCC
A365	- Human malignant melanoma - Female	- Expression of precursor plasmids, and miniphagemids - PC for assessing miniphagemid specificity and DNA internalization	ATCC

ATCC: American Type Cell Culture Collection (Manassas, USA)

* Primary records from original derivation do not document whether cells came from a male or female rat [116].

3.2.1 Maintaining Immortalized Cell Lines

The A7 and A375 mammalian cell lines (Table 7) were maintained in Dulbecco's Modified Eagle Medium (DMEM) (Catalog # 11965118, Thermo Fisher Scientific, Waltham, USA) supplemented with 10% fetal bovine serum (FBS) (Catalog # 26140079, Gibco, Waltham, USA)

and 0.8% penicillin-streptomycin antibiotic (Catalog # 15140122, Gibco, Waltham, USA). All culturing procedures were performed inside a disinfected Class II biosafety cabinet (Labconco, Kansas City, USA) using aseptic techniques.

3.2.1.1 Recovery from Cryopreservation

To start a new cell line, a frozen cryovial containing desired culture was retrieved from liquid nitrogen storage and thawed in a 37 °C water bath. During thawing, the vial cap was slightly loosened to relieve internal pressure. Once thawed, 1mL of cell suspension was transferred to a 15 mL centrifuge tube (Catalog # TB15-500, FroggaBio, Toronto, Canada). To dilute the cryoprotectant, pre-warmed, serum-free DMEM was added to cells dropwise while mixing. The tube was then centrifuged at 300 x g for 5 min at room temperature and old media was removed to resuspend the cell pellet in 4 mL of fresh complete growth media (DMEM with 10% FBS). The cells were then transferred to a new culture plate (Catalog # 130181, Thermo Fisher Scientific, Waltham, USA) with 0.8% penicillin-streptomycin. All cultures were maintained in a humidified incubator at 37 °C with 5% CO_2.

3.2.1.1 Cell Passaging

Immortalized cell lines used in this project were passaged every 2-3 days upon reaching 80-90% confluence. To begin the passaging process, the old cell media was removed from the plate, and the cell monolayer was washed with ~5 mL pre-warmed phosphate buffer saline (PBS) (Catalog #SH3002802, Thermo Fisher Scientific, Waltham, USA) to remove dead cells and residual serum. Cells were then detached by adding 1 mL of pre-warmed 0.25% Trypsin-EDTA (Catalog # 25200056, Gibco, Waltham, USA) and incubating the plate at 37 °C for 5 min. Following incubation, the enzymatic activity of the trypsin was neutralized by adding 2 mL of

complete 10% FBS media. The suspension was transferred to a 15 mL centrifuge tube and centrifuged at 300 x g for 5 min. After discarding the supernatant, the pellet was resuspended in 5 mL of fresh complete media, and 0.15 mL of the resuspended cells were transferred into a new culture plate containing 4 mL of complete media and 0.8 % of penicillin-streptomycin.

3.2.2 Astrocyte Differentiation and Maintenance

Tissue culture-treated plates were coated with either Matrigel or gelatin depending on the phase of astrocyte differentiation. Matrigel Matrix (Catalog # 356234, Corning, New York, USA) aliquots were stored at -80 °C and thawed on ice to prevent premature gelling. For neural stem cell (NSC) culturing the thawed Matrigel was diluted 1:50 in cold DMEM, immediately added to the culture plate, and incubated at 37 °C for 1 h. For astrocyte differentiation, tissue culture-treated plates were coated with a 0.2% gelatin solution and incubated at 37 °C for 1 h. NSCs were thawed in a 37 °C water bath. 4 mL of pre-warmed Complete Neural Progenitor Media (NPM) (Catalog # 05833, STEMCELL Technologies, Vancouver, Canada) was added dropwise to the cell suspension before centrifugation at 300 x g for 5 min. The resulting cell pellet was resuspended in NPM and plated onto Matrigel-coated plate. For routine maintenance NSCs were passaged every ~6 days or upon reaching high confluency, with media changes performed every 48 h. During passaging, cells were dissociated using 1 mL cold Accutase for 5-7 min at 37 °C, followed by diluting with media. After centrifugation at 300 x g for 5 min, viable cells were quantified via 0.4% Trypan Blue (Catalog # 15250061, Thermo Fisher Scientific, Waltham, USA) exclusion using a hemocytometer and re-plated on Matrigel-coated plate in NPM.

To initiate astrocyte differentiation, NSCs were seeded onto gelatin-coated plate at a density of 30,000 cells/cm² in NPM. After 24 h, non-adherent aggregates were gently removed with PBS wash, and the medium was replaced with basal astrocyte media (AM) that was supplemented with

FBS, penicillin-streptomycin, and astrocyte growth supplement (AGS) (Catalog # 1801, ScienCell Research Laboratories, Carlsbad, USA). Reconstituted AM was protected from light, stored at 4 °C in 45 mL aliquots, and equilibrated to room temperature in the dark prior to use. During the differentiation phase, AM was replaced every 48 h. Upon reaching 95% confluency, cells were passaged using TrypLE Select (Catalog # 12563011, Thermo Fisher Scientific, Waltham, USA) for 5 min at 37 °C, diluting with AM, and seeded at approximately 30,000 cells/cm² onto new gelatin-coated plate. This process was maintained in AM for a minimum of 21 days to reach astrocyte maturation.

3.2.3 Cell Transfection with Precursor Constructs

The plasmids listed in Table 3 are used for the transfection of immortalized astrocytes of embryonic Sprague-Dawley rats (A7) from ATCC (Manassas, USA) to evaluate the transfection efficiency of those plasmids. These cells were cultured at 37 °C in a humidified atmosphere with 5% CO_2 in DMEM supplemented with 10% FBS and 0.8% penicillin antibiotic.

A7 cells were quantified via Countess 3 Automated Cell Counter (Catalog # AMQAX2000, Thermo Fisher Scientific, Waltham, USA) and then seeded in triplicate into 96-well plates (Catalog # 08-772-3, Thermo Fisher Scientific, Waltham, USA) in DMEM supplemented with 10% FBS at a density of ~ 1 x 10^5 cells/mL or 2 x 10^4 cells/well and incubated at 37 °C overnight or until cells reach 70-90% confluency. Then, the Lipofectamine-DNA mix was prepared by combining 0.15 µL of Lipofectamine 3000 Reagent and 0.10 µL of the Enhancer Reagent, P3000 (Catalog # L3000001, ThermoFisher Scientific, Waltham, USA) with 150 ng of precursor plasmid DNA. The mix was then incubated for 10-15 min, combined with 10% FBS DMEM and added to the wells. The plate was gently swirled for even distribution and incubated at 37 °C and 5% CO_2 for 72 h until transfection efficiency evaluation. p326 plasmid was used as a GFP positive control, EF-1α-

dTomato plasmid was used as a dTomato positive control, and non-transfected cells were used as negative controls.

Precursor plasmids were used to transfect A7 cells to evaluate their transfection efficiency and to assess gene expression using *GFP*, *dTomato*, or *mNeonGreen* fluorescent markers, as well as luciferase. To assess transfection efficiency 72 h post-transfection, A7 cells were imaged using fluorescence microscopy to detect any fluorescence signal (Inverted Microscope IX51, OLYMPUS, Tokyo, Japan; DP26 Microscope Digital Camera, OLYMPUS, Tokyo, Japan; X-Cite 120Q, Lumen Dynamics, Mississauga, Canada).

Next, A7 cells were harvested to quantify total percent of fluorescent cells at 72 h through flow cytometry. To harvest the cells from 96 well plates, they were first washed once with 100 µL of PBS. Next, 20 µL of 0.25% Trypsin-EDTA was added to each well and cells were incubated at 37 °C + 5% CO_2 for 5 min. 80 µL of prewarmed PBS + 10% FBS was then added to inactivate 0.25% Trypsin-EDTA. The cells were then moved to a V-bottom plate (Catalog # 781961, BrandTech Scientific, Essex, USA) and centrifuged at 300 x g at room temperature for 5 min. The supernatant was discarded, and the pellet was washed by re-suspending in 100 µL of PBS. The cells were then centrifuged again at 300 x g at room temperature for 5 min. This wash step was repeated one more time after which cells were finally resuspended in 100 µL of PBS. The plate was then loaded into the Beckman Coulter CytoFLEX S Cytometer (USA) to assess the signal emitted by the fluorescent protein. Non-transfected cells were run through the flow cytometer along with the test samples as a negative control to detect any autofluorescence signal. The flow cytometer was set to take up a maximum of 100 µL of sample from each well, at a medium flow rate with the particle size threshold value set to automatic. Analysis of the number of events (cells), and presence of fluorescent signal was carried out using the CytoFLEX Software CytExpert (USA) to assess transfection efficiency, and homogeneity of cell population. Transfection efficiency is

shown in percent and was calculated as the number of cells emitting fluorescence divided by the total number of cells detected.

pJL1, pJL2, pJL3, and pLuNe precursor plasmids contain *luciferase* gene that can be expressed by cells, with the resulting luciferase enzyme serving as an indicator of successful transfection. To assess transfection efficiency, A7 cells were harvested 72 h post-transfection, and a luciferase assay was performed. The 5X luminescence assay lysis reagent (1 mL) (Catalog #16177, Thermo Fisher Scientific, Waltham, USA) was diluted with 4 mL of PBS to obtain a 1X working solution.

Old media was carefully removed from the corners of the wells in the culture plate and cells were washed by adding 50 µL of pre-warmed PBS to the corners of the wells. Then, 20 µL of the 1X lysis reagent was added to each well, and the plate was incubated on a shaker for 15 min at room temperature to lyse the cells. After the incubation, the plate was removed from the shaker, and 20 µL of cell lysate from each well was transferred to a new 96-well plate. Immediately, 100 µL of warm LAR2 reagent (Catalog # 16177, ThermoFisher Scientific, Waltham, USA) was added to each well. The plate was loaded into the Varioskan LUX Multimode Microplate Reader (ThermoFisher Scientific, Waltham, USA), and the luminescence of the samples was measured. Analysis of the luminescence intensity was carried out using the SkanIt v7.1 software (ThermoFisher Scientific, Waltham, USA). Luminescence intensity, which corresponds to the amount of light emitted from the luminescent cells, is shown in relative luminescence units (RLU) which represent the signal strength detected by the instrument.

In addition to fluorescent and luciferase reporters, pLuNe plasmid was labeled with the Label IT Tracker Reagent (Mirus Bio, MIR 7020) to visualize DNA uptake in transfected cells, A7 and A375. First, Label IT Tracker Reagent was equilibrated to room temperature, briefly centrifuged to collect the pellet, and reconstituted with Tracker Reconstitution Solution for first-

time use. Labeling reactions were prepared by combining plasmid DNA with 10X Labeling Buffer A, ultra-pure water, and the Label IT Reagent, for a total reaction volume of 50 µL. Mix was incubated at 37 °C for 1 h, with brief centrifugation at 30 min to minimize evaporation. Unbound dye was removed using the Monarch Spin PCR & DNA Cleanup Kit (Catalog # T1135V, NEB, Ipswich, USA), with elution performed in 20 µL of 60 °C ultra-pure water. Labeled plasmids were subsequently used for A7 cell transfection under the same conditions described above.

3.2.4 Activation of A7 Cells

This step involved working with reactive astrocytes, which more accurately represent the pathological states observed in neurodegenerative diseases or after stroke. Working with these cells is extremely important for this project, since they display characteristics different from resting astrocytes, such as altered signaling pathways or overexpression of certain genes. Astrocyte activation was induced in cultured A7 cells using lipopolysaccharide (LPS) (LPS, *E. coli* serotype O55:B5; Sigma-Aldrich, St. Louis, USA). Cells were seeded 24 h prior to treatment at ~1 x 10^4 cells/mL density to achieve 20 - 30% confluency. LPS was diluted in pre-warmed 10% FBS DMEM to a final concentration of 100 ng/mL, 200 ng/mL and 300 ng/mL and applied to the cells following removal of the existing medium. Cultures were incubated at 37 °C and 5% CO_2 for 24 h. A7 activation was then assessed by analysing morphological changes such as cell size and shape and by western blot analysis of glial fibrillary acidic protein (GFAP) expression [100].

3.2.4.1 Image-Based Assessment of Cell Morphology

After the 24 h incubation, LPS treated A7 cells were imaged using light microscopy (Inverted Microscope IX51, OLYMPUS, Tokyo, Japan) at 40X magnification. Multiple images were acquired from each well to capture the full field of view. These images were subsequently

stitched into a single composite using a bundle adjustment-based image stitching algorithm implemented in the open-source computer vision library OpenCV [101]. It is a technique that aligns visual features, like cell edges, between images within a set. The resulting stitched image provided a continuous view of the cells in the well, this helped to avoid double counting the cells that appeared in multiple images. Following image stitching, individual cells were identified using Cellpose v1, a neural network–based segmentation tool [102]. Cellpose automatically detects cell boundaries and generates binary masks in which each pixel is classified as either belonging to a cell or to the background. For each segmented cell mask, perimeter was calculated by counting boundary pixels separating cell and background regions, while the area was determined by summing all pixels within the mask. Cell circularity was then calculated from the perimeter and area values. Cells with a smaller perimeter to area ratio are closer to a perfect circle, while elongated or irregular cells have larger ratios. Circularity can serve as a quantitative measure of cell morphology [103]. Next, circularity values were compared across experimental conditions to assess whether LPS treatment induced changes in A7 cell shape. Cellular changes following treatment were further characterised by immunoblots for GFAP protein expression.

Using the circularity index data obtained from image analysis of A7 cells a bar plot was generated. Circularity values were grouped into predefined bins, and the fraction of cells within each bin was counted for each treatment condition (0, 100, 200, and 300 ng/mL of LPS). Bin counts were normalized to the total number of cells per condition to obtain relative frequencies. These frequencies were plotted to visualize differences in circularity distributions across the treatment groups.

3.2.4.2 Immunoblots

Activation of A7 cells was also assessed through western blot. A7 cells were treated with LPS in the same way described previously and GFAP was extracted. When cells were ready for harvest, all materials were pre-chilled to preserve protein integrity. A large Styrofoam container was filled with ice until 5 cm from the top, and microcentrifuge tubes and 1 cc syringes were placed on ice. Cell culture plate was placed on ice, and the culture medium was removed using an aspirator. Each well was gently rinsed with 2 mL of ice-cold PBS. Protease and phosphatase inhibitors (Catalog # 78440, Thermo Fisher Scientific, Waltham, USA), stored at 4 °C, were added to the pre-warmed lysis buffer immediately prior to use. Then 65-70 µL of lysis buffer was added to each well. Cells were detached by scraping the bottom of the well and the lysate was transferred into pre-chilled microcentrifuge tubes. Cells were further lysed by passing the suspension through a high-gauge hypodermic needle attached to a 1 cc syringe (Catalog # 14-817-179, Thermo Fisher Scientific, Waltham, USA) at least 20 times. The samples were then centrifuged at 14,000 × g for 20 min at 4 °C to collect supernatant. Extracted protein was stored at -80 °C. Concentration of protein in the sample was measured with Pierce™ BCA Protein Assay Kit (Catalog # 23227, Thermo Fisher Scientific, Waltham, USA).

Next, protein samples were run on western blot. First, the gel rack was assembled and both the resolving and stacking gels are prepared with the 4% stacking gel and 8% resolving gel for 50 kDa GFAP separation [104,105]. The resolving gel is prepared first using 1.0 M Tris-HCl buffer pH 8.8 (Catalog # BP153-500, Thermo Fisher Scientific, Waltham, USA), 20% sodium dodecyl sulfate (SDS), 30% acrylamide- Bisacrylamide (Catalog # 1610154, Bio-Rad, Hercules, USA), N,N,N′,N′-Tetramethylethylenediamine (TEMED) (Catalog # 17919, Thermo Fisher Scientific, Waltham, USA) and freshly prepared 10% ammonium persulfate (APS) (Catalog # 1610700, Bio-Rad, Hercules, USA). These components are mixed on a stir bar, with TEMED added last, and

briefly stirred to ensure uniform mixing. The resolving gel is then poured into the gel rack up to 1.5 cm from the top, and 100% ethanol is layered on top to separate air and make a straight gel edge. After 30 min, once the gel has solidified, the 4% stacking gel was prepared using 1.0 M Tris-HCl buffer pH 6.8, 20% SDS, 30% acrylamide- Bisacrylamide, TEMED and freshly prepared 10% APS, poured on top the resolving gel, and the comb was inserted.

A 4x Laemmli sample buffer was prepared to a final volume of 10 mL. 3 mL of ultra-pure water was added to a clean tube, followed by 2.5 mL of 1 M Tris–HCl (pH 6.8). Then 0.8g of SDS was added, and the solution was gently heated to 50-60 °C with intermittent mixing until the SDS was fully dissolved. 4.0 mL of glycerol and bromophenol blue were subsequently added, and the volume was adjusted to 10 mL with ultra-pure water. The solution was allowed to cool to room temperature before the addition of 2.0 mL of β-mercaptoethanol. The buffer was mixed thoroughly and aliquoted for storage at -20 °C.

Protein samples were then fully thawed and vortexed to ensure homogeneity. Next, 20 µg of protein from each sample was aliquoted to clean microcentrifuge tubes and combined with 4X Laemmli buffer. Both buffer and sample are vortexed, briefly spun down, and heated at 100 °C for 5 min on a heat block. After the incubation samples were loaded in the gel along with the Spectra BR protein ladder (Catalog # 26623, Thermo Fisher Scientific, Waltham, USA). The gel was run in Tris buffer at 120 V for 15 min, followed by 200 V for an additional 50 min.

After electrophoresis, the gel was transferred onto a nitrocellulose membrane using a transfer stack assembled with transfer buffer-soaked blotting paper, membrane, and gel, ensuring removal of air bubbles. The transfer is run at 25 V for 30 min, after which the membrane is incubated in SuperBlock blocking buffer (Catalog # 37581, Thermo Fisher Scientific, Waltham, USA) on a rocker for 1.5 h. After blocking, the membrane was incubated overnight on a rocker

with the anti-GFAP rabbit polyclonal primary antibody (Catalog # ab7260, abcam, Cambridge, UK) at 1:10,000 dilution in blocking buffer containing 0.05% Tween-20 (Catalog # J20605.AP, Thermo Fisher Scientific, Waltham, USA). The following day, the membrane was washed 3 times for 5 min with TBS-T buffer. Then, the membrane was incubated 1.5 h in the dark on a rocker with the HRP-conjugated goat anti-rabbit antibody (Catalog # 12-348, MilliporeSigma, Burlington, USA) diluted at 1:10,000 in blocking buffer containing 0.05% Tween-20. The membrane was then again washed 3 times for 5 min with TBS-T buffer, in the dark.

After the final washes, 4 mL of warm HRP substrate (Catalog # WBLUR0100, MilliporeSigma, Burlington, USA) was added directly onto the membrane and incubated for 5 min on a rocker in the dark. The membrane was then imaged using the iBright 1500 Chemi blot imaging system. Optionally, Ultra TMB blotting solution (Catalog # 37574, Thermo Fisher Scientific, Waltham, USA) may be added to the membrane and incubated for 5 min on a rocker in the dark for additional visualization. Data analysis was performed using Thermo Fisher Scientific Connect Platform. Protein extracts from LPS treated A7 cells were ran on 4 separate gels staining for GFAP and β-actin protein. β-actin staining was performed using anti-β-actin mouse monoclonal antibody (Catalog # ab8226, abcam, Cambridge, UK). The band density was then normalized based on the β-actin signal and averaged from the 4 gels.

3.2.5 Transfection of Cells by Miniphagemids

The next step is to see if miniphagemids displaying ligands specific for reactive cells, such as IRL1620, SF, SG, and SL, preferentially target reactive A7 cells [94]. Transfections were performed using both precursor plasmids and miniphagemids, with efficiency assessed through the same methods as in previous steps. Miniphagemids produced using the designed plasmids were used to specifically target and transfect A7 cells delivering the transcription factor gene, *NeuroD1*.

A7 cells were seeded onto 96-well plates at a density of ~ 1 x 10^5 cells/mL in DMEM supplemented with 10% FBS and incubated at 37 °C overnight or until cells reach 70-90% confluency. The next day 2 x 10^9 VP of miniphagemids (MOI = 100,000) were mixed with fresh DMEM supplemented with 10% FBS and added to the wells. The plate was gently swirled for even distribution and incubated at 37 °C + 5% CO_2 for 72 h until transfection efficiency evaluation. The precursor plasmids were used as a positive control for transfections, while non-transfected cells were used as a negative control. Transfection efficiencies were assessed through flow cytometry as described earlier.

3.2.6 Assessing Cell Viability

In addition to assessing the transfection efficiency of miniphagemids in A7 cells, it is important to evaluate cell viability in the presence of miniphagemids, their storage buffer (TN buffer), and transfection reagents. Viability of A7 cells was assessed using propidium iodide (PI) staining by identifying cells with damaged cell membranes. PI is a red fluorescent dye that cannot enter healthy, live cells, but it can enter dead or dying cells with compromised membranes and bind to DNA [106]. Cell viability was quantitatively assessed by measuring the proportion of PI-positive cells using flow cytometry.

To assess cell death in treated populations, A7 cells were seeded in 96-well plates at a density of 1 × 10^5 cells/mL, as described previously, and incubated overnight at 37 °C. The following day, cells were treated with miniphagemids, TN buffer, or transfection reagents and incubated at 37 °C with 5% CO_2 for 72 h prior to viability assessment. Heat-killed cells were used as a positive control for PI staining, while unstained cells served as a negative control. Following the treatment, 2 μL of PI dye was added to each well, mixed and incubated for 15 min. Immediately after cells were ran through the flow cytometer using the PE (Phycoerythrin) channel.

3.3 Evaluate Astrocyte Differentiation into Neurons Using Neuronal Marker PSA-NCAM

The goal of this objective was to confirm the successful reprogramming of astrocytes into neurons by characterizing the resulting cells using neuronal markers. This analysis focused on determining whether the reprogrammed cells expressed key neuronal proteins. To achieve this, NSC-derived astrocytes were seeded in a 96-well plate and transfected with some of the GFP encoding precursor constructs (pAI1, pAI2, pAI3) to assess transfection efficiency prior to performing reprogramming assays. This allowed us to determine how effectively the cells took up the constructs before evaluating neuronal marker expression. Methodologies for transfection and assessment were described earlier.

The reprogrammed cells were then analyzed for neuronal marker expression using fluorescently linked polysialylated neuronal cell adhesion molecule (PSA-NCAM) antibody staining (Catalog #130-120-437, Miltenyi Biotec, Bergisch Gladbach, Germany). PSA-NCAM is encoded by the *NCAM1* gene and is a receptor overexpressed on immature neurons and serves as a marker for developing neurons in the vertebrate nervous system. However, it is also present in regions of the mature brain that perform morphological and functional reorganization during life [107]. The antibody assay was performed at days 7 and 14 post-transfection. Prior to PSA-NCAM Ab treatment, cells were washed 3 times with 100 µL of pre-warmed PBS. Next, they were blocked with 100 µL of bovine serum albumin (BSA) blocking buffer for 10 min at room temperature. During this incubation, the PSA-NCAM Ab was diluted in the buffer at a 1:100 ratio. Following the removal of the BSA buffer, 100 µL of the diluted antibody was added to the wells, and the cells were incubated for at least 30 min in the dark. After incubation, cells were washed 3 times with 100 µL PBS and assessed using allophycocyanin (APC) laser in flow cytometry to determine the percentage of cells bound to the PSA-NCAM Ab.

In addition to staining reprogrammed cells, PSA-NCAM Ab was also used to stain immature neurons at day 0, day 2, and day 14 to validate the system as a positive control.

3.4 Statistical Analysis

Due to the exploratory nature of this research, data collected from several experiments was assessed qualitatively or summarized using descriptive statistics rather than formal hypothesis testing. Most experiments were conducted with a limited number of replicates (n = 3 per group), which restricts the ability to reliably assess assumptions required for parametric statistical tests, such as normality and homogeneity of variance. While non-parametric tests could be considered, the small sample size greatly limits statistical power and reduces the reliability of statistical significance observed during testing. Therefore, data are presented as individual data points, with central tendency indicated by the median and variability represented by the full data range. This approach prioritizes transparency and allows visualization of biological variability without overinterpretation of underpowered datasets. Therefore, in cases where statistical significance could not be calculated, qualitative visualization through fluorescence microscopy or through bar plots was used to identify trends in data for future optimization.

4. Results and Discussion

4.1 Objective #1: Design, Construct and Characterise Miniphagemid Vectors Carrying *NeuroD1* Transcription Factor, Tissue-Specific Promoter, and Targeting Peptides.

4.1.1 Plasmid Sequence Verification

In order to verify the sequence of the constructs used for miniphagemid production, the plasmids were subjected to double restriction digestion (Appendix D) and sequencing analysis assessed via Smith-Waterman local alignment of Nanopore sequencing reads (Table 8). Sequence validation of the plasmids was performed using Oxford Nanopore R10.4.1 chemistry and the super high accuracy (SUP) basecalling model. An average assembly coverage of 120x was achieved, exceeding the 95% expected coverage threshold. Assembly was performed using Canu, ensuring high consensus identity (>99%) for the verification.

The results showed good structural integrity across the majority of the samples. All helper plasmids demonstrated good sequence homology (>98–99%) with only minor alignment gaps and point mutations observed within these constructs. Some of these discrepancies could also be Nanopore sequencing artifacts such as reading errors within homopolymeric regions [108].

In contrast, constructs such as pAI1 and Flex Switch showed suboptimal alignment identities coupled with large deletions. Given that the Smith-Waterman algorithm is optimized for local alignment, those sequences were re-aligned using semi-global alignment which has revealed deletions of large regions. These discrepancies are likely due to large-scale recombination events during bacterial amplification.

Table 8: Plasmid DNA Sequence Local Alignment Scores

Plasmid	Alignment Method	Identity (%)	Notes
pAI1	Semi-global	Range 1: 99 Range 2: 0 Range 3: 100	Large scale deletion of *M13 STOP* (5,774 bp – 5,972 bp – range 2)
pAI2	Local	100	None
pAI3	Local	99.98	1 gap in *GFP* (0.02%)
pJL1	Local	99.97	2 gaps in *hGFAP* (0.03%)
pJL2	Local	100	None
pJL3	Local	99.97	1 gap (0.01%) in *hGFAP*
Flex Switch	Semi-global	Range 1 100 Range 2 0 Range 3 99	Large scale deletion of *loxP, dTomato, 3'UTR, SSeq, M13 STOP* (5,850 bp - 7,302 bp – range 2)
pLuNe	Local	98.31	67 gaps (1.60%) in polyA tail
p326	Local	98.73	68 gaps in polyA tail (1.27%)
EF-1α-dTomato	Local	99.90	4 point mutations in *f1 ori*
pM13ori2-cmv-luc	Local	99.98	1 point mutation in CMV enhancer
SW8-IRL1620	Local	99.93	Point mutation in *gVIII, gIII*
SW8-EGF	Local	99.08	41 gaps (0.7%) scattered across *gVIII, gIII, and gIV*
SW8-EGFSF	Local	99.34	38 gaps (0.49%) in *gIX*, *gVIII*, some point mutations in *gIV*
SW8-SF	Local	99.86	3 gaps (0.07%) in *gIII*
SW8-SG	Local	99.32	36 gaps (0.49%) in *gVIII, gIII, gIV,*
SW8-SL	Local	99.18	34 gaps (0.62%) in *gIV*

4.1.2 Immunoblot Analysis for Miniphagemids

To confirm the presence of miniphagemids with properly formed pIII coat proteins, a dot blot was performed on all the produced miniphagemid samples. The dot blot results show detectable M13 pIII minor capsid protein in the AI, JL, Flex-EGF, and LuNe miniphagemid samples, suggesting possibly well-formed vectors with potential capacity for targeting (Figure 8-A, B). Detection of pIII suggests incorporation of this protein into the phage capsid; however, dot blot doesn't assess its infectivity, cell targeting, or DNA packaging. In contrast, the Flex-IRL1620 miniphagemid sample did not produce a detectable signal, suggesting unsuccessful miniphagemid production, or a significantly lower yield relative to the other samples. Given that MADLS assay on the Flex-IRL1620 samples showed presence of appropriately sized particles (Table 10), the absence of pIII signal is also possible due to the obstruction of the binding site for anti-pIII Ab by IRL-1620 display. The antibody used (M13 phage coat E1) is frequently applied for screening phage display libraries, suggesting that it binds pIII even in the presence of N-terminal fusions. Unless specific properties of the IRL-1620 ligand can spontaneously induce a conformational change to mask pIII by preventing antibody binding, perhaps it is more likely that the lack of signal is due to miniphagemid yield falling below the detection limit of the assay. This could also explain the low signal intensity for Flex-EGF. The TN buffer negative control showed no signal, suggesting that the observed signal in samples is not due to the background noise. Variability in signal intensity was observed across the samples, which is likely due to differences in miniphagemid yield or PEG precipitation efficiency.

To confirm the EGF display on miniphagemids, a dot blot was performed on all the produced EGF displaying miniphagemids. The dot blot results show detectable EGF protein in all miniphagemid samples expected to display the ligand, suggesting the presence of EGF on the miniphagemid capsid (Figure 8-C). This indicates that the ligand is displayed on the capsid;

however, this assay doesn't evaluate EGF functionality. The TN buffer and non-display miniphagemid negative controls showed no signal, suggesting that the observed signal was not due to the background noise or nonspecific antibody binding to the phage capsid. As with the previous dot blot, some variability in signal intensity was observed across samples.

Since the samples were loaded in equal volume rather than normalized by concentration, the observed variation in signal likely reflects differences in phage production yield between different constructs or phage display efficiency. After visual comparison of signal intensities across the dot blots, AI miniphagemids demonstrated strong signals in both anti-pIII and anti-EGF assays, suggesting they have high production titers and efficient ligand display. In contrast, JL miniphagemids showed strong pIII signal but much weaker EGF signal, suggesting that while it allows for high-titer phage production, ligand display is inefficient or unstable. Flex miniphagemids showed significantly lower signals in the anti-pIII blot suggesting that Flex has a much lower packaging or production efficiency compared to AI or JL miniphagemids.

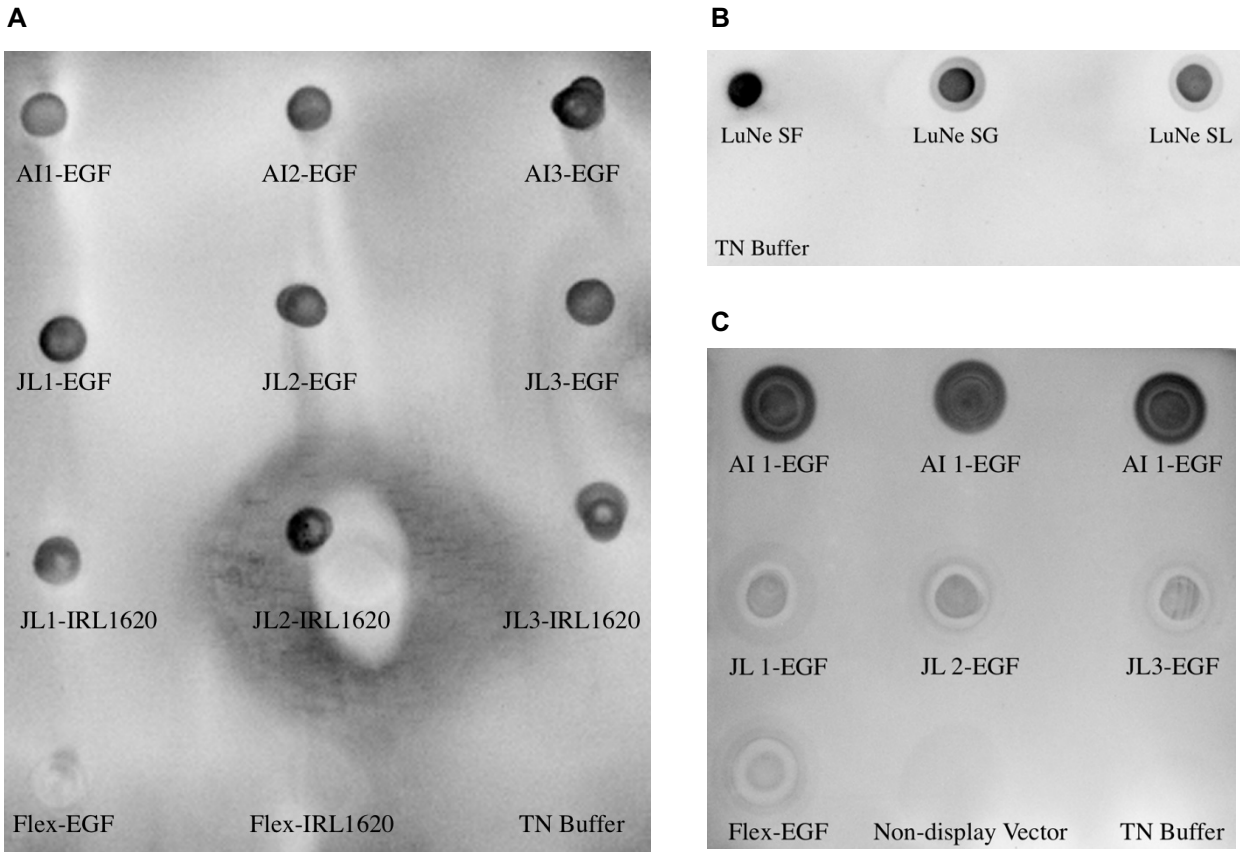


Figure 8: Dot Blot on Miniphagemids Staining for EGF Display and M13 Capsid Protein pIII

Dot blot analysis for the presence of miniphagemids via detection of M13 pIII capsid protein. 5 µL of miniphagemid samples were spotted onto a nitrocellulose membrane, with TN buffer included as a negative control. The membrane was probed with an anti-M13 pIII primary Ab followed by an HRP-conjugated secondary Ab. Signal was visualized using chemiluminescent substrate via iBright (A). Dot blot analysis for the presence of LuNe miniphagemids via detection of M13 pIII capsid protein. 5 µL of LuNe miniphagemid samples were spotted onto a nitrocellulose membrane, with TN buffer included as a negative control. The membrane was probed with an anti-M13 pIII primary Ab followed by an HRP-conjugated secondary Ab. Signal was visualized using chemiluminescent substrate via iBright (B). Dot blot analysis for the presence of EGF display on miniphagemids. 5 µL of miniphagemid samples were spotted onto a nitrocellulose membrane, with TN buffer included as a negative control. The membrane was probed with an anti-EGF primary Ab followed by an HRP-conjugated secondary Ab. Signal was visualized using chemiluminescent substrate via iBright (C).

4.1.3 Purification of the single-stranded Miniphagemid DNA

Table 9: Expected Sizes of Miniphagemid Genomes

Miniphagemid Precursor Plasmid	Expected ssDNA Size (kb)
pAI1	3.1
pAI2	2.5
pAI3	2.5
pJL1	3.5
pJL2	2.9
pJL3	2.9
Flex Switch	3.8
pLuNe	3.1

To investigate the genome carried by the produced miniphagemids (Table 4) their ssDNA was extracted using phenol-chloroform method and ran on AGE (Figure 9) where each lane corresponds to one miniphagemid type produced. White bands seen on the gel represent stained DNA molecules that have migrated through the agarose gel and glow when subjected to the UV light due to DNA labelling dye. Most of the observed results are consistent with the expected fragment sizes, suggesting that the miniphagemids could carry correct genome sequence with respect to their precursor plasmids. Importantly, this analysis only shows the overall genome size, DNA sequencing would be required for full genome verification. In addition, some miniphagemids such as AI3-EGF, Flex-EGF, Flex-IRL1620, and JL-EGFSF have resulted in no bands. The absence of visible ssDNA bands may be due to low ssDNA yield, or unsuccessful staining since ssDNA has fewer dye binding sites compared to dsDNA. Therefore, this does not necessarily indicate incorrect DNA packaging in a miniphagemid. LuNe-SF, LuNe-SG, and LuNe-SL resulted in faster bands that did not exactly match the expectations. This may have been due to circular

ssDNA forming secondary structures which cause it to migrate non-proportionally relative to dsDNA size ladder. In addition, most bands appear tight and distinct which suggests successful extraction of a homogenous DNA molecules. It can be observed that some ssDNA bands appear much brighter than others, this could be due to differences in DNA concentrations loaded onto the gel since extracts from miniphagemids were not standardized prior to assay. While exact ssDNA size determination through AGE is limited, relative migration patterns were consistent with the expected DNA sizes, supporting the identity of tested miniphagemids.

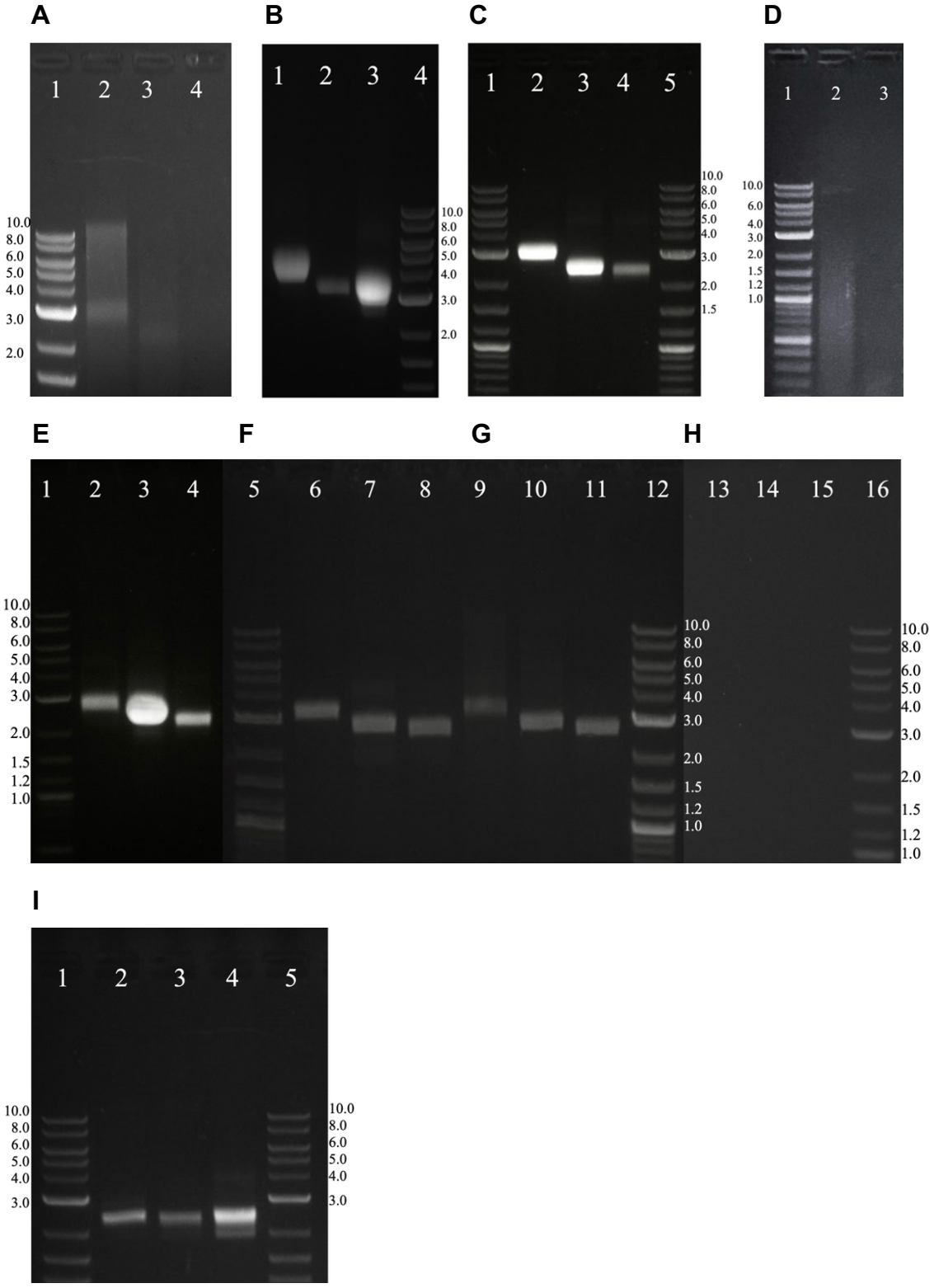


Figure 9: Agarose Gel Electrophoresis of Extracted Single-Stranded DNA from All Produced Miniphagemids

ssDNA extracted from AI1, AI2, AI3 with EGF (A); Flex Switch with EGF and IRL1620 (D); JL1, JL2, JL3 with EGF (B), IRL1620 (C), SF (E), SG (F), SL (G), and EGFSF (H); LuNe with SF, SG, and SL (I) miniphagemids using phenol-chloroform extraction method was run on 0.8% agarose gel.
A) Lane 1: 1kb plus DNA Ladder labelled in kb. Lane 2: AI1 ssDNA; Lane 3: AI2 ssDNA. Lane 4: AI3 ssDNA.

B) Lane 1: JL1 EGF ssDNA, lane 2: JL2 EGF ssDNA, lane 3: JL3 EGF ssDNA, lane 4: 1kb plus DNA Ladder labelled in kb.
C) Lane 1 & 5: 1kb plus DNA Ladder labelled in kb, lane 2: JL1 IRL1620 ssDNA, lane 3: JL2 IRL1620 ssDNA, lane 4: JL3 IRL1620 ssDNA.
D) Lane 1: 1 kb plus DNA Ladder labelled in kb, lane 2: Flex EGF ssDNA, lane 3: Flex IRL1620ssDNA.
E) Lane 1: 1kb plus DNA Ladder labelled in kb, lane 2: JL1 SF ssDNA, lane 3: JL2 SF ssDNA, lane 4: JL3 SF ssDNA.
F) Lane 5 & 12: 1kb plus DNA Ladder labelled in kb, lane 6: JL1 SG ssDNA, lane 7: JL2 SG ssDNA, lane 8: JL3 SG ssDNA.
G) Lane 9: JL1 SL ssDNA, lane 10: JL2 SL ssDNA, lane 11: JL3 SL ssDNA.
H) Lane 13: JL1 EGFSF ssDNA, lane 14: JL2 EGFSF ssDNA, lane 15: JL3 EGFSF ssDNA, lane 16: 1kb plus DNA Ladder labelled in kb.
I) Lane 1&5: 1kb plus DNA Ladder labelled in kb, lane 2: LuNe SF ssDNA, lane 3: LuNe SG ssDNA, lane 4: LuNe SL ssDNA.

4.1.4 Quantifying Miniphagemids via Multi-Angle Dynamic Light Scattering and UV–Visible Spectrophotometry

Miniphagemid concentration, size and polydispersity were assessed using MADLS (Table 10). To gain confidence in the obtained values, MADLS results were compared to the concentration estimates obtained by OD measured through UV-visible spectrophotometry, Table 10. The values were generally consistent across the miniphagemid samples where both values were available. For the AI-EGF constructs, MADLS and OD derived concentrations were within one order of magnitude (10^{11} - 10^{12} phage/mL), indicating reasonably good agreement between the two methods.

Previous studies using diffusion-based assessment methods for bacteriophages have shown hydrodynamic diameters around 100 nm, making this the expected size for the miniphagemids in this project [109]. Miniphagemids are rod-shaped; however, the MADLS algorithms use the Stokes-Einstein equation to calculate hydrodynamic diameter assuming a spherical shape [96,97]. Therefore, the values reported here do not represent a precise miniphagemid width or length, but rather the diameter of a theoretical sphere that diffuses at the same rate. Therefore, the output values are

consistent with the hydrodynamic behavior expected from elongated particles, representing the length of the rotating miniphagemid rather than their width.

For most samples particle sizes fell within the expected range: 90 - 170 nm, suggesting successful particle formation. However, some samples showed significantly larger sizes, including JL3-EGF and Flex-EGF, which had sizes exceeding 300 nm. This is likely due to particle aggregation, incomplete assembly or improper genome packaging.

Estimated concentrations varied across samples, ranging from 10^{10} to 10^{13} phage/mL indicating significant variation in production efficiency of different constructs. However, many samples showed comparable concentrations within each construct group. Therefore, production efficiency is construct-dependent. In addition, samples with larger hydrodynamic sizes did not consistently present higher concentrations, suggesting that increased particle size is not necessarily associated with higher miniphagemid yield.

By collecting data from multiple angles, MADLS also allows detection of polydispersity (expressed in PDI) of the sample, which is the variation of the particle sizes in the sample. High PDI (0.7) indicates a wide range of sizes, while low PDI (0.3) indicates a uniform size [96,97]. PDI values for most samples ranged between 0.20 and 0.40, consistent with moderately dispersed populations.

Overall, these results suggest that while the majority of miniphagemid samples contain particles within the expected size range, there is variability in size distribution and concentration across constructs. Therefore, additional characterization methods are required to further assess miniphagemid integrity and suitability for gene delivery.

Table 10: Miniphagemid Size and Concentration Estimated Using MADLS

Miniphagemid sample	Size (nm)	Concentration (phage/mL)		Polydispersity Index (PDI)
		MADLS	OD	
AI1-EGF	103.8	10^{12}	10^{11}	0.24
AI2-EGF	174.6	10^{12}	10^{12}	0.29
AI3-EGF	163.5	10^{12}	10^{12}	0.28
JL1-EGF	125	10^{13}	-	0.32
JL2-EGF	148.9	10^{13}	-	0.27
JL3-EGF	336.4	10^{13}	-	0.35
JL1-IRL1620	157.2	10^{12}	-	0.34
JL2-IRL1620	153.4	10^{13}	-	0.38
JL3-IRL1620	157.8	10^{11}	-	0.40
Flex -EGF	318.9	10^{10}	-	0.34
Flex-IRL1620	127.6	10^{10}	-	0.21
JL1-SF	146	10^{10}	-	0.18
JL2-SF	131.3	10^{11}	-	0.34
JL3-SF	132.8	10^{10}	-	0.24
JL1-SG	110.1	10^{11}	-	0.26
JL2-SG	118.7	10^{10}	-	0.20
JL3-SG	113.5	10^{11}	-	0.24
JL1-SL	138.5	10^{11}	-	0.33
JL2-SL	100.3	10^{13}	-	0.27
JL3-SL	133.1	10^{10}	-	0.29
JL1-EGFSF	121.5	10^{10}	-	0.3
JL2-EGFSF	120.1	10^{12}	-	0.25
JL3-EGFSF	176.3	10^{10}	-	0.34
LuNe-SF	95.9	10^{13}	-	0.32
LuNe-SG	103.73	10^{13}	-	0.28
LuNe-SL	90.53	10^{13}	-	0.25

4.1.5 Assessing Backbone Contamination via Colony Assay

It was expected that the iPhAGE system will produce high titres of miniphagemids with quality ssDNA. The packaged DNA should also have minimal contamination from prokaryotic DNA, which was assessed using the colony assay. Miniphagemids were screened for the presence of *nptII* (kanamycin resistance), *bla* (ampicillin resistance), or both, which would indicate incorporation of non-target plasmid DNA. Properly packaged miniphagemids, containing only the intended cassette, are not expected to present antibiotic resistance. Based on prior reports, filamentous phage systems that eliminate helper plasmid packaging through the deletion of the packaging-signal, show helper plasmid contamination at levels frequently below 1% of the total yield or at undetectable levels [63]. Therefore, the miniphagemid samples are expected to show negligible contamination from the helper plasmid and bacterial backbone DNA.

As anticipated, the iPhAGE system produced high-titre miniphagemid vectors with very low levels of contamination from bacterial backbone sequences, as assessed by the colony assay (Table 11). For the majority of the samples, no antibiotic-resistant colonies were observed, meaning contamination levels were below the detection limits of the assay ranging from $< 2 \times 10^{-7}$ % to. $< 2 \times 10^{-10}$ %, depending on the initial titre, indicating minimal carryover of prokaryotic DNA. These findings are consistent with the design of the iPhAGE system, which only packages ssDNA derived from the miniphagemid excluding bacterial backbone elements.

Miniphagemids produced at higher titres (10^{12} - 10^{13} phage/mL), such as the LuNe and several JL vectors, showed contamination efficiencies below the assay's limit of detection, getting as low as $<2 \times 10^{-10}$ % across all antibiotic selection conditions (Amp, Kan, and Amp + Kan). The absence of colonies on these selective plates suggests that the iPhAGE system provides good DNA purity and efficiently excludes non-target plasmid DNA, even at high particle yields. For constructs

produced at lower titres (10^{10} - 10^{11} phage/mL), such as the Flex Switch and SF/SG/SL variants, contamination was similarly undetectable in the majority of samples. While the calculated limits of detection for these constructs appear higher, typically ranging from $<2 \times 10^{-7}$ % to $<2 \times 10^{-8}$ %, this is not due to a decrease in packaging reliability, but a proportional effect of the colony assay. Because the total number of phage particles plated is lower for these samples, the minimum detectable contamination threshold proportionally increases.

Despite the generally undetectable levels of prokaryotic DNA contamination across the constructs, a few outliers were observed. Most notably, JL3 SG under ampicillin selection showed a contamination efficiency of 4×10^{-5} %. This may be due to random events of full precursor plasmid packaging rather than a general production failure.

In conclusion, the iPhAGE system produced high-titre miniphagemids with negligible prokaryotic DNA contamination. With the exception of rare outliers, most samples had contamination efficiencies below detection limits. These findings suggest that this system primarily excludes bacterial backbone elements from being packaged into miniphagemid vectors.

Table 11: Contamination Efficiency of Miniphagemids Based on the Colony Assay

Miniphagemid sample	Concentration (phage/mL)	Contamination (%)		
		Amp	Kan	Amp + Kan
AI1-EGF	10^{12}	6×10^{-9}	$<2 \times 10^{-9}$	$<2 \times 10^{-9}$
AI2-EGF	10^{12}	1×10^{-8}	$<2 \times 10^{-9}$	$<2 \times 10^{-9}$
AI3-EGF	10^{12}	2×10^{-9}	$<2 \times 10^{-9}$	$<2 \times 10^{-9}$
JL1-EGF	10^{13}	2×10^{-10}	$<2 \times 10^{-10}$	$<2 \times 10^{-10}$
JL2-EGF	10^{13}	$<2 \times 10^{-10}$	$<2 \times 10^{-10}$	$<2 \times 10^{-10}$
JL3-EGF	10^{13}	$<2 \times 10^{-10}$	$<2 \times 10^{-10}$	$<2 \times 10^{-10}$
JL1-IRL1620	10^{12}	$<2 \times 10^{-9}$	$<2 \times 10^{-9}$	$<2 \times 10^{-9}$
JL2-IRL1620	10^{13}	$<2 \times 10^{-10}$	$<2 \times 10^{-10}$	$<2 \times 10^{-10}$
JL3-IRL1620	10^{11}	$<2 \times 10^{-8}$	$<2 \times 10^{-8}$	$<2 \times 10^{-8}$
Flex -EGF	10^{10}	$<2 \times 10^{-7}$	$<2 \times 10^{-7}$	$<2 \times 10^{-7}$
Flex-IRL1620	10^{10}	$<2 \times 10^{-7}$	$<2 \times 10^{-7}$	$<2 \times 10^{-7}$
JL1-SF	10^{10}	$<2 \times 10^{-7}$	4×10^{-7}	$<2 \times 10^{-7}$
JL2-SF	10^{11}	$<2 \times 10^{-8}$	6×10^{-7}	$<2 \times 10^{-8}$
JL3-SF	10^{10}	$<2 \times 10^{-7}$	$<2 \times 10^{-7}$	$<2 \times 10^{-7}$
JL1-SG	10^{11}	4×10^{-8}	$<2 \times 10^{-8}$	$<2 \times 10^{-8}$
JL2-SG	10^{10}	$<2 \times 10^{-7}$	$<2 \times 10^{-7}$	$<2 \times 10^{-7}$
JL3-SG	10^{11}	4×10^{-5}	$<2 \times 10^{-8}$	$<2 \times 10^{-8}$
JL1-SL	10^{11}	2×10^{-8}	$<2 \times 10^{-8}$	$<2 \times 10^{-8}$
JL2-SL	10^{13}	$<2 \times 10^{-10}$	$<2 \times 10^{-10}$	$<2 \times 10^{-10}$
JL3-SL	10^{10}	2×10^{-7}	$<2 \times 10^{-7}$	$<2 \times 10^{-7}$
JL1-EGFSF	10^{10}	$<2 \times 10^{-7}$	$<2 \times 10^{-7}$	4×10^{-7}
JL2-EGFSF	10^{12}	$<2 \times 10^{-9}$	$<2 \times 10^{-9}$	$<2 \times 10^{-9}$
JL3-EGFSF	10^{10}	$<2 \times 10^{-7}$	$<2 \times 10^{-7}$	$<2 \times 10^{-7}$
LuNe-SF	10^{13}	$<2 \times 10^{-10}$	$<2 \times 10^{-10}$	$<2 \times 10^{-10}$
LuNe-SG	10^{13}	$<2 \times 10^{-10}$	$<2x10^{-10}$	$<2 \times 10^{-10}$
LuNe-SL	10^{13}	$<2 \times 10^{-10}$	$<2 \times 10^{-10}$	$<2 \times 10^{-10}$

4.1.6 Summary of Results for Objective 1: Design, Construct and Characterise Miniphagemid Vectors Carrying *NeuroD1* Transcription Factor, Tissue-Specific Promoter, and Targeting Peptides.

Overall, the data on miniphagemid vectors indicate that this system can produce particles carrying genome of the expected size with low levels of prokaryotic DNA contamination. This can be concluded based on the following assays and results. Dot blot assays detected M13 capsid protein pIII and EGF ligand display in most samples, suggesting that some of the produced particles contain one of the M13 capsid proteins meaning that the rest of the capsid protein are also present to form the complete vector, however variability in signal intensity and the absence of signal in certain constructs suggest differences in production efficiency. Agarose gel analysis of ssDNA showed bands consistent with expected genome sizes for most miniphagemids, but inconsistent or absent bands in some samples potentially due to technical limitations of ssDNA visualization or variability in yield or construct. MADLS measurements demonstrated particle sizes mostly within the expected range for phage-derived vectors, but construct dependent variation in size, concentration, and polydispersity was observed. Colony assays showed that most miniphagemid preparations contained prokaryotic DNA at or below detection limits, with rare outliers. Overall, these findings suggest that miniphagemids can be produced.

4.2 Objective #2: Assess the Gene Delivery Efficiency to Target Cells by Quantifying Reporter Gene Activity.

To evaluate the success of miniphagemid-mediated gene delivery, reporter gene expression was quantified as a representation for cellular entry and expression of the *NeuroD1* transcription factor. Although direct detection of the NeuroD1 production was not performed in this project, the miniphagemid constructs were designed such that the reporter genes (*GFP, dTomato,* etc.) are encoded downstream of the *NeuroD1* sequence through 2 P2A linkers. Therefore, the detection of the reporter signal not only indicates successfully DNA delivery to the target cell, but also strongly suggests that the upstream *NeuroD1* gene is being co-expressed.

4.2.1 Transfection of A7 Astrocyte Cells with Plasmids Containing Transcription Factor Genes for Astrocyte Reprogramming

Figure 10 shows representative fluorescence microscopy images of A7 cells transfected with precursor plasmids encoding fluorescent reporter genes. Plasmids p326, pAI1, pAI2, and pAI3 encode the *GFP* gene, resulting in green fluorescence upon excitation at 488 nm, while EF-1α-dTomato and Flex Switch plasmids encode *dTomato*, producing red fluorescence upon excitation at 554 nm. In these images, individual GFP or dTomato-positive cells are visible and are marked with circles. The presence of fluorescent cells indicates that a subset of A7 cells successfully internalized the plasmid DNA and expressed the reporter gene under the control of the corresponding promoter. However, fluorescence appears to be low and unevenly distributed across the field of view for precursor plasmids, particularly when compared to the positive control constructs. While fluorescence microscopy provides direct visual confirmation of reporter gene expression, it is only qualitative and has certain limitations such as uneven illumination or background fluorescence. As a result, these images were used primarily to confirm expression

rather than to quantify the efficiency. To obtain a more reliable and quantitative assessment of reporter expression, the same samples were analyzed by flow cytometry.

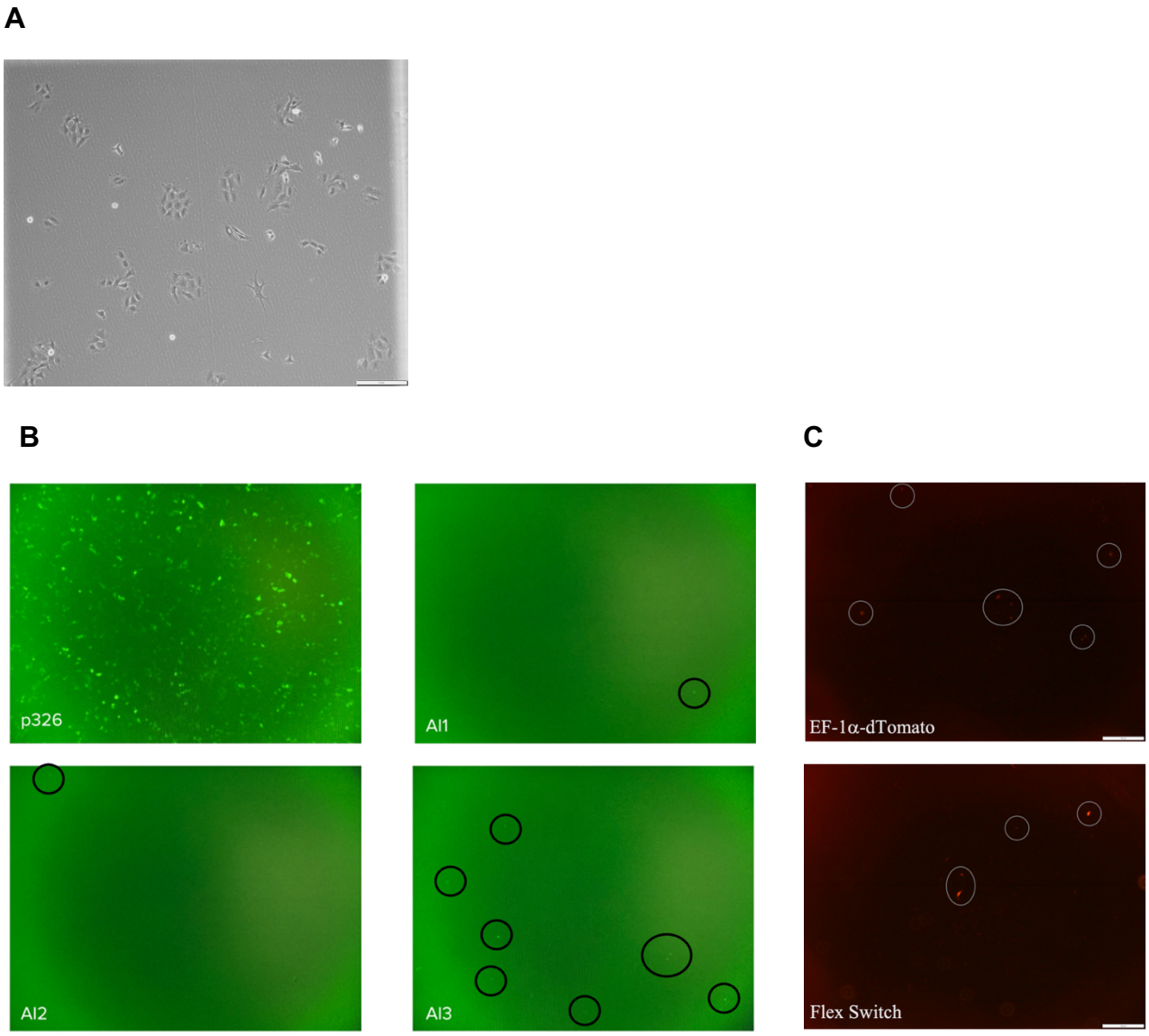


Figure 10: Visualizing *GFP* and *dTomato* Expression in A7 Cells Transfected with Precursor Plasmids

Immortalized A7 rat astrocytes in cell culture at passage 9, 24 h after passaging. Imaged at 40X magnification (A). A7 cells were transfected with precursor plasmids encoding fluorescent markers. The p326, AI1, AI2, and AI3 plasmids encode the *GFP* gene which results in the production of GFP, this protein fluoresces green when excited with light of 488 nm wavelength [110]. Cells that successfully took up these plasmids are circled in black (B). The EF-1α-dTomato and Flex Switch plasmids encode *dTomato* gene resulting in the production of dTomato protein, which fluoresces red when excited with light of 554 nm wavelength [111]. Cells that successfully took up those plasmids are circled in grey (C). A transfection reagent, Lipofectamine was added to each sample, and images were taken at 72 h post-transfection at 40X total magnification.

Figure 11 shows flow cytometry data quantification of fluorescent reporter expression in A7 cells transfected with precursor plasmids, compared to their respective positive controls. Figure 11-A compares *GFP* expression in cells transfected with pAI1, pAI2, and pAI3 plasmids relative to the p326 positive control. Figure 11-B compares *dTomato* expression in cells transfected with the Flex Switch plasmid relative to the EF-1α-dTomato positive control. In both cases, A7 cells transfected with precursor plasmids showed detectable but lower levels of reporter gene expression compared to positive control plasmids. In all cases, the proportion of fluorescent cells remained below the commonly used threshold of 10% for transgene expression. In contrast, positive control plasmids driven by strong EF-1α promoter allowed for higher expression, confirming that the Lipofectamine transfection protocol and assay methods were fully functional.

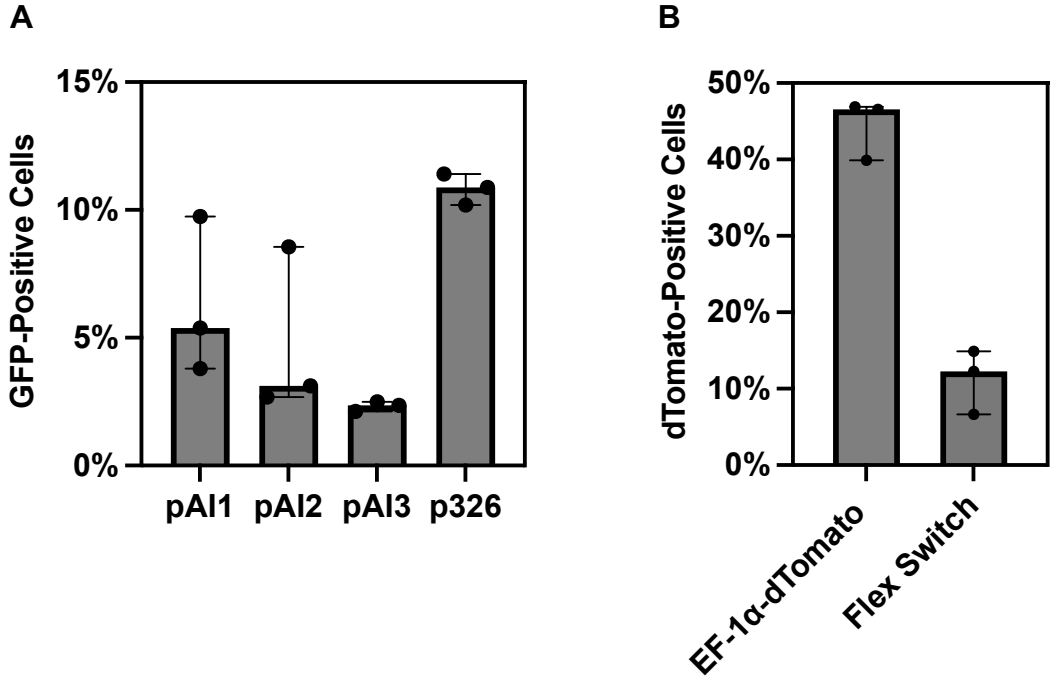


Figure 11: Percentage of Fluorescent Marker-Positive A7 Cells

Figure contains a bar plot comparing *GFP* expression in A7 cells transfected with pAI1, pAI2, and pAI3 precursor plasmids, and the p326 positive control plasmid (n = 3) (A). Figure also contains a bar plot comparing *dTomato* expression in A7 cells transfected with Flex Switch precursor plasmid, and EF-1α-dTomato positive control plasmid (n = 3) (B). A transfection reagent, Lipofectamine was added to each sample, and measurements were taken at 72 h post-transfection. Negative control cells showed ≤1% fluorescent marker-positive cells and are not shown for clarity. Data are presented as data points with bars at the median percentage of fluorescent cells.

Figure 12 presents a quantitative comparison of *luciferase* expression in A7 cells transfected with pJL1, pJL2, pJL3, and pLuNe precursor plasmids, alongside the pM13ori2-cmv-luc positive control plasmid. Consistent with fluorescence gene analyses, luciferase activity was detected in cells transfected with precursor plasmids but was much lower than the signal for the positive control plasmid which produced the highest luminescence reading, suggesting more efficient expression. In contrast, precursor plasmids showed lower reporter output, suggesting limited expression or worse DNA entry.

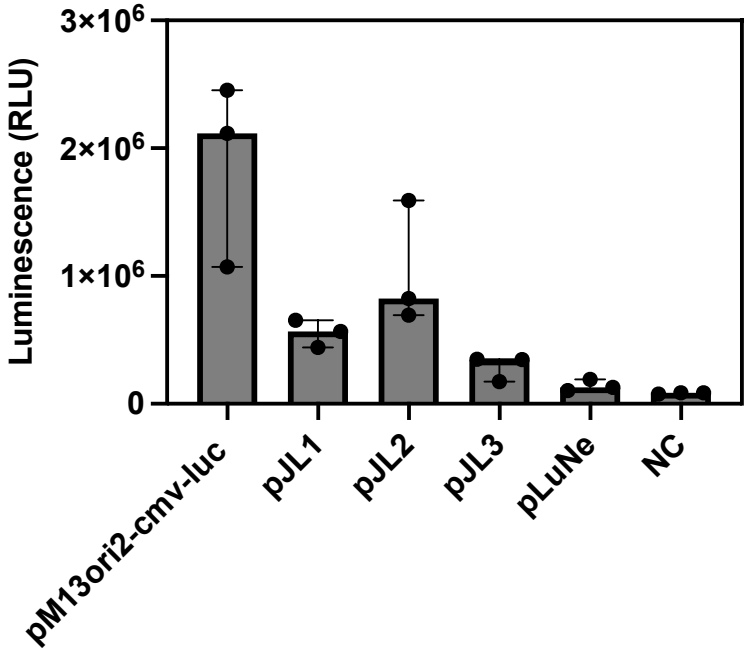


Figure 12: Firefly Luciferase Reporter Activity in A7 Cells

Luciferase activity measured in A7 cells following transfection with pJL1, pJL2, pJL3, pLuNe precursor plasmids, and the pM13ori2-CMV-luc positive control ($n = 3$). Luminescence was measured at 72 h. Data are presented as data points with bars indicating the median.

Since the precursor constructs and the control plasmids are comparable in size (Table 3), the observed reduction in reporter signal can't be due to the size-dependent differences in transfection efficiency. Instead, this could be due to limitations in promoter recognition and backbone design. For constructs encoding the human GFAP promoter, reduced expression is likely due to species mismatch as A7 cells are immortalized embryonic rat astrocytes (ATCC, Manassas,

USA), which may lack the transcriptional machinery required to fully activate a human astrocyte promoter. In addition, even for precursor plasmids encoding the universal CMV promoter, the specific backbones may lack required enhancer elements or be subjected to intracellular silencing. One major factor is intracellular silencing through unmethylated CpG motifs. Precursor plasmids contain bacterial backbone components, such as *ori* and *bla*, which are rich in unmethylated CpG motifs. The mammalian innate immune system would recognize these prokaryotic sequences as being pathogen-associated; therefore, their presence can lead to active gene silencing [112,113]. This could explain the low reporter gene expression observed from precursor plasmids, even if the DNA was successfully internalized.

These results suggest that although the flow cytometry assay is effective, reporter gene expression from the precursor plasmids is limited. Since reporter output depends on both successful DNA entry and subsequent gene expression, it is unclear whether this limitation comes from inefficient cellular uptake or from poor downstream expression. To distinguish between these possibilities and confirm successful DNA entry, it was necessary to assess DNA uptake independently of reporter expression.

4.2.2 Assessing DNA Uptake by A7 Cells During Transfection

Since observed transfection efficiencies in A7 cells were consistently low (<10%) across multiple reporter constructs (Figure 11, Figure 12), an additional experiment was performed to determine if this limitation was due to inefficient plasmid DNA uptake or poor gene expression. To address this, pLuNe plasmid encoding the *mNeonGreen* reporter gene, was covalently labeled with a Cy3 tag using Label IT dye prior to transfection. This allowed for the direct visualization of DNA uptake independent of the *mNeonGreen* expression. Lipofectamine was used as the transfection reagent to form DNA-Lipofectamine complex. In this experiment, detection of red

Cy3 fluorescence within the cells without mNeonGreen signal would indicate that DNA was successfully taken up but not expressed.

As shown in Figure 13, a considerable proportion of both A375 and A7 cells showed detectable Cy3 fluorescence, indicating successful plasmid DNA uptake. As expected, the A375 positive control cells demonstrated higher uptake (~80%), while A7 cells still showed a relatively strong uptake rate (~60%). Consistent with this, A375 cells also showed higher *mNeonGreen* expression (~35%), suggesting that both DNA uptake and downstream gene expression are more permissive in this cell line. In contrast, although a considerable fraction of A7 cells internalized the plasmid, reporter gene expression remained low (<10%).

These results suggest that the low reporter gene signal observed in A7 cells is primarily not due to a failure in DNA uptake, but due to significant intracellular factors that limit expression. Cy3 signal suggests successful membrane penetration, but lack of mNeonGreen signal suggests that the DNA may remain trapped within endosomes or get lost in the cytoplasm.

A375 human melanoma cells are highly proliferative, with doubling time around 15 h [114]. This allows for frequent nuclear envelope breakdown during mitosis, providing an opportunity for cytoplasmic plasmids to gain passive access to the transcriptional machinery [115]. In contrast, the A7 cells have a significantly higher doubling time around 48 - 72 h [116]. Slower growth rate means that the nuclear envelope remains intact for longer making it harder for plasmids to enter passively and they must rely on the restrictive nuclear pore complex for entry [117]. In addition, as A7 cells are astrocyte-derived and specialize in clearance of extracellular debris and maintenance of CNS homeostasis [118, 119]. This could mean that their lysosomal system is more aggressive than in A375 and effectively destroys foreign DNA. The combination of increased time plasmid spends in the cytoplasm due to slower cell doubling and enhanced lysosomal activity may promote more rapid

degradation of plasmid DNA in A7 cells. In contrast, A375 cells, which divide more rapidly, may allow plasmid DNA to access the nucleus more efficiently before being degraded.

In conclusion, this experiment has confirmed successful DNA entry which strongly supports the hypothesis that intracellular mechanisms are likely interfering with DNA expression. Main factors for why A7 cells produce low reporter signal are likely the innate immune recognition of unmethylated CpG motifs in the bacterial backbone combined with long doubling time and aggressive lysosomal clearance. These aspects likely contribute to the inactivation of most of the plasmids internalized by A7 cells.

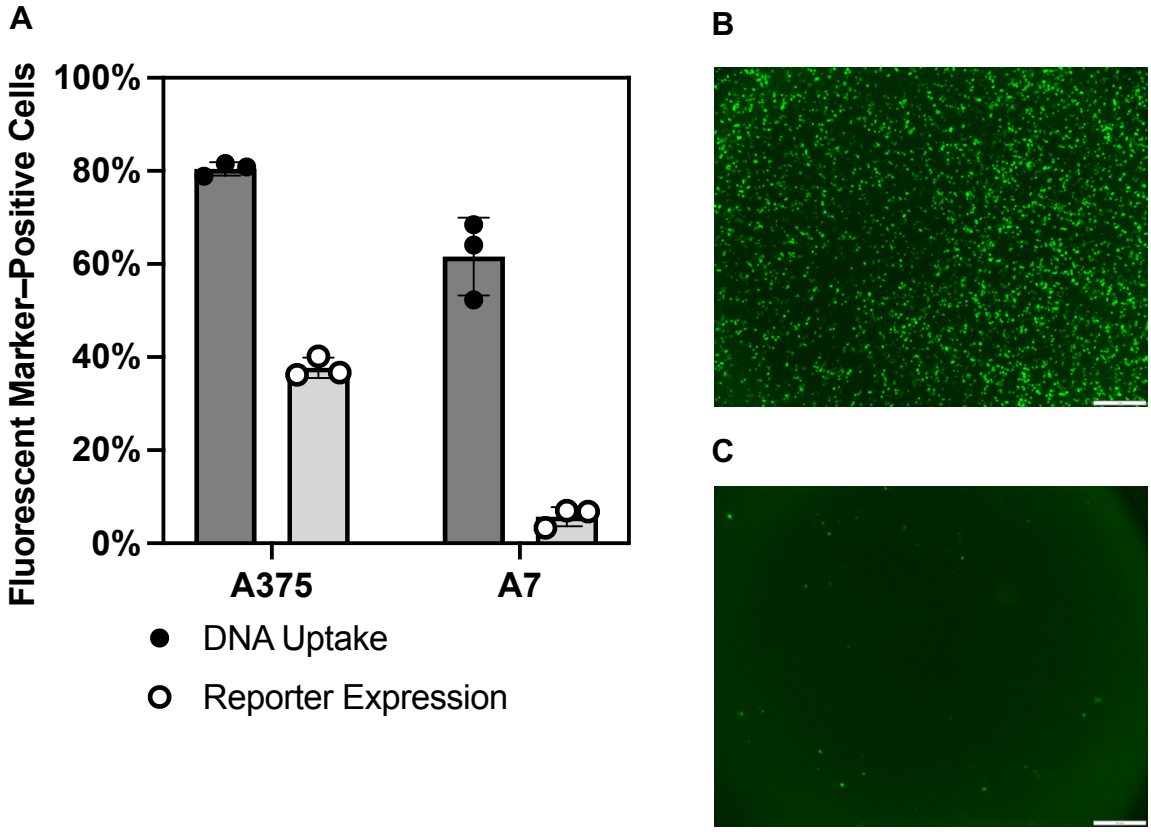


Figure 13: DNA Uptake and Reporter Gene Expression in A365 and A7 Cells

Figure contains a bar plot comparing transfection and expression efficiencies in A375 (PC) and A7 cells. They were transfected with pLuNe plasmid labeled with Cy3 to assess DNA uptake, while gene expression was measured by mNeonGreen signal (n = 3). Data are presented as data points with bars at the median percentage of fluorescent cells (A). *mNeonGreen* expression in A375 cells (B). *mNeonGreen* expression in A7 cells (C).

4.2.3 Assessing Activation of A7 Cells Through Morphological Changes

Figure 14 shows stitched light microscopy images of A7 cells after 24 h of LPS treatment at increasing concentrations (100, 200, and 300 ng/mL), alongside the untreated negative control cells. Visual inspection of the images suggests small morphological differences between untreated and LPS-treated cells. Untreated A7 cells have a more uniform and rounder appearance, while LPS-treated cells show heterogeneous morphology. However, dose-dependent morphological differences between the LPS-treated groups are not distinguishable by eye.

To assess morphological changes associated with activation of A7 cells, their circularity was measured using Cellpose segmentation tool and compared between treatments (Figure 15). Circularity can be used to describe cell shape, with higher values indicating a more rounded morphology [103]. Astrocyte activation is not a uniform process, and different activation stimuli can elicit distinct morphological responses [120]. As a result, reactive astrocytes may exhibit either increased or decreased circularity depending on the activation type.

In this experiment, cells were activated using LPS, which is a pro-inflammatory stimulus that triggers cytoskeletal remodeling [121]. Under these conditions, the circularity of treated cell has decreased. This is consistent with reactive astrocytes undergoing major morphological changes, such as hypertrophy and cytoskeletal reorganization, specifically an increase in branching and process complexity, which result in an increase in cell perimeter relative to the area [122]. Therefore, lower circularity suggests a more irregular morphology, process extension, and an increase in structural complexity [103]. The distribution of circularity values in A7 cells differed between untreated and LPS-treated groups. A chi-square test of independence showed a significant effect of LPS treatment on circularity distribution ($p = 8.07 \times 10^{-21}$), indicating that LPS treatment is linked to changes in cell morphology. Overall, LPS-treated A7 cells showed altered circularity compared to untreated controls.

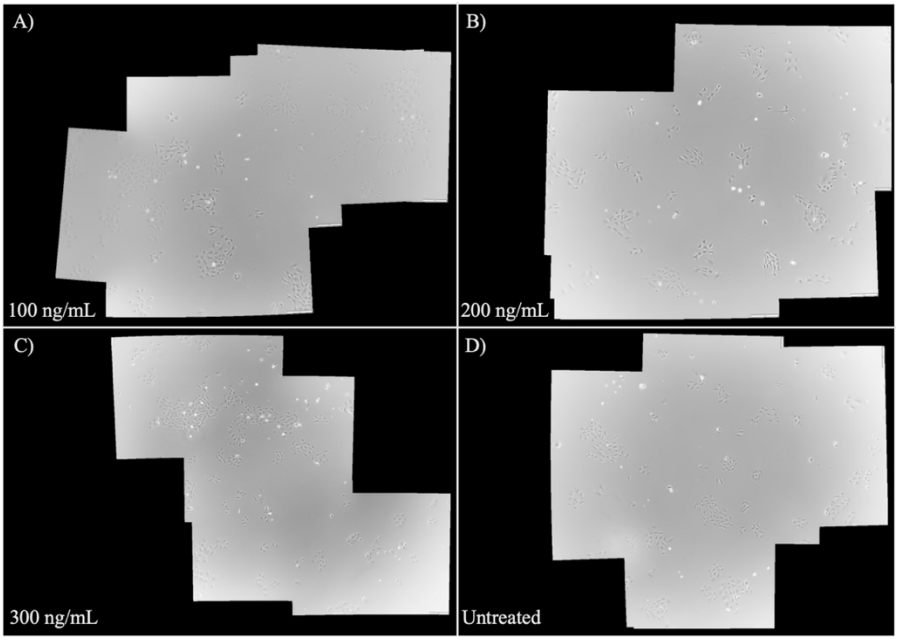


Figure 14: A7 Cells Treated with LPS at 24 h

Figure illustrates stitched light microscopy images of A7 astrocytes following 24 h of LPS treatment. Images show cells treated with 100 ng/mL (A), 200 ng/mL (B), and 300 ng/mL (C) LPS as well as untreated negative control cells (D). Multiple fields of view acquired at 40X magnification were stitched using OpenCV to generate a continuous image for each condition.

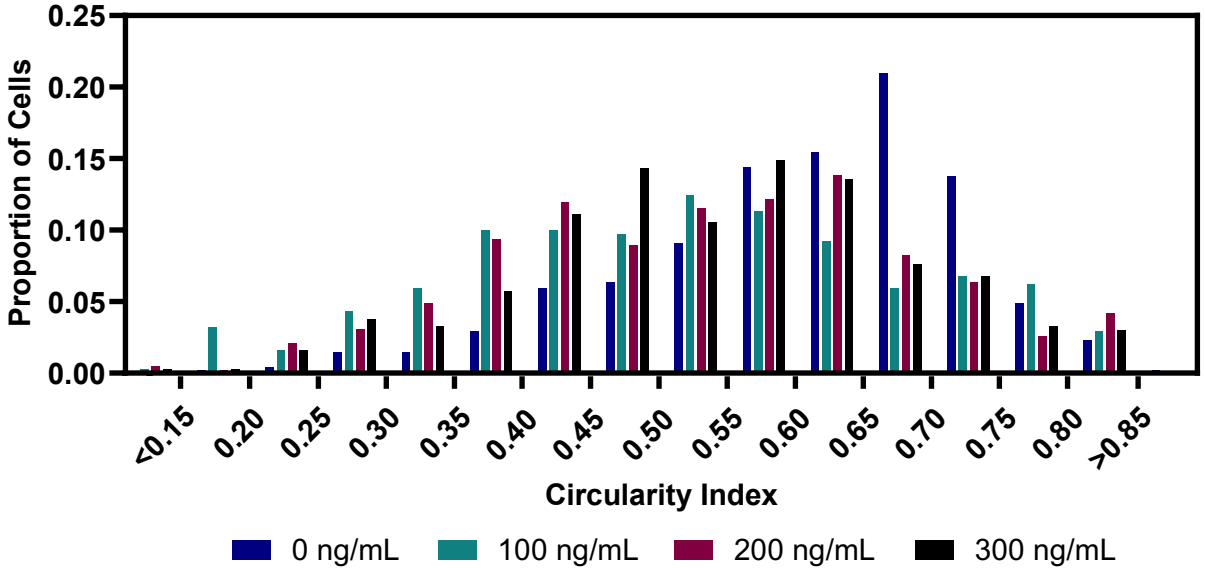


Figure 15: Effect of LPS Treatment on Circularity of A7 Cells

Distribution of circularity in A7 astrocytes following LPS treatment. Circularity values were binned, and the proportion of cells within each bin was calculated for untreated cells (0 ng/mL) and cells treated with 100, 200, or 300 ng/mL LPS. Bin counts were normalized to the total number of cells per condition (0 ng/mL – 472 cells, 100 ng/mL –370 cells, 200 ng/mL – 426 cells, 300 ng/mL – 369 cells).

Differences in circularity distributions across LPS treatment doses were then assessed using a chi-square test of independence. After observing a significant overall effect where p value = 8.07×10^{-21}, post-hoc pairwise chi-square tests were performed between treatment groups with Bonferroni correction for multiple comparisons. Based on the number of treatment groups there were 6 pairs between all of them, 6-pairwise test was conducted where $\alpha = 0.05/6 = 0.0083$. Therefore, for post-hoc pairwise chi-square tests $p < 0.0083$ is significant, but $p \geq 0.0083$ is not significant. Table 12 summarises the results obtained from the post-hoc pairwise chi-square tests. All comparisons between untreated cells and LPS-treated cells were statistically significant, indicating that exposure to LPS, even at 100 ng/mL, the lowest concentration tested, is sufficient for changes in morphology of A7 cell. In contrast, no statistically significant differences were observed between the LPS-treated groups themselves, indicating that increasing LPS to 300 ng/mL does not change A7 cell circularity, suggesting that these cells become activated at relatively low LPS concentrations within 24 h.

Table 12: Summary of Post-hoc Pairwise Chi-square Tests

Comparison	X^2 test p-value	Significant (α= 0.0083)
0 vs 100	2.83×10^{-18}	Yes
0 vs 200	1.24×10^{-13}	Yes
0 vs 300	1.72×10^{-10}	Yes
100 vs 200	0.139	No
100 vs 300	0.015	No
200 vs 300	0.348	No

Circularity on its own cannot be used as a definitive measure of astrocyte reactivity state. Although changes in cell circularity suggest cytoskeletal remodeling, they do not evaluate functional or molecular aspects of cell reactivity. Therefore, while the observed decrease in

circularity supports cell activation, this data should be interpreted in combination with additional activation markers such as GFAP upregulation.

In addition to cell circularity, the size of LPS-treated and untreated A7 cells was assessed using flow cytometry (Figure 16). Cell size was measured as forward scatter (FSC), with higher FSC values corresponding to larger cells. This analysis showed that LPS-treated cells had slightly higher FSC than untreated controls, indicating mild hypertrophy and cytoplasmic expansion consistent with astrocyte activation [103]. Narrow peaks suggest uniform population without major debris or doublets. This FSC shift was dose-dependent and aligns with other observed morphological changes, suggesting that LPS induces early activation in A7 cells.

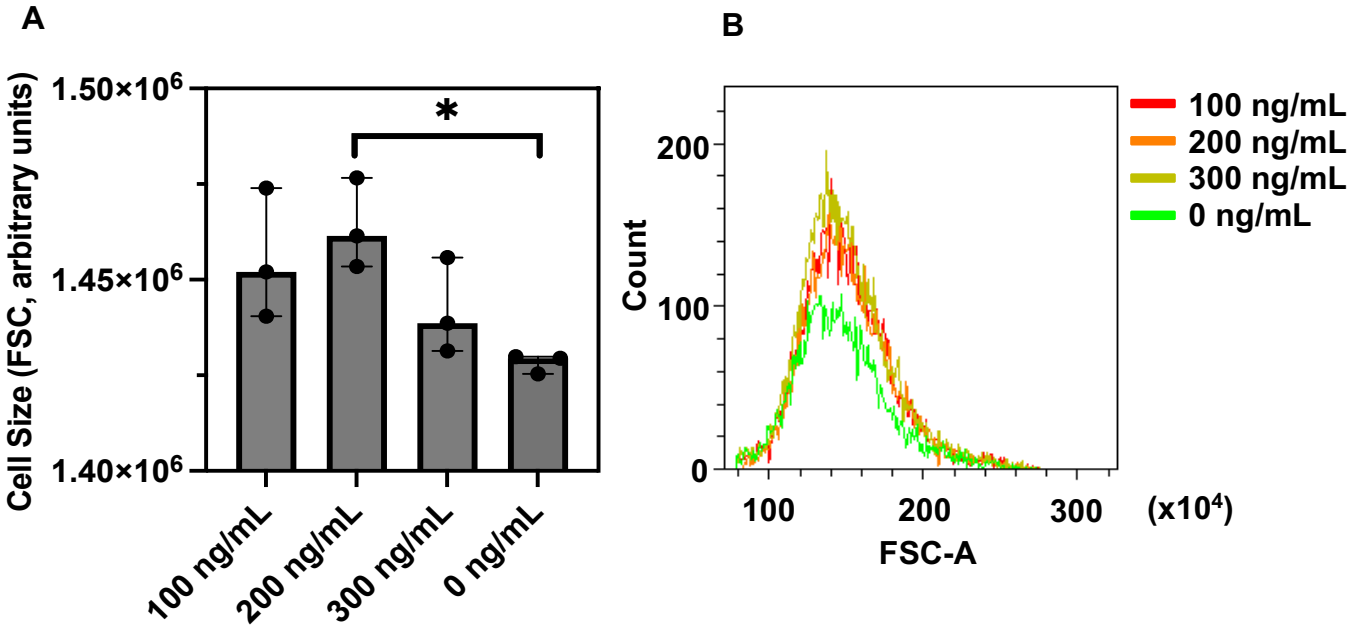


Figure 16: Effect of LPS Treatment on A7 Cell Size

FSC measurement was used to compare cell sizes. Each bar represents the median FSC of A7 cells treated with 100, 200, or 300 ng/mL LPS, or untreated, with individual data points overlaid ($n = 3$). A star above the 200 ng/mL and NC bars indicates a significant difference (Dunn's test with Bonferroni correction, $p = 0.039$) (A). FSC histogram generated in CytExpert shows the change in distribution of cells versus FSC for each LPS treatment (B).

FSC measurements were analyzed using a non-parametric Kruskal-Wallis test due to small sample sizes. A significant overall difference among groups was observed. Dunn's post-hoc test with Bonferroni correction identified a significant difference between the 200 ng/mL LPS treatment and the negative control, while no other comparisons were significant.

4.2.4 Assessing Activation of A7 Cells via Western Blot

GFAP expression was evaluated as a biochemical marker of activation in A7 cells following 24 h of LPS treatment. Protein levels were quantified by western blot and normalized to β-actin as an internal loading control, and then expressed relative to untreated control cells, which were set to a relative expression value of 1. *GFAP* expression was expected to increase in activated A7 cells compared to resting, since its upregulation is the main marker of astrocyte reactivity. Activation is commonly associated with cytoskeletal remodeling and growth of intermediate filaments, which are typically accompanied by increased *GFAP* expression in response to inflammatory stimuli such as LPS [121]. As shown in Figure 17-A, A7 cells treated with 200 ng/mL or 300 ng/mL LPS showed *GFAP* expression levels comparable to untreated cells, with only minor fluctuations observed (means of approximately 1.01 and 0.92 relative to control). These differences are minimal, indicating no significant upregulation of GFAP in response to LPS under the conditions tested. The representative western blot image for GFAP (Figure 17-B) supports this by showing bands of similar intensity across untreated and LPS-treated samples, migrating just above the 55 kDa marker. In addition, the uniform intensity of the β-actin bands across all lanes (Figure 17-C) suggests equal total protein loading. No clear increase in GFAP band intensity is seen with increasing LPS concentration, further suggesting that LPS exposure for 24 h does not significantly alter GFAP levels in A7 cells.

The estimated molecular weight of GFAP is ~ 50 kDa [105]; however, the bands observed in this experiment migrated slightly above the 55 kDa mark. This shift could be due to certain cellular modifications of GFAP. Previously observed morphological changes, the decreased circularity and early stellation of the A7 cells require significant reorganization of the cytoskeleton. This structural remodeling is regulated by post-translational modifications, mainly phosphorylation of intermediate filaments like GFAP [123,124]. Denaturation of the sample protein unfolds its 3D structure but does not break the covalent bonds [125]; therefore, highly phosphorylated GFAP retains this extra volume and altered charge. This could result in GFAP migrating more slowly through the polyacrylamide gel than an unmodified 50 kDa protein.

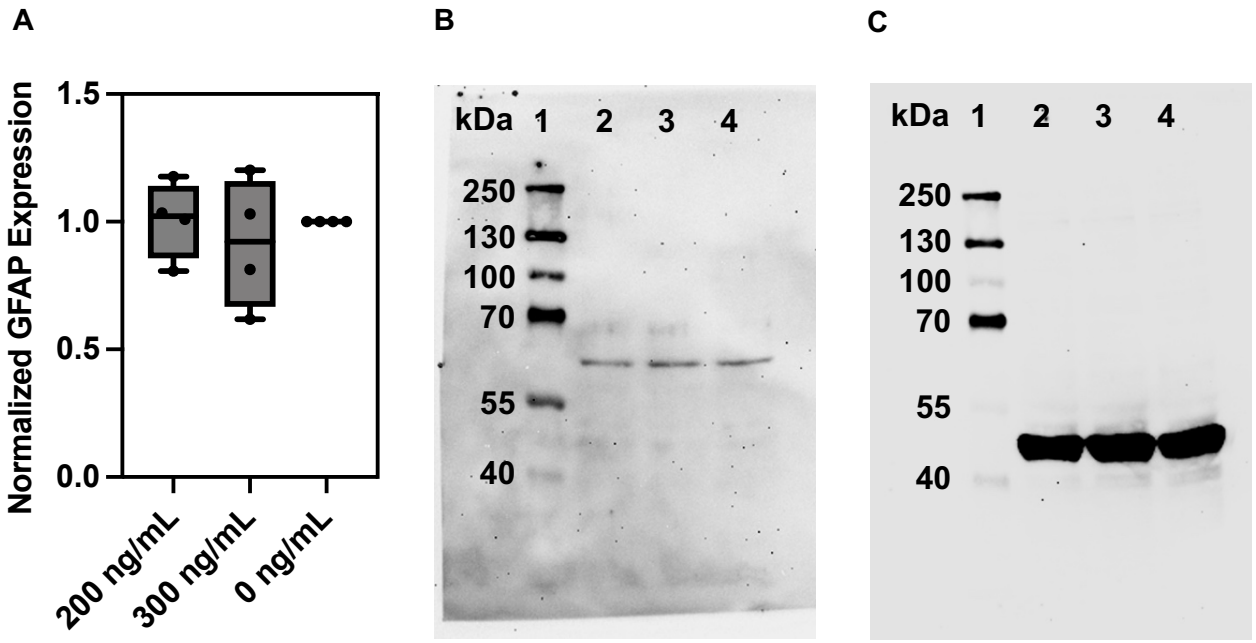


Figure 17: Levels of GFAP Protein in A7 Cells Following LPS Treatment

GFAP expression in A7 cells was assessed by western blotting and quantified relative to untreated control cells, which were normalized to 1. Cells were treated with 200 ng/mL or 300 ng/mL LPS, showing minimal changes in *GFAP* expression compared to untreated cells ($n = 4$) (A). Raw representative image of a western blot where samples were stained with anti-GFAP rabbit primary Ab and anti-rabbit HRP-conjugated secondary Ab 24 h after LPS treatment. The membrane was imaged in the presence of HRP substrate using the iBright Chemi blot imaging system. Lane 1: Spectra BR protein ladder, lane 2: A7 protein after treatment with 200 ng/mL LPS, lane 3: A7 protein after treatment with 300 ng/mL LPS, lane 4: A7 protein untreated (B). Raw representative image of a western blot where samples were stained with anti-β-actin mouse primary Ab and anti-mouse HRP-conjugated secondary Ab. The membrane was imaged in the presence of HRP substrate using the iBright Chemi blot imaging system. Lane 1: Spectra BR protein

ladder, lane 2: A7 protein after treatment with 200 ng/mL LPS, lane 3: A7 protein after treatment with 300 ng/mL LPS, lane 4: A7 protein untreated (C).

These results indicate that, despite the morphological changes observed after LPS treatments, *GFAP* expression remained unchanged. This suggests that LPS treatment of A7 cells does not result in an increase in GFAP under these experimental conditions. Overall, the decrease in cell circularity in the absence of increased GFAP suggests that the cells have entered an early stage of astrocyte activation, where morphological remodeling occurs without detectable GFAP upregulation. Astrocyte reactivity is highly heterogeneous and context dependent, and changes in cell shape can occur independently of classical activation markers such as GFAP [126]. Decreased circularity reflects stellation, characterised by the extension of small, branched processes. This morphology represents a priming phase in which astrocytes extend their processes to monitor the local environment, such as sensing signals from microglia, before initiating full activation [127]. In pure astrocyte cultures, the absence of microglial cytokines can lead to these subtle morphological shifts rather than complete activation [128].

4.2.5 Assessing Transfection Efficiency in Reactive A7 Cells with Miniphagemids

The data on Figure 18-A suggests that expression efficiency of DNA delivered by miniphagemids measured through *dTomato* expression, differs between reactive and resting A7 cells and depends on the displayed targeting ligand. The plasmid control produced comparable *dTomato* expression in resting and reactive A7 cells, indicating that the activity of the GFAP and EF-1α promoters is similar in both cases. This suggests that differences between miniphagemid types are likely due to variations in cellular uptake rather than gene expression.

Flex-EGF miniphagemids resulted in low *dTomato* expression in resting A7 cells, which decreased even more in reactive A7 cells. This suggests that EGF-mediated targeting does not

preferentially enhance delivery to reactive astrocytes and may even be less effective. In contrast, Flex-IRL1620 miniphagemids showed low transfection efficiency in resting A7 cells with an increase in reactive A7 cells. Although expression levels are still low, this relative increase supports the hypothesis that IRL1620-displaying miniphagemids preferentially target reactive astrocytes. IRL1620 is an ETBR agonist, and *ETBR* expression has been reported to increase in activated astrocytes [74]. Transfection efficiency in all miniphagemid samples was much lower than the plasmid control, suggesting that phage display may improve specificity for cell targeting but not delivery efficiency.

This limitation is supported by the comparative control experiment shown in Figure 18-B, where A375 melanoma cell line known to highly express both EGFR [129] and ETBR [130], were treated with the same miniphagemids to evaluate their targeting ability independent of astrocyte activation. While the Flex Switch plasmid control showed high expression rate (~68% dTomato-positive cells), both Flex-EGF and Flex-IRL1620 miniphagemids did not result in noticeable expression. Since the EGFR and ETBR are abundantly present on A375 cells, this lack of signal suggests a strong delivery barrier. Given that A375 cells are generally more susceptible to foreign DNA uptake and expression, the near-zero signal observed suggests a problem with the IRL1620 ligand as a targeting peptide for cellular entry. It is possible that it fails to properly bind the receptor to initiate the uptake, explaining the limited expression seen in the A7 and A375 models.

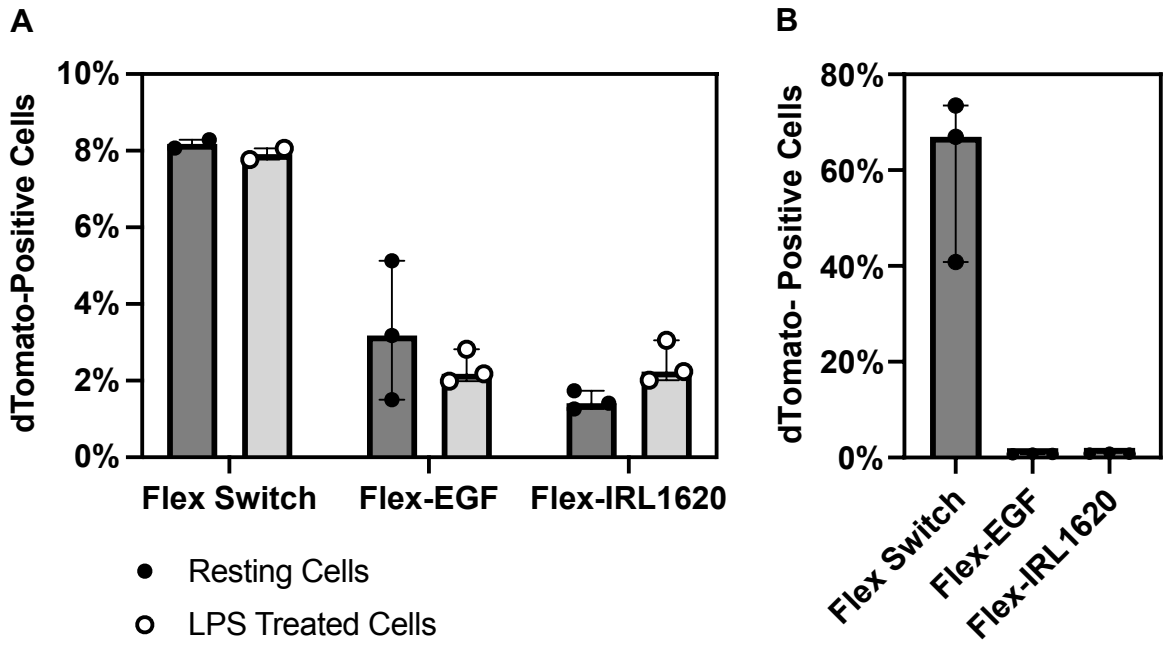


Figure 18: dTomato Signal in Reactive vs Resting A7 Cells and A375 Cells Infected with Miniphagemids

Comparison of Flex-EGF and Flex-IRL1620 miniphagemid affinity to reactive and resting A7 cells (n = 3). Bar plot demonstrates that IRL1620 displaying miniphagemids deliver *dTomato* gene to reactive A7 cells more effectively than EGF displaying miniphagemids (A). Comparison of Flex-EGF and Flex-IRL1620 miniphagemid affinity to A375 cells (n = 3). Bar plot demonstrates that there is no change in deliver efficiency of the *dTomato* gene to A375 cells between EGF and IRL1620 displaying miniphagemids (B). Negative control cells showed ≤1% dTomato-positive cells and are not shown. Data are presented as data points with bars at the median percentage of fluorescent cells.

Effectiveness of the IRL1620 display was also tested using miniphagemids encoding *luc* reporter gene. Luciferase activity in A7 cells treated with miniphagemids was lower than that observed with the pCMV-luc plasmid control, indicating limited gene expression in all samples (Figure 19). The pCMV-luc control produced high luminescence in both resting and LPS-treated cells, signal in reactive cells suggests that they are viable and capable of expression after LPS treatment. However, EGF and IRL1620-displaying miniphagemids showed low and construct-dependent luciferase signal that was close to negative control for most samples. Among the miniphagemids, JL3-EGF showed the highest expression in both resting and LPS-treated cells, while JL1-EGF and JL2-EGF showed low signals with high variability. Miniphagemids displaying IRL1620 showed low expression with negligible differences between resting and reactive cells states. While LPS treatment generally did not increase the luciferase signal across most

miniphagemid samples, JL3-EGF was an exception. For this specific construct, median luminescence nearly doubled from approximately 740 RLU in resting cells to 1,400 RLU in LPS-treated cells. However, examining the individual data points for each condition reveals high variability, suggesting that while JL3-EGF may have some enhanced uptake or expression in reactive A7 cells, it does not overcome the generally limited delivery efficiency. This suggests that while targeted miniphagemids can deliver reporter genes to A7 cells, overall expression remains limited, indicating that the IRL1620 peptide may not effectively bind to LPS-treated A7 cells in this specific conformation.

Similarly to the instance with Flex miniphagemids, this data was supported by the comparative control experiment using A375 cells shown in Figure 19-B, where they were treated with the same miniphagemids to evaluate their targeting ability independent of astrocyte activation. The pJL3 plasmid control transfected into A375 cells resulted in a high luminescence signal around 15,000 RLU. While JL3-EGF miniphagemids managed to perform successful EGFR mediated entry and produce a signal around 800 RLU, all of JL-IRL1620 vectors did not raise luminescence above the untransfected control. Since A375 cells possess abundant ETBR targets, this lack of signal strengthens the hypothesis from the dTomato assays that the IRL1620 ligand, in its phage-displayed conformation, does not facilitate effective cellular entry.

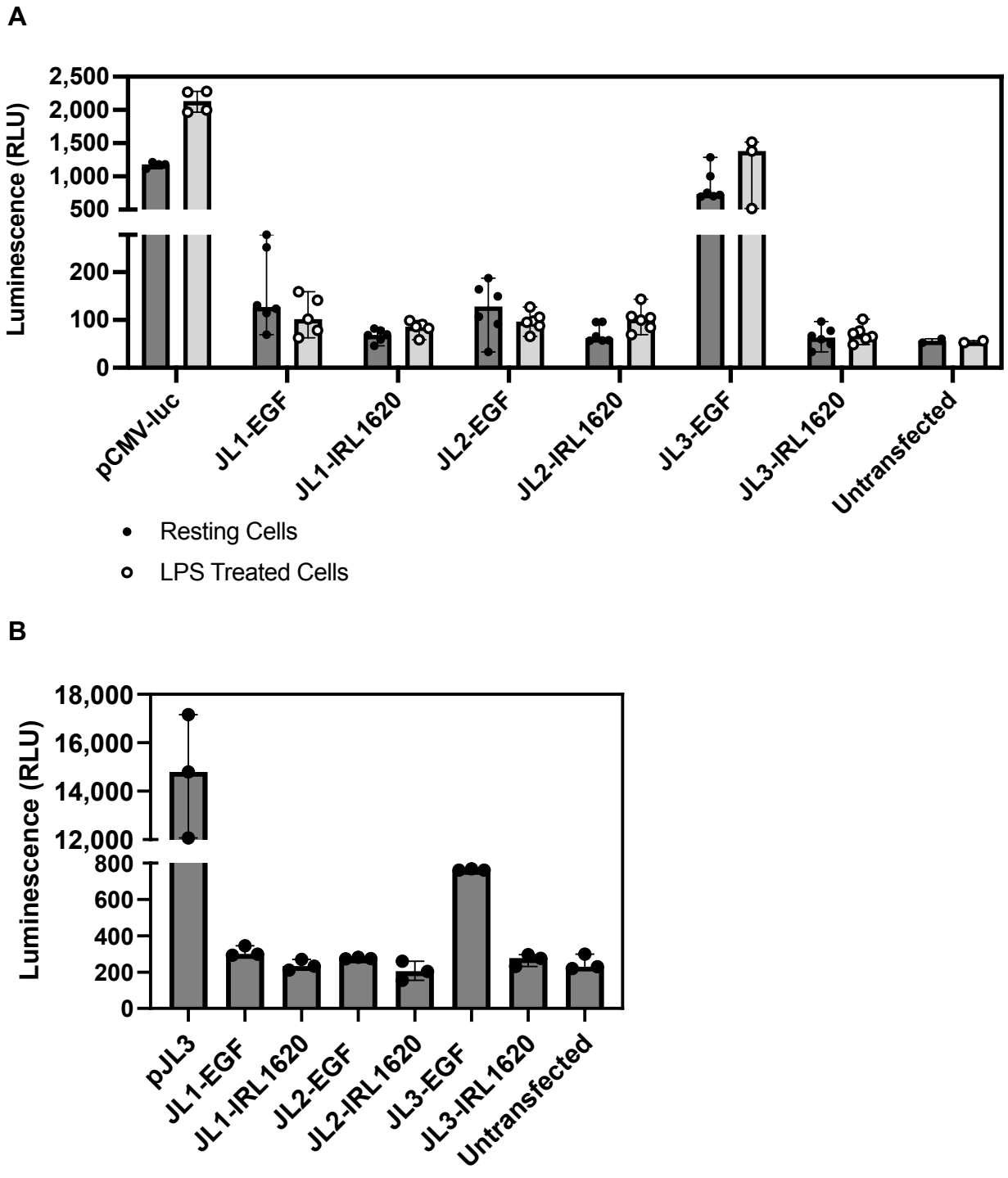


Figure 19: Luciferase Signal in Reactive vs Resting A7 Cells and A375 Cells Infected with Miniphagemids

Luciferase activity in resting and LPS-treated A7 cells after infection with EGF and IRL1620 miniphagemids (n = 2-6). Luminescence is shown as relative luminescence units (RLU) and compared to a pCMV-luc plasmid positive control (A). Luciferase activity in A375 cells after infection with EGF and IRL1620 miniphagemids (n = 3). Luminescence is shown as relative luminescence units (RLU) and compared to a pJL3 plasmid positive control (B). Data are presented as data points with bars at the median luminescence.

After being unable to detect meaningful reporter gene signal in cell cultures treated with IRL1620 displaying miniphagemids, different set of targeting peptides was tested under the same conditions. The data in Figure 20 show that LuNe miniphagemids displaying the SF, SG, and SL ligands result in higher percentages of mNeonGreen-positive cells in LPS-treated A7 cells compared to resting cells. Overall transfection efficiencies for all LuNe miniphagemids were low, with mNeonGreen-positive cells generally below 4% in both resting and reactive states. In contrast, the pLuNe control showed higher expression in resting A7 cells than in reactive. Among the 3 miniphagemids, LuNe-SF showed the highest level of mNeonGreen-positive cells in reactive A7 cells, with low expression in resting cells. This supports the prediction that SF ligand may have activation-dependent targeting and that nonspecific uptake in resting astrocytes is limited [94]. LuNe-SG and LuNe-SL showed a slight increase in expression in reactive cells compared to resting. In addition, for pLuNe in resting A7 cells, large standard deviation was observed, suggesting high biological or technical variability and indicating the need for additional replicates.

These results suggest that ligand display on LuNe miniphagemids can influence gene delivery to reactive astrocytes, with SF showing the most pronounced effect among the peptides tested. However, the small increases in reporter expression and low expression overall indicate that further optimization is needed before this system can be used effectively for therapeutic gene delivery.

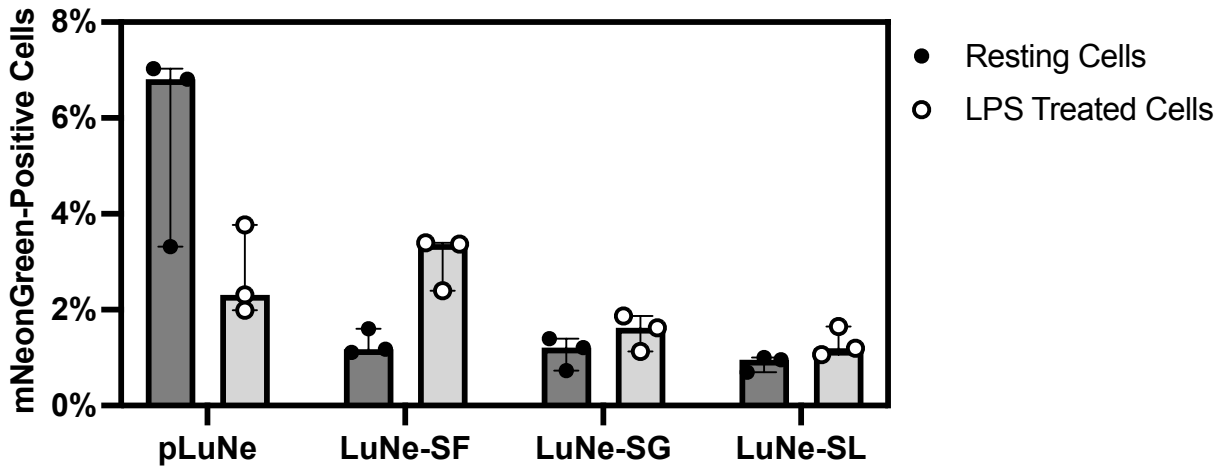


Figure 20: A7 Cells Treated with LuNe Miniphagemids

Comparison of LuNe-SF, LuNe-SG, and LuNe-SL miniphagemid affinity to reactive and resting A7 cells (n = 3). Bar plot demonstrates that SF displaying miniphagemids deliver *mNeonGreen* gene to reactive A7 cells more effectively than other miniphagemids. Negative control cells showed ≤1% mNeonGreen-positive cells and are not shown. Data are presented as data points with bars at the median percentage of fluorescent cells.

4.2.5.1 Limitations Related to Intracellular Trafficking of Miniphagemids

One of the main limitations of the miniphagemid gene delivery system is related to the incomplete understanding of intracellular vector trafficking after the uptake. Miniphagemids lack natural tropism for mammalian cells and rely on peptide display for entry, such as EGF, which can bind EGFR on cell surface triggering clathrin-mediated endocytosis [131]. Following internalization, miniphagemids are isolated inside an early endosome and then late endosome and lysosome. Previous experimental observations in HeLa cells have shown that phages localize near nuclear regions consistent with lysosomal accumulation within hours of uptake. Although a large portion of cells may internalize miniphagemids, only a small percentage expresses the delivered genes, making endosomal entrapment a big limitation in phage-mediated gene delivery [131,132]. The acidic environment of late endosomes and lysosomes could contribute to miniphagemid uncoating since low pH may dissociate capsid proteins from the genome [133]. However, this this is insufficient for genetic cargo to escape from the endosome into the cytoplasm.

In the previous study by Dr. Shirley Wong, TurboFect transfection reagent was used to enhance gene delivery. Within the acidic environment, amine-rich cationic polymers become protonated, leading to osmotic swelling and rupture of the endosomal membrane through the proton sponge effect [134]. Previous findings showed improved gene transfer when phages were combined with TurboFect, supporting the hypothesis that the combination disrupts endosomes facilitating miniphagemid escape from endosomes [72].

Translating such strategies to the human brain raises safety concerns, including cytotoxicity and inflammation, and may reduce the advantages of phage vectors if external chemicals are always required. Future research should focus on developing miniphagemids with intrinsic endosomal escape system, such as capsid modification with pH-sensitive peptides or positive ions, to enable cytosolic delivery without chemical assistance.

One promising strategy to assist miniphagemids with endosomal escape is cationic wrapping [135]. This approach involves coating phages with positively charged polymers, which can help them escape from endosomes through a phenomenon known as the proton sponge effect. Highly cationic polymers create osmotic swelling within endosomal compartments, ultimately leading to rupture [135]. In addition, their positive charge promotes attraction to the negatively charged lipid membranes of cells and endosomes, enhancing uptake and escape, similar to the effect achieved with TurboFect. However, there is no evidence of TurboFect being used for in vivo gene delivery within CNS, and since it is artificial and has strong positive charge, it may be disruptive to neuronal cells making it too toxic for CNS applications [136].

A safer alternative is chitosan, a biodegradable, non-immunogenic cationic polymer [137] that can be optimized to coat miniphagemids through interaction with capsid proteins [138]. Once inside an endosome, chitosan's positive charges attract and trap protons (H^+ ions) as the endosome naturally becomes acidic. This leads to an increase in ions and water inside the endosome, causing

it to swell. Eventually, the swelling creates enough pressure to rupture the endosome [137,139], releasing the miniphagemids into the cytoplasm. In addition, the positive charge of chitosan could help it stick to the negatively charged endosomal membrane [139], further aiding escape. Chitosan has already been used in gene delivery systems to cross the blood–brain barrier in vitro and in vivo [138], and its use for miniphagemids can be optimized by adjusting the chitosan-to-phage ratio to generate stable and functional complexes.

Another approach to enhance miniphagemid endosomal escape is capsid modification. In this strategy, the phage coat is engineered to include endosomal escape peptides such as H5WYG. By incorporating these peptides into the pVIII major coat protein, it is possible to display hundreds of copies on the surface of miniphagemid particles, significantly increasing their ability to disrupt endosomal membranes through the proton sponge effect due to the presence of the histidine residues that absorb the incoming protons [140]. This design allows the phage to more efficiently exit endosomes, improving delivery of the transgenes without the need for any external coatings.

4.2.6 Assessing Cell Viability After Miniphagemid Treatment

To evaluate the safety of the produced miniphagemids, A7 cell viability was assessed following the treatment with various miniphagemids through flow cytometry (Figure 21). The gating for unhealthy or dead cells was established using an unstained untreated A7 population to set the PI-positive range. Overall, most miniphagemid treatments resulted in low levels of cell death (<5%), compared to the untreated and TN buffer controls. This suggests that they are generally well-tolerated by A7 cells and do not compromise membrane integrity. However, AI1 and AI2 vectors appear to be noticeable outliers, showing much higher death rate at ~ 20% and 9% PI-positive cells, respectively. This could be due to a construct-specific cell response since, unlike any other miniphagemid, AI series encodes *GFP* to act as an expression marker gene. The elevated

cell death may be linked to the accumulation of the GFP reporter protein. While it is generally considered safe, high expression of *GFP* has been shown to induce oxidative stress through the generation of reactive oxygen species (ROS) during the chromophore maturation process [141,142]. In glial, sensitive cell lines like A7, this could trigger apoptotic pathways [143], potentially explaining why the AI series showed a higher percentage of PI-positive cells.

Alternatively, but less likely, it is possible that AI miniphagemids have higher delivery efficiency, resulting in a higher expression of *NeuroD1* transcription factor gene. This would cause faster initiation of neuronal reprogramming compared to other vectors and may create a significant metabolic or proteotoxic burden on the A7 cells. This activity could potentially trigger apoptosis in a subset of the population that couldn't transition rapidly enough to a neuronal state, suggesting that the observed cell death from AI1 and AI2 could be a byproduct of their higher delivery efficiency.

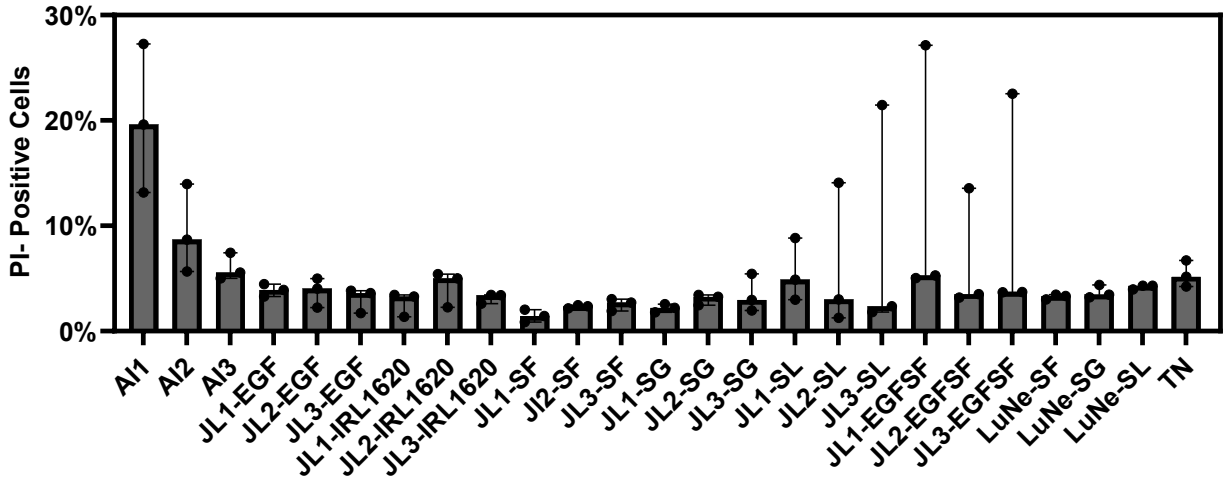


Figure 21: Assessment of A7 Cell Viability Following Miniphagemid Treatments

A7 cells were treated with multiple miniphagemids, transfection reagents, and TN buffer. Cell death was assessed by PI staining and quantified by flow cytometry ($n = 3$). Untreated and TN buffer treated cells served as negative controls, while Lipofectamine (LP) was included as transfection reagent controls. Unstained negative control cells showed ≤1% PI-positive cells and are not shown. Data are presented as data points with bars at the median percentage of fluorescent cells.

4.2.7 Summary of Results for Objective 2: Assess the Gene Delivery Efficiency to Target Cells by Quantifying Reporter Gene Activity.

The findings from this objective show that achieving efficient miniphagemid-mediated gene delivery for astrocyte reprogramming appears to be obstructed by both extracellular targeting barriers and an intracellular environment.

Fluorescent tracking of Cy3-labeled plasmids confirmed that while A7 cells can internalize foreign DNA, reporter gene expression remains low. This suggests that A7 cells possess an aggressive intracellular environment, likely due to active lysosomes and slow division. However, since DNA uptake was assessed using naked plasmids rather than miniphagemids, the ratio of miniphagemid binding efficiency versus expression efficiency remains unquantified.

Despite this, the comparative data from A375 cell line showed the difficulty of the IRL1620 ligand to transfect ETBR-positive A375 cells suggesting an issue with receptor binding or endocytosis when the peptide is displayed on the capsid. In contrast, the LuNe-SF miniphagemid appears to be the most promising candidate as it showed activation-specific targeting of reactive A7 cells, even with low overall expression.

These results suggest that obtaining high *NeuroD1* expression needed for astrocyte reprogramming will require a two-step optimization of the miniphagemid platform. Future work must explore fluorescent labeling of the miniphagemid capsid to decouple receptor binding efficiency from gene expression efficiency. Second, the miniphagemids must be modified to incorporate endosomal escape mechanisms such as cationic wrapping or display of pH-sensitive peptides.

4.3 Objective #3: Evaluate the Ability of *NeuroD1* Constructs to Initiate Astrocyte-to-Neuron Reprogramming.

4.3.1 Assessing Transfection Efficiency in Astrocytes

Expression efficiency was evaluated in human NSC-derived astrocytes (Figure 22-A) following the delivery of 3 plasmid constructs carrying the *NeuroD1* gene (pAI1, pAI2, pAI3). Flow cytometry analysis of *GFP* expression has revealed that all 3 constructs were successfully delivered; however, the efficiency varied across the groups (Figure 22-B). This variation can be due to the promoters used in each construct. The pAI2 construct, which has the universal viral CMV promoter [85], resulted in the lowest *GFP* expression. This is consistent with the fact that the CMV promoter to can be transcriptionally silenced in human stem cell-derived lineages [144,145]. In contrast, pAI1 and pAI3 constructs used the astrocyte-specific GFAP promoter and resulted in higher *GFP* expression with noticeable variability which could be due to differences in the maturation state of the NSC-derived astrocytes at the time of transfection.

Overall expression was relatively low across all conditions (< 10%) suggesting that only a small number of astrocytes was successfully set for reprogramming. While these results show successful construct delivery, this low baseline made the detection of downstream neuronal markers more difficult. Therefore, while plasmid delivery into astrocytes is achievable, expression is inefficient and needs optimization to proceed with this reprogramming approach.

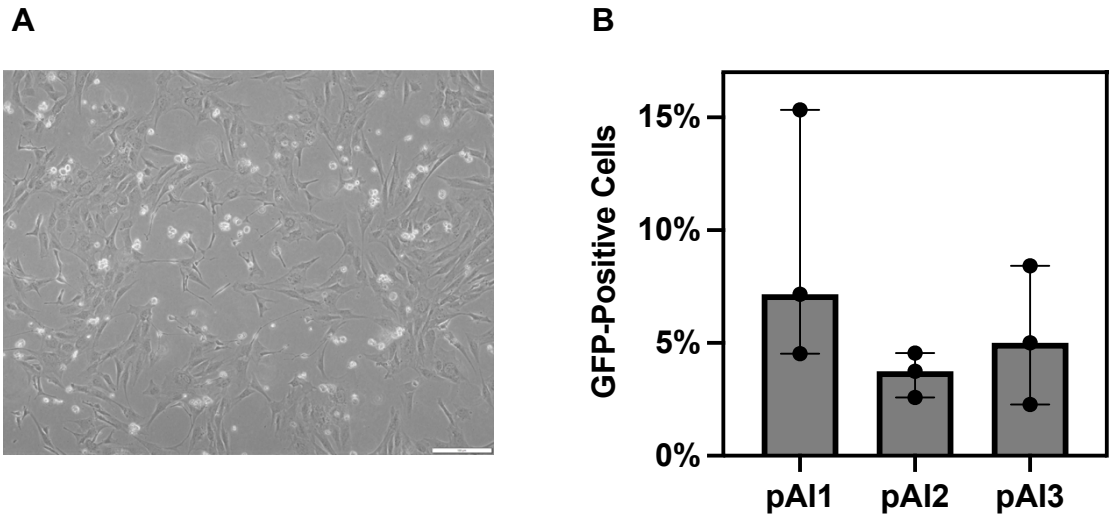


Figure 22: *GFP* Expression in NSC Derived Astrocytes

NSC derived astrocyte cells in cell culture at 100X magnification (A). Flow cytometry analysis of NSC-derived astrocytes showing the percentage of cells expressing GFP for each construct (n = 3). pAI1 showed the highest transfection efficiencies, while pAI2 and pAI3 showed lower yields. Negative control cells showed ≤1% GFP-positive cells and are not shown. Data are presented as data points with bars at the median percentage of fluorescent cells and error bars representing the full data range (B).

4.3.2 Detection of PSA-NCAM Proteins of Reprogrammed Astrocytes

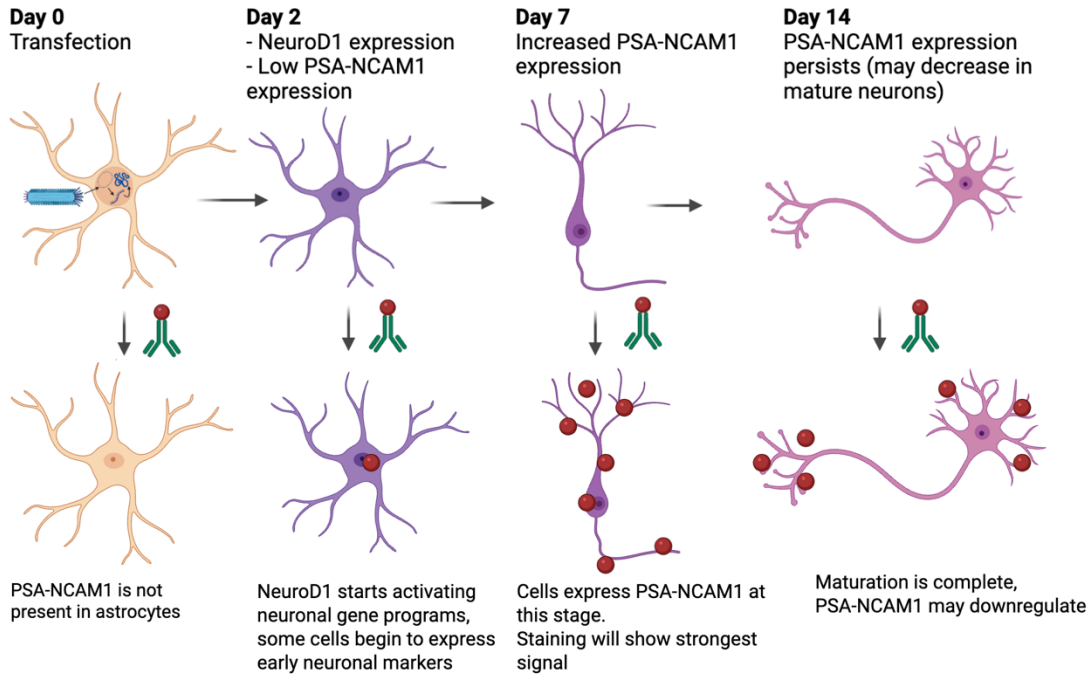


Figure 23: PSA-NCAM Receptors on Astrocytes and Neurons

Schematic representation of PSA-NCAM receptor appearance on cells as they are being converted from astrocytes into neurons (Made with BioRender).

To evaluate early reprogramming-associated changes, a flow cytometry assay was designed to quantify the binding of PSA-NCAM antibody, an early marker associated with neuronal differentiation (Figure 23). First, PSA-NCAM antibody was used to stain immature neurons at day 0, day 2, day 14 to validate the system as a positive control (Figure 24-A). Neurons used in these experiments were provided by James Livingstone, Beazely Lab (Figure 24-B). However, staining remained near baseline levels (< 2%) in these neuronal controls, suggesting that the flow cytometry-based PSA-NCAM antibody assay was not reliable in this case. The lack of signal may be due to the enzymatic cell dissociation using Trypsin-EDTA required for flow cytometry, which could cleave cell surface markers like PSA-NCAM. Therefore, the data from this approach cannot be considered reliable for evaluating astrocyte reprogramming.

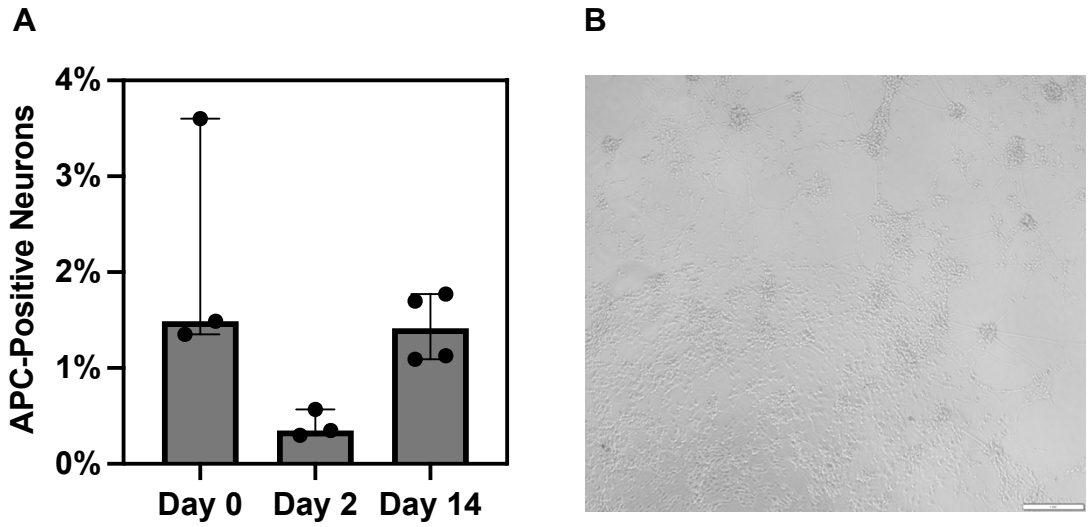


Figure 24: PSA-NCAM Ab Binding in Immature Neurons

Figure contains a bar plot comparing PSA-NCAM Ab binding in immature neurons (n = 3). Negative control cells showed ≤1% APC-positive neurons and are not shown. Data are presented as data points with bars at the median percentage of fluorescent cells (A). Immature neurons on day 14 at 40X magnification (B).

Despite the limitations of this assay, following the transfection with *NeuroD1* carrying constructs: pAI and pJL, the expression of *NCAM1*, an early marker associated with neuronal differentiation, was assessed in NSC-derived astrocytes at days 7 and 14 (Figure 25). Astrocyte cultures used in these experiments were provided by Kartar Singh, Beazely Lab. Binding of PSA-NCAM antibody was quantified using flow cytometry to evaluate early reprogramming-associated changes in cells. While PSA-NCAM bound cells were detected at both time points, with higher signal at day 14, suggesting that this neuronal marker appears over time. Cells treated with pJL constructs showed lower PSA-NCAM binding than those treated with pAI, suggesting that there are differences in expression efficiency of *NeuroD1* that might influence *NCAM1* expression in astrocytes. The overall percentage of PSA-NCAM bound cells was low across all conditions, consistent with the low transfection efficiencies observed in NSC-derived astrocytes (Figure 25). To more accurately assess neuronal differentiation, later analyses should attempt immunocytochemistry (ICC) with an internal TUJ1 antibody to confirm marker expression in reprogrammed cells.

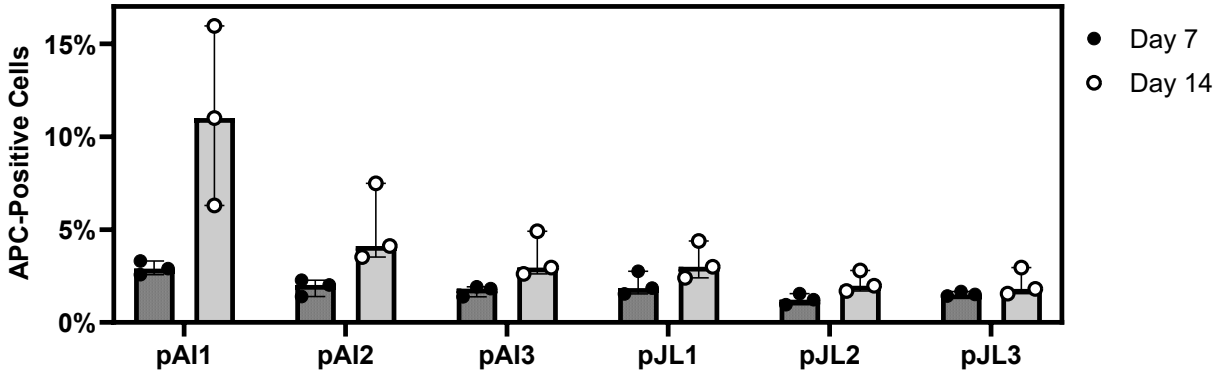


Figure 25: PSA-NCAM Ab Signal in NSC-Derived Astrocytes at Day 7 and 14 Post-Transfection

Figure contains a bar plot comparing PSA-NCAM Ab binding in NSC derived astrocyte cells transfected with pAI and pJL plasmids at days 7 and 14 post-transfection (n = 3). Negative control cells showed ≤1% APC-positive cells and are not shown. Data are presented as data points with bars at the median percentage of fluorescent cells.

4.3.3 Summary of Results for Objective 3: Evaluate the Ability of *NeuroD1* Constructs to Initiate Astrocyte-to-Neuron Reprogramming.

These results demonstrate that while miniphagemid vectors can successfully deliver *NeuroD1* into human NSC-derived astrocytes, some important barriers are still present before efficient reprogramming can be achieved. Transfection efficiency of astrocytes with precursor plasmids was generally low (<10%) across all samples, with expression levels influenced by the present promoter. Additionally, the inability to detect PSA-NCAM binding in positive control neurons suggests that flow cytometry is not a reliable method for assessing early reprogramming in this experiment, probably due to the enzymatic cleavage of surface markers during cell detachment. Therefore, future work should focus on optimizing transfection conditions to improve delivery rates and investigating ICC as an alternative for detecting neuronal differentiation markers in treated astrocyte cells.

5. Future Directions

5.1 Future Miniphagemid Purification and Characterization Steps

In addition to employing quantification techniques such as MADLS and UV-Vis, the concentration of miniphagemid samples can be quantified using SYBR Green quantitative polymerase chain reaction (qPCR), it is a method that measures DNA quantity through fluorescence. In this technique, SYBR Green dye binds dsDNA and fluoresces when excited by light, and the intensity of the fluorescence is proportional to the amount of DNA present [146]. By amplifying a specific region of the miniphagemid DNA using primers designed for its sequence, the fluorescence signal is measured at each cycle of amplification. In this case the sequences for the markers such as GFP tag can be amplified since those are standard target sequences that are present in multiple plasmids. A standard curve generated from known concentrations of miniphagemid DNA will allow to quantify the DNA concentration in the sample based on the fluorescence data [146].

In addition to DNase treatment, miniphagemids can be further purified via size exclusion chromatography (SEC) which separates molecules based on their size. A sample containing miniphagemids is run through a column packed with porous beads. Smaller molecules enter the pores and take longer to pass through the column, while larger molecules, such as miniphagemids, are excluded from the pores and elute faster [147]. The eluting samples is collected in fractions since difference in elution times allows for the separation of miniphagemids from smaller contaminants, such as free nucleotides or smaller plasmids, producing purified miniphagemids [148].

5.2 Assessing Endotoxin Levels in Miniphagemids

It is important to assess endotoxin levels in miniphagemid samples because endotoxins, primarily lipopolysaccharides (LPS) from bacterial cell walls, can negatively impact mammalian cell cultures by triggering inflammatory responses, altering gene expression, and reducing cell viability [149]. These effects can reduce transfection efficiency and interfere with experimental results by introducing unintended responses, such as stress or immune-like activation in sensitive cell types like astrocytes. In addition, because miniphagemids are being developed for therapeutic use, monitoring and minimizing endotoxin contamination is important to ensure reliable results and to meet safety standards for future translational applications.

Endotoxicity of the produced miniphagemid samples was assessed using the ToxinSensor™ Chromogenic LAL Endotoxin Assay Kit (Catalog # L00350C, GenScript, Piscataway, USA); however, the assay controls did not perform as expected, limiting interpretation of the results. Serial dilution of *E. coli* endotoxin standard was prepared (0.1 - 1 EU/mL) for generating a standard curve. Then 100 µL of these standards and miniphagemid samples dispensed into endotoxin-free vials to which 100 µL of Limulus Amebocyte Lysate (LAL) reagent was added and incubated at 37 °C for 10 min. Following the incubation, chromogenic substrate was added and incubated for 6 min, then the stop solutions were added. Next, samples were transferred to the white clear bottom 96 well plate (Catalog # 165306, Thermo Fisher Scientific, Waltham, USA) and their absorbance was measured at 545 nm via the Varioskan LUX Multimode Microplate Reader (Thermo Fisher Scientific, Waltham, USA), analysis of the absorbance was carried out using the SkanIt v7.1 software (Thermo Fisher Scientific, Waltham, USA). The endotoxin concentration in the samples was calculated by plotting absorbance against the standard curve (1 EU = 0.2 ng of LPS). The results, shown in Figure 26, indicate that all samples including the TN buffer negative control contained LPS levels at the concentration of around 1 EU/mL which is the

detection limit of this assay kit. However, it is possible that sample buffer is emitting a background signal close to the detection limit. This suggests a potential issue with the assay or contamination in the experimental setup since TN buffer should ideally show no endotoxin detection, as it is free from endotoxins. Values were calculated from a standard curve generated using serial dilutions of *E. coli* endotoxin.

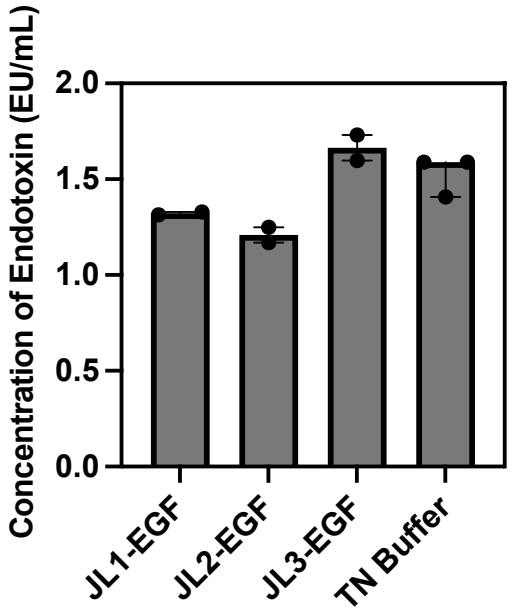


Figure 26: Quantification of Endotoxin in Miniphagemid Samples Using Chromogenic Assay

Quantification of endotoxin levels in miniphagemid samples using a chromogenic LAL assay (n = 2-3). Endotoxin concentrations (EU/mL) were measured for JL1-EGF, JL2-EGF, and JL3-EGF miniphagemid preparations, with TN buffer included as a negative control. Data are presented as data points with bars at the median.

Future work should focus on improving endotoxin testing and resolving the issues observed with the current assay. Endotoxin measurements should be repeated using strict endotoxin-free techniques and verified controls, and potential interference from TN buffer or miniphagemid components should be evaluated by testing known endotoxin standards in these solutions. Using an endotoxin detection kit with a higher detection range or sensitivity would help better distinguish low endotoxin levels from background signal. In addition, endotoxin removal steps should be optimized during miniphagemid purification and followed by repeat testing.

5.3 Optimizing Miniphagemids for Enhanced BBB Penetration

Although filamentous M13 bacteriophages have been shown to be able to cross the BBB some studies have suggested that the efficiency with which they travel across the barrier could be enhanced. Improving this process could significantly increase transgene delivery to the brain and enhance the effectiveness of gene therapy in CNS. One promising approach is ligand-mediated transcytosis. For example, M13 phages that have been modified to carry chlorotoxin on their pIII capsid protein have been shown to actively cross the BBB in vivo, leading to a significant increase in accumulation in the brain of healthy mice compared to non-targeted phages, which are rapidly cleared and show lower brain uptake [150]. Therefore, future work could explore additional ligands that target natural BBB transport receptors to further improve endothelial uptake and transcytosis. In addition, optimizing capsid surface properties, such as charge may enhance circulation time, cellular uptake, and brain specificity.

5.4 Further Assessing Astrocytes Reprogramming into Neurons

It is also possible to perform functional assays on the reprogrammed neurons to assess their electrophysiological activity, synaptic connectivity, and neurotransmitter release. This will allow to verify that reprogrammed neurons are not only expressing neuronal markers but are also presenting neuronal activity, essential for integration into neural networks and performing neuronal functions. Multi-Electrode Arrays (MEAs) can be used to assess electrical properties of neurons. MEAs consist of a grid of microelectrodes embedded in a culture dish that detect electrical signals generated by neurons. When neurons are cultured on the array, the electrodes capture extracellular voltage changes, which correspond to action potentials and network activity. This data is recorded and analyzed to assess neuronal firing patterns, connectivity, and overall network dynamics [151]. Synaptic activity can be measured via calcium imaging that detects neuronal activity by measuring

calcium influx during action potential firing. Neurons can be treated with calcium-sensitive fluorescent dyes that change fluorescence intensity in response to calcium influx. These changes are visualized using fluorescence microscopy, providing information of neuronal firing and network activity in real time [152]. Neurotransmitter release can also be measured via optical imaging using Fei Mao (FM) dyes such as FM1-43. FM dye can label synaptic vesicles in neurons and when a neuron is stimulated, the vesicles fuse with the plasma membrane to release neurotransmitters, and the FM dye integrates into the membrane. After vesicle endocytosis, the dye is retained within the vesicles, and changes in fluorescence intensity can be measured. This will provide a real-time visualization of neurotransmitter release using fluorescence microscopy [153].

Successful reprogramming of astrocytes into neurons requires more than the introduction of transcription factors. Epigenetic modifiers, such as chromatin remodeling agents or DNA methylation inhibitors, can be used to enhance the accessibility of neuronal genes and improve reprogramming efficiency [154,155]. In addition, presence of the growth factors like brain-derived neurotrophic factor (BDNF) and neurotrophin-3 (NT-3) in the media is necessary for neuronal survival, differentiation, and maturation [155,156]. Moreover, suppression of astrocyte-specific pathways, such as STAT3 signaling, can further enhance neuronal conversion [155]. A robust and efficient delivery system, such as the miniphagemid vectors developed in this project, may prove useful in facilitating precise, high-efficiency expression of the transcription factors.

6. Summary and Significance

This research project focuses on developing a novel gene therapy approach for treating neurodegenerative diseases by reprogramming astrocytes into neurons using the Intelligent Phagemid-Assembled Gene Expression (iPhAGE) technology. Neurodegenerative diseases are marked by the progressive loss of neurons, and existing treatments are very limited, requiring novel solutions. Reprogramming astrocytes into neurons offers a promising strategy to repair damaged neural circuits and restore cognitive and motor functions. The iPhAGE system, based on M13 bacteriophage-derived miniphagemids, offers several advantages over existing gene delivery methods, including large cargo capacity, low immunogenicity, and the potential to cross blood-brain barrier [63,72]. These features make iPhAGE a platform capable of overcoming key limitations of current gene delivery systems.

In this study, plasmids encoding the *NeuroD1* reprogramming factor under both astrocyte-specific and universal promoters were constructed, and miniphagemids were produced and characterised. Transfection efficiency was evaluated in resting and reactive A7 cells, and early neuronal reprogramming was assessed using *NCAM1* expression. While full functional reprogramming was not achieved at this stage, the project established a framework for iPhAGE-based gene delivery and identified main challenges for future optimization. By enabling the controlled delivery of reprogramming factors, iPhAGE could facilitate the development of regenerative therapies that restore neuronal populations in damaged brain tissue.

References

1. Ludwig, P. E., Reddy, V. & Varacallo, M. A. Neuroanatomy, Neurons. in *StatPearls* (2025).
2. Gradisnik, L. & Velnar, T. Astrocytes in the central nervous system and their functions in health and disease: A review. *World J. Clin. Cases* 11, 3385–3394 (2023).
3. Steinmetz, J. D. *et al.* Global, regional, and national burden of disorders affecting the nervous system, 1990–2021: a systematic analysis for the Global Burden of Disease Study 2021. *Lancet Neurol.* 23, 344–381 (2024).
4. Jellinger, K. A. Basic mechanisms of neurodegeneration: a critical update. *J. Cell. Mol. Med.* 14, 457–487 (2010).
5. S. Wong, R. A. Slavcev. Nucleic Acid Delivery System. Patent. U.S. 63,336844 (2022).
6. Kessaris, N., Pringle, N. & Richardson, W. D. Specification of CNS glia from neural stem cells in the embryonic neuroepithelium. *Philos. Trans. R. Soc. B Biol. Sci.* 363, 71–85 (2008).
7. Yamaguchi, M. *et al.* Neural stem cells and neuro/gliogenesis in the central nervous system: understanding the structural and functional plasticity of the developing, mature, and diseased brain. *J. Physiol. Sci.* 66, 197–206 (2016).
8. Lanjewar, S. N. & Sloan, S. A. Growing Glia: Cultivating Human Stem Cell Models of Gliogenesis in Health and Disease. *Front. Cell Dev. Biol.* 9, 649538 (2021).
9. Sofroniew, M. V. & Vinters, H. V. Astrocytes: biology and pathology. *Acta Neuropathol. (Berl.)* 119, 7–35 (2010).
10. Gradisnik, L. & Velnar, T. Astrocytes in the central nervous system and their functions in health and disease: A review. *World J. Clin. Cases* 11, 3385–3394 (2023).
11. Wei, D. C. & Morrison, E. H. Histology, Astrocytes. in *StatPearls* (StatPearls Publishing, Treasure Island (FL), 2025).

12. Corti, S. *et al.* Direct reprogramming of human astrocytes into neural stem cells and neurons. *Exp. Cell Res.* 318, 1528–1541 (2012).
13. Bortolanza, M. *et al.* Sex-Specific Properties of Astrocytes: From Development to Evolutionary Insights. *Neurochem. Res.* 50, 267 (2025).
14. Santos-Galindo, M., Acaz-Fonseca, E., Bellini, M. J. & Garcia-Segura, L. M. Sex differences in the inflammatory response of primary astrocytes to lipopolysaccharide. *Biol. Sex Differ.* 2, 7 (2011).
15. Gozlan, E., Lewit-Cohen, Y. & Frenkel, D. Sex Differences in Astrocyte Activity. *Cells* 13, 1724 (2024).
16. Brulet, R. *et al.* NeuroD1 Instructs Neuronal Conversion in Non-Reactive Astrocytes. *Stem Cell Rep.* 8, 1506–1515 (2017).
17. Gascón, S. *et al.* Identification and Successful Negotiation of a Metabolic Checkpoint in Direct Neuronal Reprogramming. *Cell Stem Cell* 18, 396–409 (2016).
18. Livingston, J. *et al.* Direct reprogramming of astrocytes to neurons leads to functional recovery after stroke. Preprint at https://doi.org/10.1101/2020.02.02.929091 (2020).
19. Miyata, T., Maeda, T. & Lee, J. E. NeuroD is required for differentiation of the granule cells in the cerebellum and hippocampus. *Genes Dev.* 13, 1647–1652 (1999).
20. Lee, J. E. *et al.* Conversion of Xenopus ectoderm into neurons by NeuroD, a basic helix-loop-helix protein. *Science* 268, 836–844 (1995).
21. Matsuda, T. *et al.* Pioneer Factor NeuroD1 Rearranges Transcriptional and Epigenetic Profiles to Execute Microglia-Neuron Conversion. *Neuron* 101, 472-485.e7 (2019).
22. Pataskar, A. *et al.* NeuroD1 reprograms chromatin and transcription factor landscapes to induce the neuronal program. *EMBO J.* 35, 24–45 (2016).

23. Li, H. & Chen, G. In Vivo Reprogramming for CNS Repair: Regenerating Neurons from Endogenous Glial Cells. *Neuron* 91, 728–738 (2016).

24. Guo, Z. *et al.* In vivo direct reprogramming of reactive glial cells into functional neurons after brain injury and in an Alzheimer's disease model. *Cell Stem Cell* 14, 188–202 (2014).

25. *Neuroscience*. (Sinauer Associates, Sunderland, Mass, 2001).

26. Vasan, L., Park, E., David, L. A., Fleming, T. & Schuurmans, C. Direct Neuronal Reprogramming: Bridging the Gap Between Basic Science and Clinical Application. *Front. Cell Dev. Biol.* 9, 681087 (2021).

27. Ang, C. E. & Wernig, M. Induced neuronal reprogramming. *J. Comp. Neurol.* 522, 2877–2886 (2014).

28. Heins, N. *et al.* Glial cells generate neurons: the role of the transcription factor Pax6. *Nat. Neurosci.* 5, 308–315 (2002).

29. Yang, N., Ng, Y. H., Pang, Z. P., Südhof, T. C. & Wernig, M. Induced Neuronal Cells: How to Make and Define a Neuron. *Cell Stem Cell* 9, 517–525 (2011).

30. Kolb, B. & Gibb, R. Brain plasticity and behaviour in the developing brain. *J. Can. Acad. Child Adolesc. Psychiatry* 20, 265–276 (2011).

31. Clark, I. H. *et al.* Cell Reprogramming for Regeneration and Repair of the Nervous System. *Biomedicines* 10, 2598 (2022).

32. Wan, Y. & Ding, Y. Strategies and mechanisms of neuronal reprogramming. *Brain Res. Bull.* 199, 110661 (2023).

33. Nagappan, P. G., Chen, H. & Wang, D.-Y. Neuroregeneration and plasticity: a review of the physiological mechanisms for achieving functional recovery postinjury. *Mil. Med. Res.* 7, 30 (2020).

34. Yudaeva, A. *et al.* Clinical and Translational Landscape of Viral Gene Therapies. *Cells* 13, 1916 (2024).

35. Scheller, E. L. & Krebsbach, P. H. Gene therapy: design and prospects for craniofacial regeneration. *J. Dent. Res.* 88, 585–596 (2009).

36. Sung, Y. & Kim, S. Recent advances in the development of gene delivery systems. *Biomater. Res.* 23, 8 (2019).

37. Moffit, J. S., Alatsis, K. R., Blanset, D. L., Buss, N. & Rana, P. Nonclinical strategies and considerations to enable the redosing of gene therapies. *Mol. Ther. Methods Clin. Dev.* 33, 101520 (2025).

38. Gray, S. J. Should patients with pre-existing anti-AAV antibodies be excluded from receiving intrathecally delivered AAV vectors? *Mol. Ther. Methods Clin. Dev.* 33, 101631 (2025).

39. Kohn, D. B., Chen, Y. Y. & Spencer, M. J. Successes and challenges in clinical gene therapy. *Gene Ther.* 30, 738–746 (2023).

40. Puhl, D. L., D'Amato, A. R. & Gilbert, R. J. Challenges of gene delivery to the central nervous system and the growing use of biomaterial vectors. *Brain Res. Bull.* 150, 216–230 (2019).

41. Bulcha, J. T., Wang, Y., Ma, H., Tai, P. W. L. & Gao, G. Viral vector platforms within the gene therapy landscape. *Signal Transduct. Target. Ther.* 6, 53 (2021).

42. Lazaris, V. *et al.* Non-Viral Episomal Vector Mediates Efficient Gene Transfer of the β-Globin Gene into K562 and Human Haematopoietic Progenitor Cells. *Genes* 14, 1774 (2023).

43. Petrov, G., Dymova, M. & Richter, V. Bacteriophage-Mediated Cancer Gene Therapy. *Int. J. Mol. Sci.* 23, 14245 (2022).

44. Ginn, S. L., Mandwie, M., Alexander, I. E., Edelstein, M. & Abedi, M. R. Gene therapy clinical trials worldwide to 2023—an update. *J. Gene Med.* 26, e3721 (2024).

45. Mulia, G. E., Picanço-Castro, V., Stavrou, E. F., Athanassiadou, A. & Figueiredo, M. L. Advances in the Development and the Applications of Nonviral, Episomal Vectors for Gene Therapy. *Hum. Gene Ther.* 32, 1076–1095 (2021).

46. Häcker, H. *et al.* Immune Cell Activation by Bacterial Cpg-DNA through Myeloid Differentiation Marker 88 and Tumor Necrosis Factor Receptor–Associated Factor (Traf)6. *J. Exp. Med.* 192, 595–600 (2000).

47. Nafissi, N. *et al.* DNA Ministrings: Highly Safe and Effective Gene Delivery Vectors. *Mol. Ther. - Nucleic Acids* 3, e165 (2014).

48. Kasman, L. M. & Porter, L. D. Bacteriophages. in *StatPearls* (StatPearls Publishing, Treasure Island (FL), 2025).

49. Zhu, J. *et al.* A prokaryotic-eukaryotic hybrid viral vector for delivery of large cargos of genes and proteins into human cells. *Sci. Adv.* 5, eaax0064 (2019).

50. Hay, I. D. & Lithgow, T. Filamentous phages: masters of a microbial sharing economy. *EMBO Rep.* 20, e47427 (2019).

51. Wang, R. *et al.* M13 phage: a versatile building block for a highly specific analysis platform. *Anal. Bioanal. Chem.* 415, 3927–3944 (2023).

52. Smeal, S. W., Schmitt, M. A., Pereira, R. R., Prasad, A. & Fisk, J. D. Simulation of the M13 life cycle I: Assembly of a genetically-structured deterministic chemical kinetic simulation. *Virology* 500, 259–274 (2017).

53. Ghosh, D., Kohli, A. G., Moser, F., Endy, D. & Belcher, A. M. Refactored M13 bacteriophage as a platform for tumor cell imaging and drug delivery. *ACS Synth. Biol.* 1, 576–582 (2012).

54. Tsedev, U. *et al.* Phage Particles of Controlled Length and Genome for In Vivo Targeted Glioblastoma Imaging and Therapeutic Delivery. *ACS Nano* 16, 11676–11691 (2022).

55. Haigh, N. G. & Webster, R. E. The pI and pXI assembly proteins serve separate and essential roles in filamentous phage assembly 1 1Edited by M. Gottesman. *J. Mol. Biol.* 293, 1017–1027 (1999).

56. Kokoska, R. J. & Steege, D. A. Appropriate Expression of Filamentous Phage f1 DNA Replication Genes II and X Requires RNase E-Dependent Processing and Separate mRNAs. *J. Bacteriol.* 180, 3245–3249 (1998).

57. Opalka, N. *et al.* Structure of the Filamentous Phage pIV Multimer by Cryo-electron Microscopy. *J. Mol. Biol.* 325, 461–470 (2003).

58. Lee, B.-Y., Lee, J., Ahn, D. J., Lee, S. & Oh, M.-K. Optimizing protein V untranslated region sequence in M13 phage for increased production of single-stranded DNA for origami. *Nucleic Acids Res.* 49, 6596–6603 (2021).

59. Jia, Q. & Xiang, Y. Cryo-EM structure of a bacteriophage M13 mini variant. *Nat. Commun.* 14, 5421 (2023).

60. Hess, G. T. *et al.* M13 Bacteriophage Display Framework That Allows Sortase-Mediated Modification of Surface-Accessible Phage Proteins. *Bioconjug. Chem.* 23, 1478–1487 (2012).

61. Fermin, G., Rampersad, S. & Tennant, P. Viruses as Tools of Biotechnology. in *Viruses* 291–316 (Elsevier, 2018). doi:10.1016/B978-0-12-811257-1.00012-7.

62. Baird, A. Gene Transfer into Mammalian Cells Using Targeted Filamentous Bacteriophage. *Cold Spring Harb. Protoc.* 2011, pdb.prot5653 (2011).

63. Wong, S., Jimenez, S. & Slavcev, R. A. Construction and characterization of a novel miniaturized filamentous phagemid for targeted mammalian gene transfer. *Microb. Cell Factories* 22, 124 (2023).

64. Chang, C. *et al.* Engineered M13 phage as a novel therapeutic bionanomaterial for clinical applications: From tissue regeneration to cancer therapy. *Mater. Today Bio* 20, 100612 (2023).

65. Marvin, D. Filamentous phage structure, infection and assembly. *Curr. Opin. Struct. Biol.* 8, 150–158 (1998).

66. Wang, Y. *et al.* Filamentous Bacteriophage—A Powerful Carrier for Glioma Therapy. *Front. Immunol.* 12, 729336 (2021).

67. Dotiwala, A. K., McCausland, C. & Samra, N. S. Anatomy, Head and Neck: Blood Brain Barrier. in *StatPearls* (StatPearls Publishing, Treasure Island (FL), 2025).

68. Kassner, P. D., Burg, M. A., Baird, A. & Larocca, D. Genetic Selection of Phage Engineered for Receptor-Mediated Gene Transfer to Mammalian Cells. *Biochem. Biophys. Res. Commun.* 264, 921–928 (1999).

69. Rakonjac, J., Jovanovic, G. & Model, P. Filamentous phage infection-mediated gene expression: construction and propagation of the gIII deletion mutant helper phage R408d3. *Gene* 198, 99–103 (1997).

70. Goverdhana, S. *et al.* Regulatable gene expression systems for gene therapy applications: progress and future challenges. *Mol. Ther.* 12, 189–211 (2005).

71. Gonçalves, G. A. R. & Paiva, R. D. M. A. Gene therapy: advances, challenges and perspectives. *Einstein São Paulo* 15, 369–375 (2017).

72. Shirley Wong. Construction and Characterization of a Hybrid Bacteriophage Gene Delivery Platform. Doctoral dissertation. (University of Waterloo, Waterloo, 2022).

73. Levinson, A., Silver, D. & Seed, B. Minimal size plasmids containing an M13 origin for production of single-strand transducing particles. *J. Mol. Appl. Genet.* 2, 507–517 (1984).

74. LeComte, M. D., Shimada, I. S., Sherwin, C. & Spees, J. L. Notch1–STAT3–ETB_R signaling axis controls reactive astrocyte proliferation after brain injury. *Proc. Natl. Acad. Sci.* 112, 8726–8731 (2015).

75. Takai, M. *et al.* A potent and specific agonist, Suc-[Glu9,Ala11,15]-endothelin-1(8-21), IRL 1620, for the ETB receptor. *Biochem. Biophys. Res. Commun.* 184, 953–959 (1992).

76. Brenner, M., Kisseberth, W., Su, Y., Besnard, F. & Messing, A. GFAP promoter directs astrocyte-specific expression in transgenic mice. *J. Neurosci.* 14, 1030–1037 (1994).

77. Kick, B., Praetorius, F., Dietz, H. & Weuster-Botz, D. Efficient Production of Single-Stranded Phage DNA as Scaffolds for DNA Origami. *Nano Lett.* 15, 4672–4676 (2015).

78. Feng, Z., Li, X., Fan, B., Zhu, C. & Chen, Z. Maximizing the Production of Recombinant Proteins in Plants: From Transcription to Protein Stability. *Int. J. Mol. Sci.* 23, 13516 (2022).

79. Palanisamy, C. P. *et al.* New strategies of neurodegenerative disease treatment with extracellular vesicles (EVs) derived from mesenchymal stem cells (MSCs). *Theranostics* 13, 4138–4165 (2023).

80. Niazi, S. K. Non-Invasive Drug Delivery across the Blood–Brain Barrier: A Prospective Analysis. *Pharmaceutics* 15, 2599 (2023).

81. Cerf, M. E., Muller, C. J. F., Du Toit, D. F., Louw, J. & Wolfe-Coote, S. A. Transcription factors, pancreatic development, and β-cell maintenance. *Biochem. Biophys. Res. Commun.* 326, 699–702 (2005).

82. Puls, B. *et al.* Regeneration of Functional Neurons After Spinal Cord Injury via in situ NeuroD1-Mediated Astrocyte-to-Neuron Conversion. *Front. Cell Dev. Biol.* 8, 591883 (2020).

83. Morrison, R. S., De Vellis, J., Lee, Y. L., Bradshaw, R. A. & Eng, L. F. Hormones and growth factors induce the synthesis of glial fibrillary acidic protein in rat brain astrocytes. *J. Neurosci. Res.* 14, 167–176 (1985).

84. Lei, K. *et al.* Neurogenic differentiation factor 1 promotes colorectal cancer cell proliferation and tumorigenesis by suppressing the p53/p21 axis. *Cancer Sci.* 111, 175–185 (2020).

85. Bäck, S. *et al.* Neuronal Activation Stimulates Cytomegalovirus Promoter-Driven Transgene Expression. *Mol. Ther. - Methods Clin. Dev.* 14, 180–188 (2019).

86. Zheng, C. & Baum, B. J. All Human EF1α Promoters Are Not Equal: Markedly Affect Gene Expression in Constructs from Different Sources. *Int. J. Med. Sci.* 11, 404–408 (2014).

87. Tanida-Miyake, E., Koike, M., Uchiyama, Y. & Tanida, I. Optimization of mNeonGreen for Homo sapiens increases its fluorescent intensity in mammalian cells. *PLOS ONE* 13, e0191108 (2018).

88. Suzuki, T. *et al.* Identification of Basal Promoter and Enhancer Elements in an Untranslated Region of the TT Virus Genome. *J. Virol.* 78, 10820–10824 (2004).

89. Brajão De Oliveira, K. Torque teno virus: a ubiquitous virus. *Rev. Bras. Hematol. E Hemoter.* 37, 357–358 (2015).

90. Wong, R. W. C. & Guillaud, L. The role of epidermal growth factor and its receptors in mammalian CNS. *Cytokine Growth Factor Rev.* 15, 147–156 (2004).

91. Wee, P. & Wang, Z. Epidermal Growth Factor Receptor Cell Proliferation Signaling Pathways. *Cancers* 9, 52 (2017).

92. Seshacharyulu, P. *et al.* Targeting the EGFR signaling pathway in cancer therapy. *Expert Opin. Ther. Targets* 16, 15–31 (2012).

93. Lahusen, T., Fereshteh, M., Oh, A., Wellstein, A. & Riegel, A. T. Epidermal Growth Factor Receptor Tyrosine Phosphorylation and Signaling Controlled by a Nuclear Receptor Coactivator, Amplified in Breast Cancer 1. *Cancer Res.* 67, 7256–7265 (2007).

94. Koss, K. M. *et al.* Toward discovering a novel family of peptides targeting neuroinflammatory states of brain microglia and astrocytes. *J. Neurochem.* jnc.15840 (2023) doi:10.1111/jnc.15840.

95. Green, M. R. & Sambrook, J. Preparation of Single-Stranded Bacteriophage M13 DNA by Precipitation with Polyethylene Glycol. *Cold Spring Harb. Protoc.* 2017, pdb.prot093419 (2017).

96. Stetefeld, J., McKenna, S. A. & Patel, T. R. Dynamic light scattering: a practical guide and applications in biomedical sciences. *Biophys. Rev.* 8, 409–427 (2016).

97. The principles of dynamic light scattering. *Anton Paar.* https://wiki.anton-paar.com/ch-de/das-prinzip-der-dynamischen-lichtstreuung/ (2026)

98. Day, L. A. Conformations of single-stranded DNA and coat protein in fd bacteriophage as revealed by ultraviolet absorption spectroscopy. *J. Mol. Biol.* 39, 265–277 (1969).

99. Quantification of Bacteriophage by Spectrophotometry. *Antibody Design Labs.* https://www.abdesignlabs.com/technical-resources/bacteriophage-spectrophotometry/ (2013).

100. Tang, Y. *et al.* Involvement of HECTD1 in LPS-induced astrocyte activation via σ-1R-JNK/p38-FOXJ2 axis. *Cell Biosci.* 11, 62 (2021).

101. Open Source Computer Vision Library. *OpenCV*. https://opencv.org (2025).

102. Stringer, C., Wang, T., Michaelos, M. & Pachitariu, M. Cellpose: a generalist algorithm for cellular segmentation. *Nat. Methods* 18, 100–106 (2021).

103. Delgado-García, L. M. *et al.* Dissecting reactive astrocyte responses: lineage tracing and morphology-based clustering. *Biol. Res.* 57, 54 (2024).

104. Western Blot SDS-PAGE. *Novus Biologicals.* https://www.novusbio.com/support/support-by-application/western-blot-sds-page (2025).

105. Inagaki, M., IMakamura, Y., Takeda, M., Nishimura, T. & Inagaki, N. Glial Fibrillary Acidic Protein: Dynamic Property and Regulation by Phosphorylation. *Brain Pathol.* 4, 239–243 (1994).

106. Crowley, L. C. *et al.* Measuring Cell Death by Propidium Iodide Uptake and Flow Cytometry. *Cold Spring Harb. Protoc.* 2016, pdb.prot087163 (2016).

107. Quartu, M. *et al.* Polysialylated-neural cell adhesion molecule (PSA-NCAM) in the human trigeminal ganglion and brainstem at prenatal and adult ages. *BMC Neurosci.* 9, 108 (2008).

108. Liu-Wei, W. *et al.* Sequencing accuracy and systematic errors of nanopore direct RNA sequencing. *BMC Genomics* 25, 528 (2024).

109. Dharmaraj, T. *et al.* Rapid assessment of changes in phage bioactivity using dynamic light scattering. *PNAS Nexus* 2, pgad406 (2023).

110. GFP Dye Profile. *FluoroFinder*. https://app.fluorofinder.com/dyes/82-gfp-ex-max-488-nm-em-max-510-nm (n.d.)

111. tdTomato Dye Profile. *FluoroFinder.* https://app.fluorofinder.com/dyes/148-tdtomato-exmax-554-nm-em-max-581-nm (n.d.)

112. Krieg, A. M. CpG motifs in bacterial DNA and their immune effects. *Annu. Rev. Immunol.* 20, 709–760 (2002).

113. Bost, J. P. *et al.* Delivery of Oligonucleotide Therapeutics: Chemical Modifications, Lipid Nanoparticles, and Extracellular Vesicles. *ACS Nano* 15, 13993–14021 (2021).

114. Wallin, H., Hunaiti, S. & Abrahamson, M. Externally added cystatin C reduces growth of A375 melanoma cells by increasing cell cycle time. *FEBS Open Bio* 11, 1645–1658 (2021).

115. Hetzer, M. W. The nuclear envelope. *Cold Spring Harb. Perspect. Biol.* 2, a000539 (2010).

116. Geller, H. M. & Dubois-Dalcq, M. Antigenic and functional characterization of a rat central nervous system-derived cell line immortalized by a retroviral vector. *J. Cell Biol.* 107, 1977–1986 (1988).

117. Fay, N. & Panté, N. Nuclear entry of DNA viruses. *Front. Microbiol.* 6, 467 (2015).

118. Rouillard, M. E., Sutter, P. A., Durham, O. R., Willis, C. M. & Crocker, S. J. Astrocyte-Derived Extracellular Vesicles (ADEVs): Deciphering their Influences in Aging. *Aging Dis.* 12, 1462–1475 (2021).

119. Fidler, P. S. *et al.* Comparing astrocytic cell lines that are inhibitory or permissive for axon growth: the major axon-inhibitory proteoglycan is NG2. *J. Neurosci. Off. J. Soc. Neurosci.* 19, 8778–8788 (1999).

120. Cotto, B., Natarajaseenivasan, K. & Langford, D. Astrocyte activation and altered metabolism in normal aging, age-related CNS diseases, and HAND. *J. Neurovirol.* 25, 722–733 (2019).

121. Sharma, A., Patro, N. & Patro, I. K. Lipopolysaccharide-Induced Apoptosis of Astrocytes: Therapeutic Intervention by Minocycline. *Cell. Mol. Neurobiol.* 36, 577–592 (2016).

122. Chang, Y.-G. *et al.* Equilibrative nucleoside transporter 2 modulates inosine catabolism to influence astrocyte metabolism and reactivity. *Cell Rep.* 44, 116420 (2025).

123. Schwarz, N. & Leube, R. E. Plasticity of cytoplasmic intermediate filament architecture determines cellular functions. *Curr. Opin. Cell Biol.* 85, 102270 (2023).

124. Snider, N. T. & Omary, M. B. Post-translational modifications of intermediate filament proteins: mechanisms and functions. *Nat. Rev. Mol. Cell Biol.* 15, 163–177 (2014).

125. Weder, J. K. P. & Belitz, H.-D. Protein | Chemistry. in *Encyclopedia of Food Sciences and Nutrition* 4805–4818 (Elsevier, 2003). doi:10.1016/B0-12-227055-X/00978-0.

126. Lawal, O., Ulloa Severino, F. P. & Eroglu, C. The role of astrocyte structural plasticity in regulating neural circuit function and behavior. *Glia* 70, 1467–1483 (2022).

127. Han, J. *et al.* The roles of microglia and astrocytes in neuroinflammation of Alzheimer's disease. *Front. Neurosci.* 19, 1575453 (2025).

128. Liu, L., Liu, J., Bao, J., Bai, Q. & Wang, G. Interaction of Microglia and Astrocytes in the Neurovascular Unit. *Front. Immunol.* 11, 1024 (2020).

129. Pietraszek-Gremplewicz, K. *et al.* Expression level of EGFR and MET receptors regulates invasiveness of melanoma cells. *J. Cell. Mol. Med.* 23, 8453–8463 (2019).

130. Ohtani, T., Ninomiya, H., Okazawa, M., Imamura, S. & Masaki, T. Bromodeoxyuridine-Induced Expression of EndothelinAin A375 Human Melanoma Cells. *Biochem. Biophys. Res. Commun.* 234, 526–530 (1997).

131. Tian, Y. *et al.* Probing the Endocytic Pathways of the Filamentous Bacteriophage in Live Cells Using Ratiometric pH Fluorescent Indicator. *Adv. Healthc. Mater.* 4, 413–419 (2015).

132. Stoneham, C. A., Hollinshead, M. & Hajitou, A. Clathrin-mediated Endocytosis and Subsequent Endo-Lysosomal Trafficking of Adeno-associated Virus/Phage. *J. Biol. Chem.* 287, 35849–35859 (2012).

133. Sartorius, R., D'Apice, L., Prisco, A. & De Berardinis, P. Arming Filamentous Bacteriophage, a Nature-Made Nanoparticle, for New Vaccine and Immunotherapeutic Strategies. *Pharmaceutics* 11, 437 (2019).

134. Behr, J.-P. The Proton Sponge: a Trick to Enter Cells the Viruses Did Not Exploit. *CHIMIA* 51, 34 (1997).

135. Meng, L. *et al.* Nanocapping-enabled charge reversal generates cell-enterable endosomal-escapable bacteriophages for intracellular pathogen inhibition. *Sci. Adv.* 8, eabq2005 (2022).

136. TurboFect in vitro Transfection Reagent. *Thermo Fisher Scientific.* https://tools.thermofisher.com/content/sfs/manuals/MAN0013119_TurboFect_Transfection_Reagent_Considerations_UG.pdf (2012).

137. Aibani, N., Rai, R., Patel, P., Cuddihy, G. & Wasan, E. K. Chitosan Nanoparticles at the Biological Interface: Implications for Drug Delivery. *Pharmaceutics* 13, 1686 (2021).

138. Khan, I. N. *et al.* Chitosan-Based Polymeric Nanoparticles as an Efficient Gene Delivery System to Cross Blood Brain Barrier: In Vitro and In Vivo Evaluations. *Pharmaceuticals* 17, 169 (2024).

139. Karayianni, M., Sentoukas, T., Skandalis, A., Pippa, N. & Pispas, S. Chitosan-Based Nanoparticles for Nucleic Acid Delivery: Technological Aspects, Applications, and Future Perspectives. *Pharmaceutics* 15, 1849 (2023).

140. Suwan, K. *et al.* Next-generation of targeted AAVP vectors for systemic transgene delivery against cancer. *Proc. Natl. Acad. Sci.* 116, 18571–18577 (2019).

141. Ganini, D. *et al.* Fluorescent proteins such as eGFP lead to catalytic oxidative stress in cells. *Redox Biol.* 12, 462–468 (2017).

142. Kalyanaraman, B. & Zielonka, J. Green fluorescent proteins induce oxidative stress in cells: A worrisome new wrinkle in the application of the GFP reporter system to biological systems? *Redox Biol.* 12, 755–757 (2017).

143. Villalpando-Rodriguez, G. E. & Gibson, S. B. Reactive Oxygen Species (ROS) Regulates Different Types of Cell Death by Acting as a Rheostat. *Oxid. Med. Cell. Longev.* 2021, 9912436 (2021).

144. Uenaka, T. *et al.* Prevention of transgene silencing during human pluripotent stem cell differentiation. *Cell Stem Cell* S1934590926000305 (2026) doi:10.1016/j.stem.2026.01.007.

145. Chung, S. *et al.* Analysis of different promoter systems for efficient transgene expression in mouse embryonic stem cell lines. *Stem Cells* 20, 139–145 (2002).

146. Lo, P.-K. *et al.* MethySYBR, a Novel Quantitative PCR Assay for the Dual Analysis of DNA Methylation and CpG Methylation Density. *J. Mol. Diagn.* 11, 400–414 (2009).

147. Hong, P., Koza, S. & Bouvier, E. S. P. A Review Size-Exclusion Chromatography For The Analysis Of Protein Biotherapeutics And Their Aggregates. *J. Liq. Chromatogr. Relat. Technol.* 35, 2923–2950 (2012).

148. Zakharova, M. Yu. *et al.* Purification of Filamentous Bacteriophage for Phage Display using Size-Exclusion Chromatography. *BioTechniques* 38, 194–198 (2005).

149. Faust, C., Beil, C., Dittrich, W., Rao, E. & Langer, T. Impact of lipopolysaccharides on cultivation and recombinant protein expression in human embryonal kidney (HEK-293) cells. *Eng. Life Sci.* 21, 778–785 (2021).

150. Uyanga Tsedev, U. T. Engineering M13 Bacteriophage Nanoplatforms for Diagnostic and Therapeutic Applications. (Massachusetts Institute Of Technology, Massachusetts, USA, 2021).

151. Negri, J., Menon, V. & Young-Pearse, T. L. Assessment of Spontaneous Neuronal Activity *In Vitro* Using Multi-Well Multi-Electrode Arrays: Implications for Assay Development. *eneuro* 7, ENEURO.0080-19.2019 (2020).

152. Grienberger, C., Giovannucci, A., Zeiger, W. & Portera-Cailliau, C. Two-photon calcium imaging of neuronal activity. *Nat. Rev. Methods Primer* 2, 67 (2022).

153. Iwabuchi, S., Kakazu, Y., Koh, J.-Y., Goodman, K. M. & Harata, N. C. Examination of Synaptic Vesicle Recycling Using FM Dyes During Evoked, Spontaneous, and Miniature Synaptic Activities. *J. Vis. Exp.* 50557 (2014) doi:10.3791/50557.

154. Handy, D. E., Castro, R. & Loscalzo, J. Epigenetic Modifications: Basic Mechanisms and Role in Cardiovascular Disease. *Circulation* 123, 2145–2156 (2011).

155. Zhang, L. *et al.* Small Molecules Efficiently Reprogram Human Astroglial Cells into Functional Neurons. *Cell Stem Cell* 17, 735–747 (2015).

156. Bathina, S. & Das, U. N. Brain-derived neurotrophic factor and its clinical implications. *Arch. Med. Sci.* 6, 1164–1178 (2015).

Appendix A: Media and Buffer Compositions

Solution	Preparation	Use Case
Ampicillin Stock	Dissolve 500 mg of ampicillin sodium salt in 10 mL sterile Milli-Q water to reach 50 mg/mL. Filter-sterilize (0.22 μm), aliquot, and store at -20 °C.	Selective marker for precursor phagemids in *E. coli*; added to broth at 100 μg/mL
Kanamycin Stock	Dissolve 500 mg of kanamycin sulfate in 10 mL sterile Milli-Q water to reach 50 mg/mL. Filter-sterilize (0.22 μm), aliquot, and store at -20 °C.	Selective marker for helper phage plasmids in *E. coli*; added to broth at 70 μg/mL.
4X Laemmli Buffer	The solution was prepared to a final volume of 10 mL. First, 3 mL of ultra-pure water and 2.5 mL of 1 M Tris–HCl (pH 6.8) were combined in a clean tube. Next, 0.8 g SDS was added, and the mixture was heated to 50–60 °C until fully dissolved. Subsequently, 4.0 mL glycerol and bromophenol blue were added, and the volume was adjusted to 10 mL with Milli-Q water. After cooling to room temperature, 2.0 mL β-mercaptoethanol was added. The buffer was mixed, aliquoted, and stored at -20 °C.	Added to protein samples to ensure that proteins are denatured, solubilized, and carry a uniform negative charge for electrophoresis.
Luria Bertani (LB) Broth	Dissolve 12.5 g of LB powder (Catalog # 12795027, Thermo Fisher Scientifics, Waltham, USA) in 400 mL Milli-Q water. Adjust volume to 500 L. Sterilize via autoclave, store at room temperature.	Nutrient rich liquid medium used for growth of bacteria in culture.

LB Agar	Dissolve 1.5 g of LB powder, and 0.65 g of agar powder in 90 mL Milli-Q water. Adjust volume to 100 mL. Sterilize via autoclave, store at 55 °C water bath.	Nutrient rich solid medium used for growth of bacteria in culture.
LB Top Agar	Dissolve 1.5 g of LB powder, and 0.65g of agar powder in 90 mL Milli-Q water. Adjust volume to 100 mL. Sterilize via autoclave, store at 55 °C water bath.	Semi-solid overlay on regular nutrient agar plates that allows miniphagemids to diffuse through the media to infect plated bacterial culture.
PEG (Polyethylene Glycol)/NaCl solution (pH 7.8)	Dissolve 20 g of PEG8000 (Catalog # AA43443A3, Thermo Fisher Scientifics, Waltham, USA) in 50 mL of 5M NaCl (Catalog # AC424290010, Thermo Fisher Scientifics, Waltham, USA) and adjust the volume to 100 mL with Milli-Q water. Allow to stir overnight. Do not autoclave, and store at room temperature.	Used to precipitate miniphagemid particles for purification.
Protein Lysis Buffer	Combine 20 mM Tris-HCl (pH 7.5),150 mM NaCl, 1 mM EDTA, 1 mM EGTA, 30 mM sodium pyrophosphate, 1 mM betaglycerophosphate, 1 mM sodium orthovanadate (Na3VO4), 1% triton X-100. Mix thoroughly avoiding foaming. Add protease inhibitors (Catalog # 78446, Thermo Fisher Scientifics, Waltham, USA) immediately before use.	Breaks the mammalian cell membrane releasing the cell contents and proteins. I mproves protein stability in the solution.
10X Running Buffer (pH 8.3)	Dissolve 30.3 g Tris Base, 144 g Glycine, and 10 g SDS (0.1% w/v) in 1 L Milli-Q water. Store at room temperature. Dilute to 1X before use.	Supports protein migration through gel electrophoresis.

8% Resolving Gel Buffer (pH 8.8)	Mix 3 mL of 1.0 M Tris-HCl (pH 8.8), 2 mL of 30% Acrylamide, 38 µL of 20% SDS, and 2.43 mL of Milli-Q water. To solidify add 36 µL of 10% APS and 5 µL of TEMED. Use immediately, overlay with ethanol and let sit for ~30 min	Provides a small-pore matrix to separate proteins based on molecular weight as they migrate through the gel.
4% Stacking Gel Buffer (pH 6.8)	Mix 630 µL of 1 M Tris-HCl (pH 6.8), 660 µL of 30% Acrylamide, 25 µL of 20% SDS, and 3.6 mL of Milli-Q water. To solidify add 25 µL of 10% APS and 5 µL of TEMED. Insert comb immediately after pouring, and let sit for ~30 min.	Provides a large-pore matrix to collect proteins into a uniform band before they enter the resolving gel.
10X TBS-T	Dissolve 15.2 mM Tris-HCl, 4.62 mM Tris base and 150 mM NaCl (pH 7.6). Add 0.1% of Tween 20. 1X TBS-T buffer was made by diluting 10X TBS in Milli-Q water.	Washing buffer for protein carrying nitrocellulose membranes used in western blot and dot blot assays.
TN Buffer (pH 7.8)	Dissolve 5.84 g of NaCl (0.1 M) and 1.21 g of Tris-HCl (0.01 M) in 1 L Milli-Q water. Adjust pH to 7.8 and autoclave. Store at room temperature.	pH stabilizing media for long-term storage of miniphagemids at 4 °C.
Transfer Buffer	Dissolve 3.03 g of Tris Base and 14.4 g of Glycine in 700 mL L Milli-Q water. Add 200 mL Methanol (20% final concentration). Adjust volume to 1 L. Store at 4 °C.	Facilitates protein transfer from the gel to the nitrocellulose membrane.
1X Tris-Acetate-EDTA (TAE) Buffer	Mix 20 mL of 50X TAE Stock (2 M Tris-acetate, 50 mM EDTA) with 980 mL of Milli-Q water.	Running buffer for DNA migration through agarose gel electrophoresis.

Appendix B: Restriction Digestion Enzymes

Table 13: Summary of Restriction Enzymes

Restriction Enzyme	Digested Plasmids	Restriction Site	Source
EcoRI-HF	pAI1, pAI2, pAI3, pJL1, pJL2, pJL3, p326, pAI1/pAI2/pAI3 combined with SW8-EGF, pJL1/pJL2/pJL3 combined with SW8-EGF	5′-G|AATTC-3′	NEB
SacII-HF	pAI1, pAI2, pAI3, pLuNe, p326	5′-C|CGCG-3′	NEB
PvuI-HF	pJL1, pJL2, pJL3, pLuNe, p326, pLuNe combined with SW8-SF/SW8-SG/SW8-SL	5′-CGAT|CG-3′	NEB
HindIII-HF	pFlex Switch, SW8-IRL1620, SW8-EGF, SW8-EGFSF, SW8-SF, SW8-SG, SW8-SL, p326, pJL1/pJL2/pJL3 combined with SW8-IRL1620/SW8-SF/SW8-SG/ SW8-SL/SW8-EGFSF	5′-A|AGCTT-3′	NEB
PacI	SW8-IRL1620, SW8-EGF, SW8-EGFSF, SW8-SF, SW8-SG, SW8-SL, p326	5′-TTAAT|TAA-3′	NEB
AfeI	SW8-EGF, p326	5′-AGC|GCT-3′	NEB

NEB: New England BioLabs (Ipswich, USA)

Appendix C: Phage Display Sequences

EGF:
AATAGTGACTCTGAATGTCCCCTGTCCCACGATGGGTACTGCCTCCATGATGGTGTGT
GCATGTATATTGAAGCATTGGACAAGTATGCATGCAACTGTGTTGTTGGCTACATCG
GGGAGCGATGTCAGTACCGAGACCTGAAGTGGTGGGAACTGCGC

IRL1620: GACAAAGAATGCGTTTACTTTTGCCATCTAGACATAATATGG

SFSNIAIR: AGCTTTAGCAACATTGCGATTCGC

SGNSTSNA: AGCGGCAACAGCACCAGCAACGCG

SLSAVDVS: AGCCTGAGCGCGGTGGATGTGAGC

Appendix D: Supplementary AGE Data

D-1 Restriction Digest Analysis of Plasmid Constructs

To check for the structural integrity and any large-scale deletions or insertions in the constructs used for this project, plasmids were subjected to a double restriction digest, in which dsDNA was cut using two restriction enzymes. The produced fragments were analyzed by size separation via AGE, and the expected fragment sizes for each construct are listed in Table 14. Each set of DNA samples was run alongside the p326 positive control plasmid shown in Figure 6, digested with the same enzymes. Undigested plasmids were also run on the same gel as negative controls. 1 kb Plus DNA ladder (Catalog # N3200S, NEB, Ipswich, USA) used for size estimation is composed of 19 DNA fragments ranging in size from 100 bp to 1 kb. 0.8% agarose gel was used in this experiment which is suitable for fragment sizes from 500 bp to 10,000 bp (Thermo Fisher Scientific, Waltham, USA). Each DNA fragment that is run on the gel is seen as a band.

Table 14: Expected Fragment Sizes from Double Restriction Digest of Plasmids

Plasmid	Restriction Enzymes Used	Expected Fragment Sizes (kbp)
pAI1	EcoRI-HF and SacII-HF	2.5 + 5.4
pAI2		2.5 + 4.3
pAI3		1.3 + 5.4
pJL1	EcoRI-HF and PvuI-HF	3.1 + 5.8
pJL2		1.9 + 5.8
pJL3		3.1 + 4.6
Flex Switch	HindIII-HF (2 cut sites)	3.2 + 6.3
pLuNe	PvuI-HF and SacII-HF	2.4 + 5.6
SW8-IRL1620	HindIII-HF and PacI	3.9 + 4.5
SW8-EGF	HindIII-HF and AfeI	3.9 + 4.5
SW8-EGFSF	HindIII-HF and PacI	2.8 + 5.6
SW8-SF		2.8 + 5.4
SW8-SG		2.8 + 5.4
SW8-SL		2.8 + 5.4

Figure 27 presents agarose gel images of digested AI plasmids, which are consistent with the expected fragment sizes and digestion patterns. The p326 positive control plasmid (6.8 kbp) produced expected bands upon digestion with EcoRI-HF and SacII-HF. AI1 (7.9 kbp), AI2 (6.8 kbp), and pAI3 (6.8 kbp) plasmids generally exhibited expected digestion patterns; however, pAI1 and pAI2 displayed unexpected bands above 10 kb, likely due to incomplete digestion. AI3 digestion resulted in an additional ~2.0 kb band, likely due to cleavage between M13 start and stop codons.

To gain additional confidence in plasmid integrity, these precursor plasmids were subjected to a second round of double restriction digest using EcoRI-HF and PvuI-HF RE. The second digest

produced bands that matched the expectations, and the corresponding agarose gel images can be found in Appendix D-2.

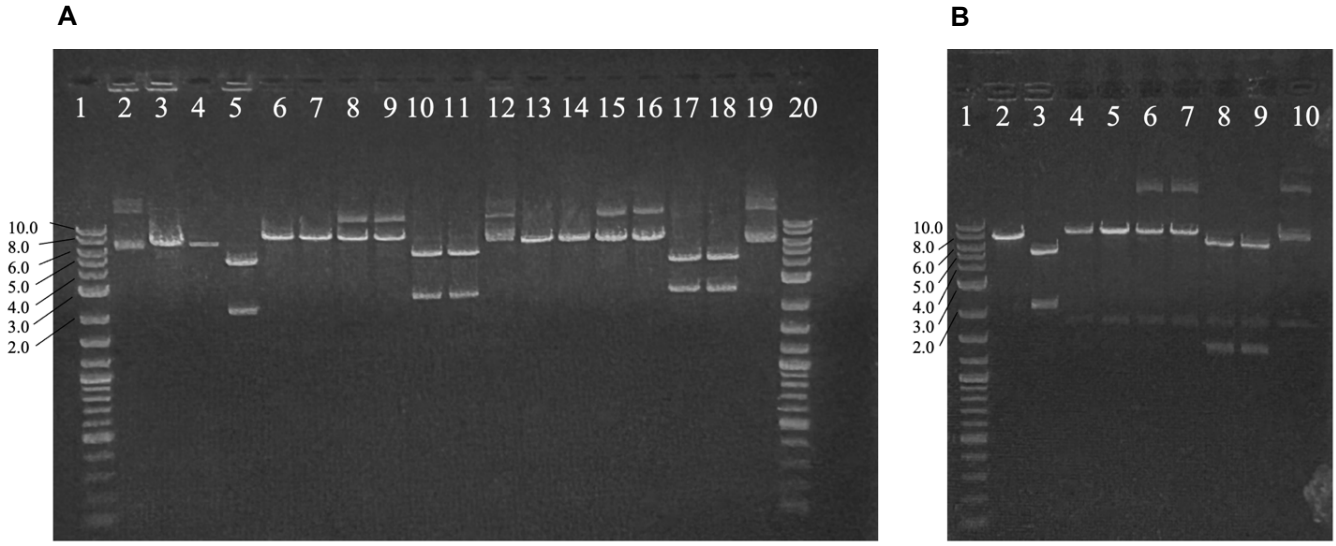


Figure 27: Agarose Gel of Restriction Digest of AI Plasmid DNA for Verification

DNA extracted from *E. coli* JM109 cells transformed with pAI1, pAI2, and pAI3 precursor plasmids was digested using EcoRI-HF and SacII-HF RE and run on a 0.8% agarose gel for 1hr and 30 min.
A) Gel of the digested pAI1 and ApI2 plasmids.
Lane 1&20: 1kb plus DNA Ladder labelled in kb.
Lane 2: undigested p326, lane 3: p326 digested with EcoRI-HF, lane 4: p326 digested with SacII-HF, lane 5: p326 digested with EcoRI-HF and SacII-HF.
Lane 6&7: pAI1 digested with EcoRI-HF, lane 8&9: pAI1 digested with SacII-HF, lane 10&11: pAI1 digested with EcoRI-HF and SacII-HF, lane 12: undigested pAI1.
Lane 13&14: pAI2 digested with EcoRI-HF, lane 15&16: pAI2 digested with SacII-HF, lane 17&18: pAI2 digested with EcoRI-HF and SacII-HF, lane 19: undigested pAI2.
B) Gel of the digested pAI3 plasmid.
Lane 1: 1kb plus DNA Ladder labelled in kb.
Lane 2: p326 digested with EcoRI-HF, lane 3: p326 digested with EcoRI-HF and SacII-HF.
Lane 4&5: pAI3 digested with EcoRI-HF, lane 6&7: pAI3 digested with SacII-HF, lane 8&9: pAI3 digested with EcoRI-HF and SacII-HF, lane 10: undigested pAI3.

Figure 28 presents agarose gel images of digested JL plasmids, which are consistent with the expected fragment sizes and digestion patterns. The positive control plasmid, p326 (6.8 kbp), showed expected band patterns (4412 bp + 1046 bp + 1378 bp) following digestion with EcoRI-HF and PvuI-HF. The pJL1 (8.9 kbp), pJL2 (7.7 kbp), and pJL3 (7.7 kbp) plasmids also produced

expected fragment sizes when digested with EcoRI-HF and PvuI-HF, supporting the structural integrity of these constructs.

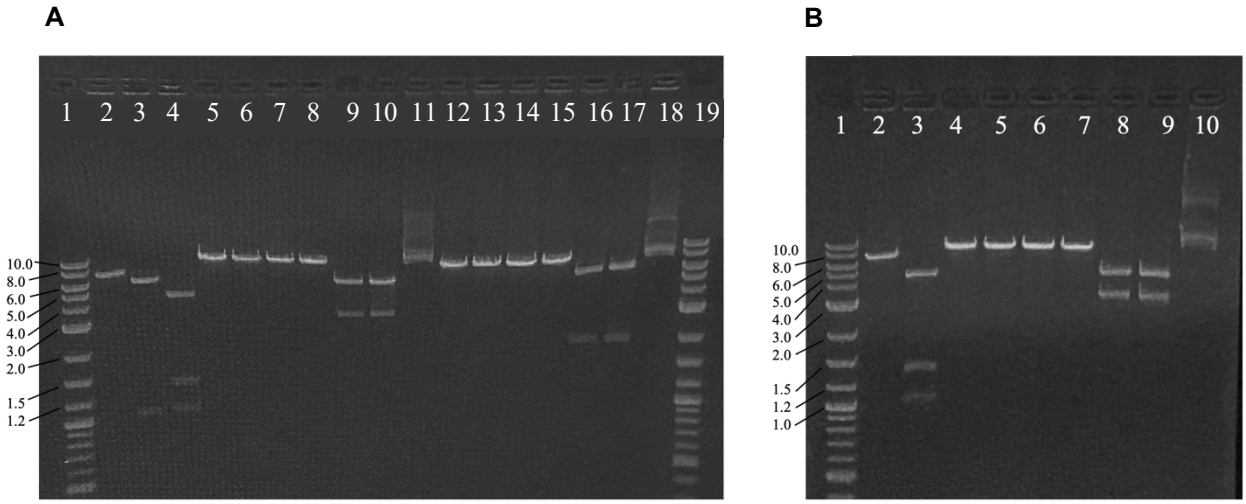


Figure 28: Agarose Gel of Restriction Digest of JL Plasmid DNA for Verification

DNA extracted from *E. coli* JM109 cells transformed with pJL1, pJL2, and pJL3 precursor plasmids was digested using EcoRI-HF and PvuI-HF RE and subsequently run on a 0.8% agarose gel for 1hr and 30 min.
A) Gel of the digested pJL1 and pJL2 plasmids.
Lane 1&20: 1kb plus DNA Ladder labelled in kb.
Lane 2: p326 digested with EcoRI-HF RE, lane 3: p326 digested with PvuI-HF, lane 4: p326 digested with EcoRI-HF and PvuI-HF.
Lane 5&6: pJL1 digested with EcoRI-HF, lane 7&8: pJL1 digested with PvuI-HF, lane 9&10: pJL1 digested with EcoRI-HF and PvuI-HF, lane 11: undigested pJL1.
Lane 12&13: pJL2 digested with EcoRI-HF, lane 14&15: pJL2 digested with PvuI-HF, lane 16&17: pJL2 digested with EcoRI-HF and PvuI-HF, lane 18: undigested pJL2.
B) Gel of the digested pJL3 plasmid.
Lane 1: 1kb plus DNA Ladder labelled in kb.
Lane 2: p326 digested with EcoRI-HF, lane 3: p326 digested with EcoRI-HF and PvuI-HF.
Lane 4&5: pJL3 digested with EcoRI-HF, lane 6&7: pJL3 digested with PvuI-HF, lane 8&9: pJL3 digested with EcoRI-HF and PvuI-HF, lane 10: undigested pJL3.

Figure 29-A presents agarose gel image of digested Flex Switch plasmid, which is consistent with the expected fragment sizes and digestion patterns. The positive control plasmid, p326, showed expected band patterns following the digestion with HindIII-HF. Flex Switch. (9.5 kbp) also produced expected fragment sizes when digested with HindIII-HF, which has two cut cites within the plasmid. Figure 29-B presents agarose gel image of digested pLuNe plasmid

(8.1 kbp). Digestion with PvuI-HF and SacII-HF RE produced fragment sizes consistent with the expected band sizes.

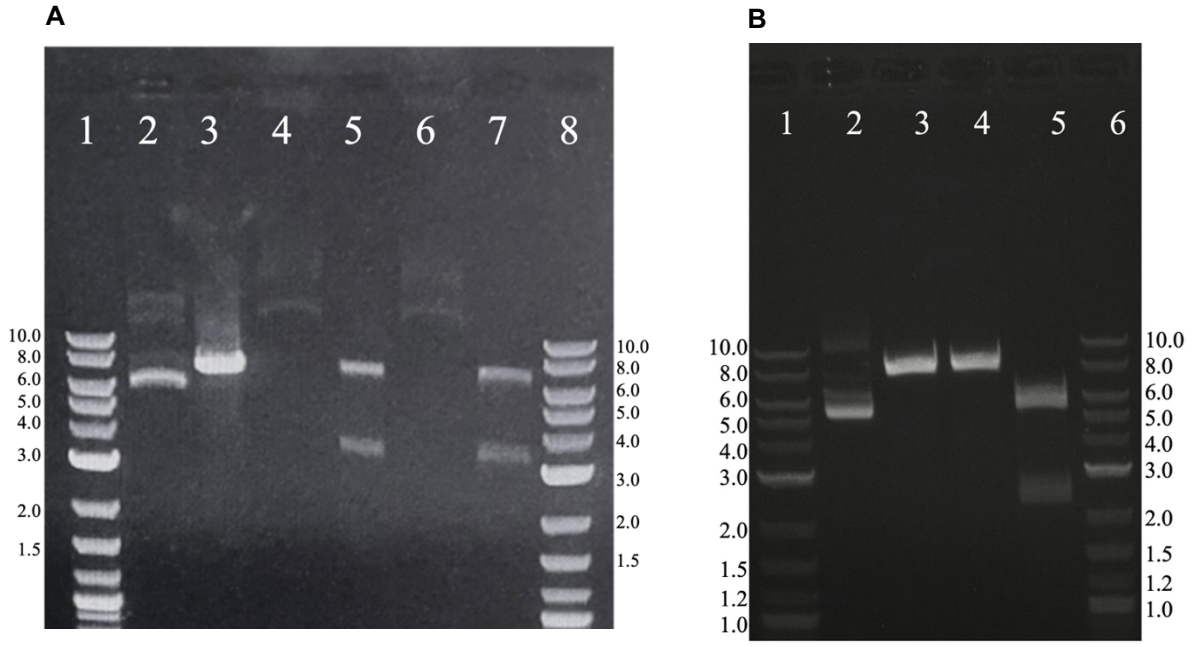


Figure 29: Agarose Gel of Restriction Digest of Flex Switch and pLuNe Plasmid DNA for Verification

A) DNA extracted from *E. coli* JM109 cells transformed with Flex Switch precursor plasmid was digested using HindIII-HF RE with 2 cut sites on the plasmids and subsequently run on a 0.8% agarose gel for 1hr and 30 min.
Lanes 1&8: 1kb plus DNA Ladder labelled in kb.
Lane 2: undigested p326, lane 3: p326 digested with HindIII-HF RE.
Lanes 4 & 6: undigested Flex Switch, lanes 5 & 7: Flex Switch digested with HindIII- HF RE.
B) DNA extracted from *E. coli* JM109 cells transformed with pLuNe precursor plasmid was digested using PvuI-HF RE and SacII-HF and subsequently run on a 0.8% agarose gel for 1hr and 30 min.
Lanes 1&6: 1kb plus DNA Ladder labelled in kb.
Lane 2: undigested pLuNe, lane 3: pLuNe digested with PvuI-HF RE.
Lanes 4: pLuNe digested with SacII-HF, lane 5: pLuNe digested with PvuI-HF and SacII-HF RE.

Figure 30-A presents agarose gel image of digested SW8-EGF helper plasmid, which is consistent with the expected fragment sizes and digestion patterns. The positive control plasmid, p326, showed expected band patterns with HindIII-HF and AfeI digestion (0.7 kbp + 2.3 kbp + 3.8 kbp). SW8-EGF (8.4 kbp) also produced expected fragment sizes when digested with HindIII-HF and AfeI. Figure 30-B presents agarose gel image of digested SW8-IRL1620 helper plasmid, which

is consistent with the expected fragment sizes and digestion patterns. The positive control plasmid, p326, showed one band ~3.0 kbp band following digestion with HindIII-HF and PacI. This is possible given that two of the expected bands are the same size (2.9 kbp + 2.9 kbp + 1.0 kbp) and will overlap, while the third band is just too faint to see and is also small enough to diffuse or run off the gel. However, SW8- IRL1620 (8.3 kbp) produced expected fragment sizes when digested with HindIII-HF and PacI.

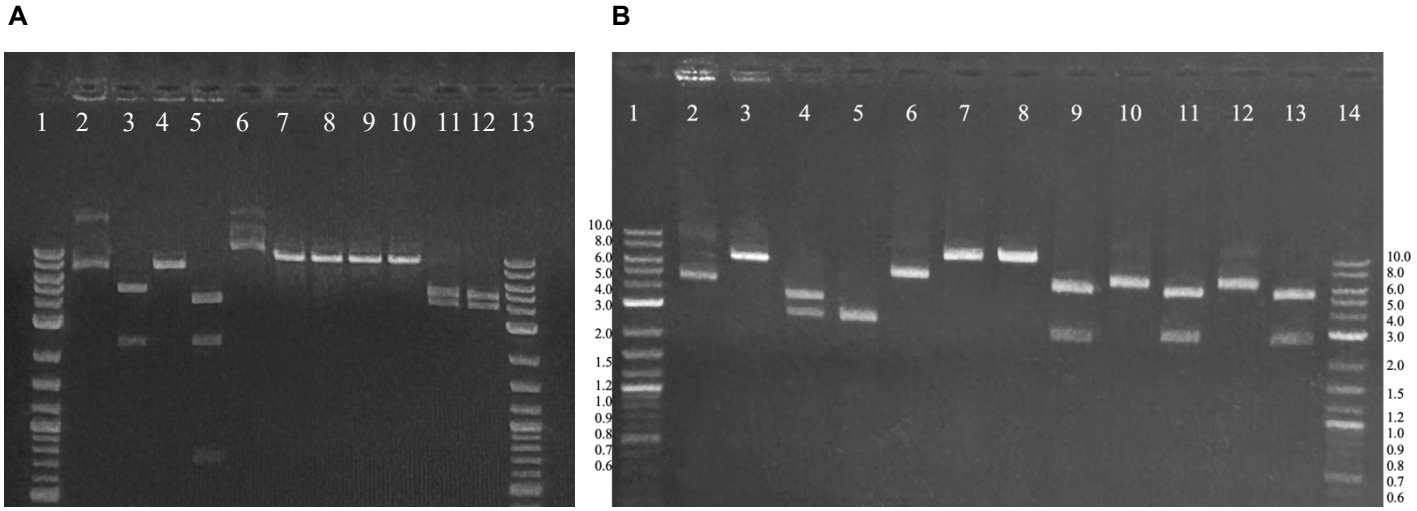


Figure 30: Agarose Gel of Restriction Digest of SW8-EGF and SW8-IRL1620 Plasmid DNA for Verification

A) DNA extracted from *E. coli* JM109 cells transformed with SW8-EGF helper plasmid was digested using HindIII-HF and AfeI RE and subsequently run on a 0.8% agarose gel for 1hr and 30 min.
Lane 1&13: 1kb plus DNA Ladder labelled in kb.
Lane 2: undigested p326, lane 3: p326 digested with HindIII-HF, lane 4: p326 digested with AfeI. Lane 5: p326 digested with HindIII-HF and AfeI.
Lane 6: undigested SW8-EGF. Lane 7&8: SW8-EGF digested with HindIII-HF, lane 9&10: SW8-EGF digested with AfeI, lane 11&12: SW8-EGF digested with HindIII-HF and AfeI.
B) DNA extracted from *E. coli* JM109 cells transformed with SW8-IRL1620 helper plasmid was digested using HindIII-HF + PacI RE and subsequently run on a 0.8% agarose gel for 1hr and 30 min.
Lane 1&13: 1kb plus DNA Ladder labelled in kb.
Lane 2: undigested p326, lane 3: p326 digested with HindIII-HF, lane 4: p326 digested with PacI.
Lane 5: p326 digested with HindIII-HF and PacI. Lane 6: undigested SW8-EGF.
Lane 7&8: SW8-EGF digested with HindIII-HF, lane 9&10: SW8-EGF digested with PacI, lane 11&12: SW8-EGF digested with HindIII-HF and PacI.

Figure 31 presents agarose gel image of digested SW8-SF, SW8-SG, SW8-SL, and SW8-EGFSF helper plasmids, which are consistent with the expected fragment sizes and digestion patterns when cut with HindIII-HF and PacI. The positive control plasmid, p326, is not shown, as it was digested with the same restriction enzymes and run on a separate agarose gel together with SW8-IRL1620 (Figure 30).

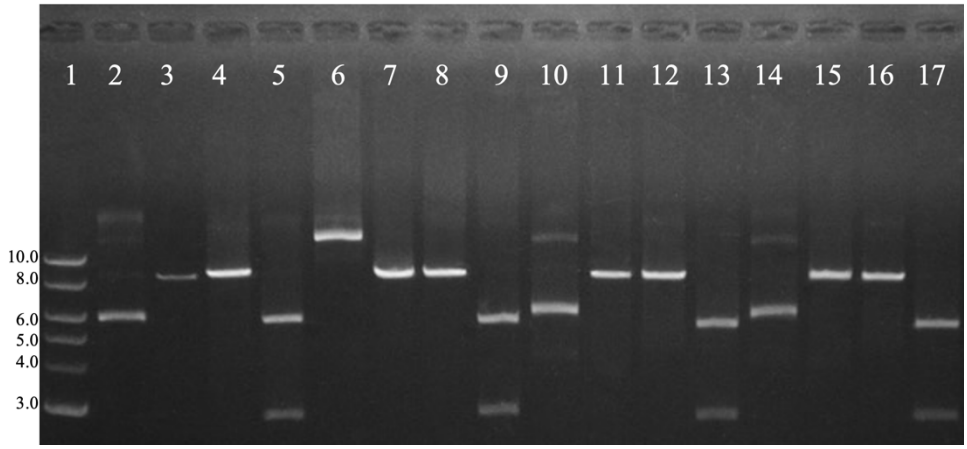


Figure 31: Agarose Gel of Restriction Digest of SW8-SF, SW8-SG, SW8-SL, and SW8-EGFSF Plasmid DNA for Verification

DNA extracted from *E. coli* JM109 cells transformed with SW8-SF, SW8-SG, SW8-SL, and SW8-EGFSF helper plasmids was digested using HindIII-HF + PacI RE and subsequently run on a 0.8% agarose gel for 1hr and 30 min.
Lane 1: 1kb plus DNA Ladder labelled in kb.
Lane 2: undigested SW8-SF, lane 3: SW8-SF digested with HindIII-HF, lane 4: SW8-SF digested with PacI, lane 5: SW8-SF digested with HindIII-HF and PacI.
Lane 6: undigested SW8-SG, lane 7: SW8-SG digested with HindIII-HF, lane 8: SW8-GS digested with PacI, lane 9: SW8-SG digested with HindIII-HF and PacI.
Lane 10: undigested SW8-SL, lane 11: SW8-SL digested with HindIII-HF, lane 12: SW8-SL digested with PacI, lane 13: SW8-SL digested with HindIII-HF and PacI.
Lane 14: undigested SW8-EGFSF, lane 15: SW8- EGFSF digested with HindIII-HF, lane 16: SW8- EGFSF digested with PacI, lane 17: SW8- EGFSF digested with HindIII-HF and PacI.

The restriction digest analysis presented here has provided an initial assessment of plasmid structural integrity and large-scale mutations. For plasmids where the observed fragment sizes matched the expectations, this suggests that the tested plasmids contain the expected restriction sites, and that major structural mutations, such as large insertions, deletions, or rearrangements, are unlikely. However, when fragment sizes did not match the expectations, this does not necessarily

mean that the entire plasmid sequence is incorrect. Such discrepancies could arise from partial digestion, star activity of the restriction enzymes, gel resolution limitations, or minor mutations that alter enzyme binding sites without affecting the overall plasmid function. Therefore, while restriction digest is useful for detecting major mutations, it does not replace plasmid sequencing for verification of the full sequence.

D-2 Additional Restriction Digest on Precursor and Helper Constructs

Additional restriction digests were performed on the plasmids where initial gel run produced ambiguous bands. Figure 32 illustrates the image of the AGE containing digested SW8-EGF plasmid, which is consistent with the expected fragment sizes and digestion patterns. The positive control plasmid, p326, showed expected band patterns with HindIII-HF RE digestion. SW8-EGF (8.4 kbp) also produced expected fragment sizes (2.8 kbp + 5.6 kbp) when digested with HindIII-HF and PacI REs.

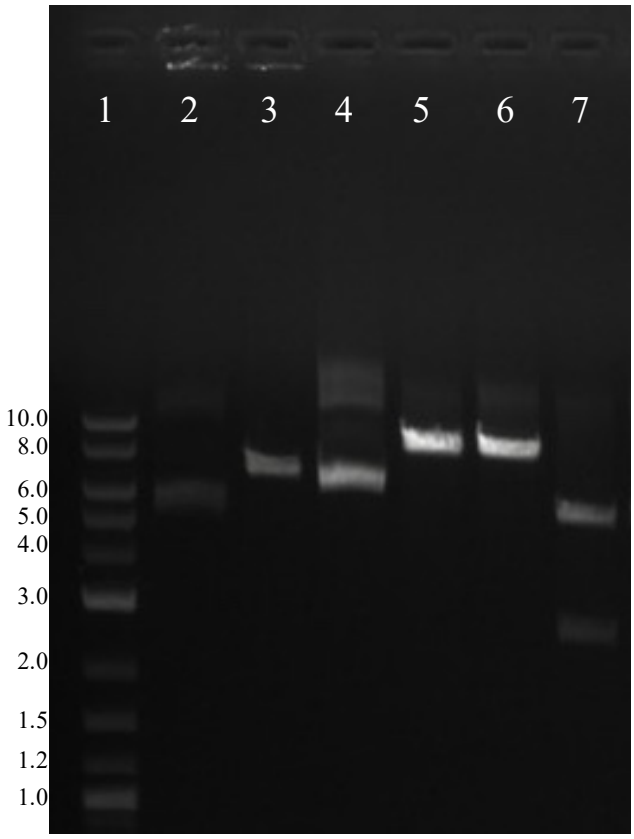


Figure 32: Agarose Gel of Restriction Digest of SW8-EGF Plasmid DNA for Plasmid Verification

DNA extracted from *E. coli* JM109 cells transformed with SW8-EGF helper plasmid was digested using HindIII-HF and PacI RE and subsequently run on a 0.8% agarose gel for 1hr and 30 min.
Lane 1: 1kb plus DNA Ladder labelled in kb.
Lane 2: undigested p326, lane 3: p326 digested with HindIII-HF.
Lane 4: undigested SW8-EGF, lane 5: SW8-EGF digested with HindIII-HF, lane 6: SW8-EGF digested with PacI, lane 7: SW8-EGF digested with HindIII-HF and PacI.

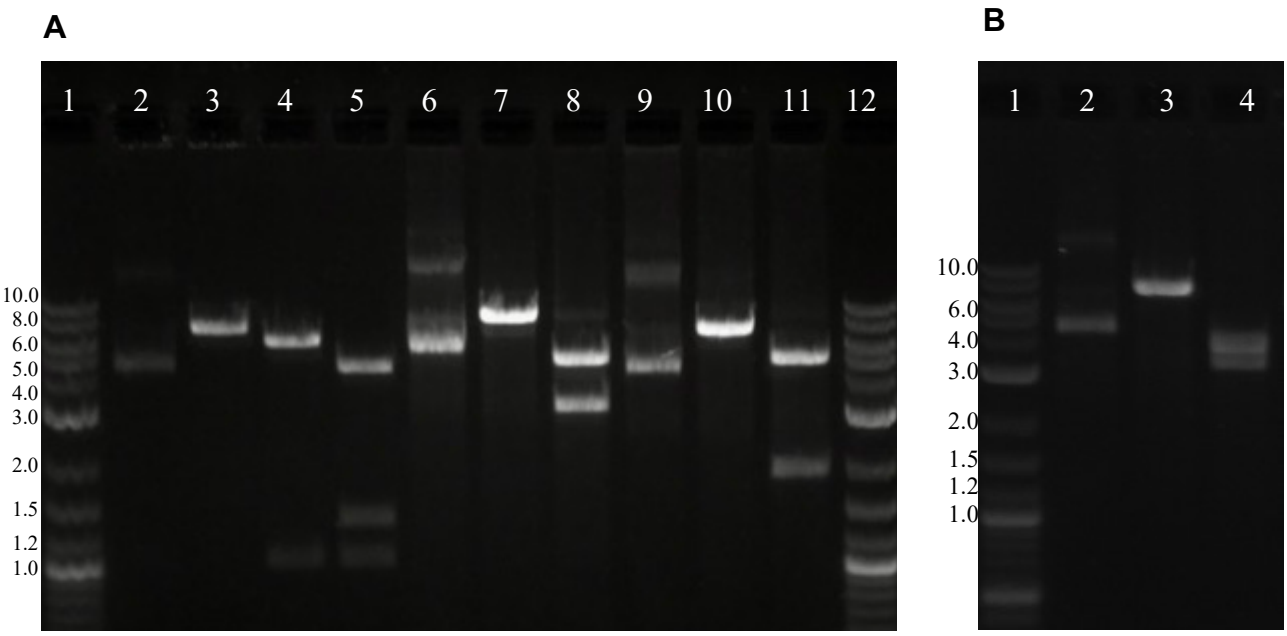


Figure 33: Agarose Gel of Restriction Digest of AI Plasmids DNA for Plasmid Verification

DNA extracted from *E. coli* JM109 cells transformed with pAI1, pAI2, and pAI3 precursor plasmids was digested using EcoRI-HF and PvuI-HF RE and run on a 1% agarose gel for 1hr and 30 min.
A) Gel of the digested pAI1 and pAI2 plasmids.
Lane 1&12: 1kb plus DNA Ladder labelled in kb.
Lane 2: undigested p326, lane 3: p326 digested with EcoRI-HF, lane 4: p326 digested with PvuI-HF, lane 5: p326 digested with EcoRI-HF and PvuI-HF.
Lane 6: undigested pAI1, lane 7: pAI1 digested with EcoRI-HF, lane 8: pAI1 digested with EcoRI-HF and PvuI-HF.
Lane 9: undigested pAI2, lane 10: pAI2 digested with EcoRI-HF, lane 11: pAI2 digested with EcoRI-HF and PvuI-HF.
B) Gel of the digested pAI3 plasmid.
Lane 1: 1kb plus DNA Ladder labelled in kb.
Lane 2: undigested pAI3, lane 3: pAI3 digested with EcoRI-HF, lane 4: pAI3 digested with EcoRI-HF and PvuI-HF.

D-3 Extraction of the Double-Stranded Plasmid DNA from the *E. coli* Pellet

To further assess the plasmids used for miniphagemid production, plasmid DNA was extracted from the cell pellet left after the separation of the miniphagemids from the bacterial cells via centrifugation for 10 min at 8000 × g at 4 °C. Plasmid DNA was extracted from the cells using the Monarch Plasmid Miniprep Kit (New England Biolabs Canada, 2015). The concentration and purity of the extracted DNA were measured using the Thermo Fisher Scientific (Waltham, USA) NanoDrop 2000 spectrophotometer. Plasmid extracts were then subjected to a single restriction digest, where the DNA was cut using one restriction enzyme. DNA extracted from cells transformed with pJL1, pJL2, pJL3, pAI1, pAI2, and pAI3 precursor plasmids, along with the SW8-EGF helper plasmid, was digested using EcoRI-HF RE (NEB, Ipswich, USA). DNA extracted from cells transformed with pJL1, pJL2, and pJL3 precursor plasmids, along with the SW8-IRL1620 helper plasmid, was digested using HindIII-HF RE (NEB, Ipswich, USA). Each test sample was digested in duplicates and DNA was run on a 0.8% agarose gel. Undigested DNA samples were also run on the same gel as negative controls. The digested DNA was visualized via AGE using TAE buffer.

Figure 34 shows AGE results for precursor-helper combination digested with EcoRI-HF RE. pAI1 with SW8-EGF produced three visible bands instead of the expected four, likely due to overlapping bands. The expected band sizes are: SW8-EGF (8399 bp), AI1 (7939 bp), RF dsDNA (6111 bp), and ssDNA (3055 bp). An unexpected 1.2 kb band was observed, and the dsDNA RF factor band was missing. pAI2 with SW8-EGF produced four bands as anticipated. The expected band sizes are: SW8-EGF (8399 bp), pAI2 (6772 bp), RF dsDNA (4937 bp), and ssDNA (2469 bp). This digest also produced an unexpected 1.2 kb band, but not dsDNA RF. pAI3 with SW8-EGF produced multiple unexpected bands (1.7 kb, 1.2 kb, 0.5 kb) and did not confirm the presence of the correct plasmids. Expected sizes: SW8-EGF (8399 bp), AI3 (6757 bp), dsDNA RF (4921

bp), and ssDNA (2461 bp). Overall, AI1 and AI2 miniphagemids may contain the correct plasmids, but AI3 does not. The absence of ssDNA and/or RF dsDNA suggests an issue with miniphagemid production.

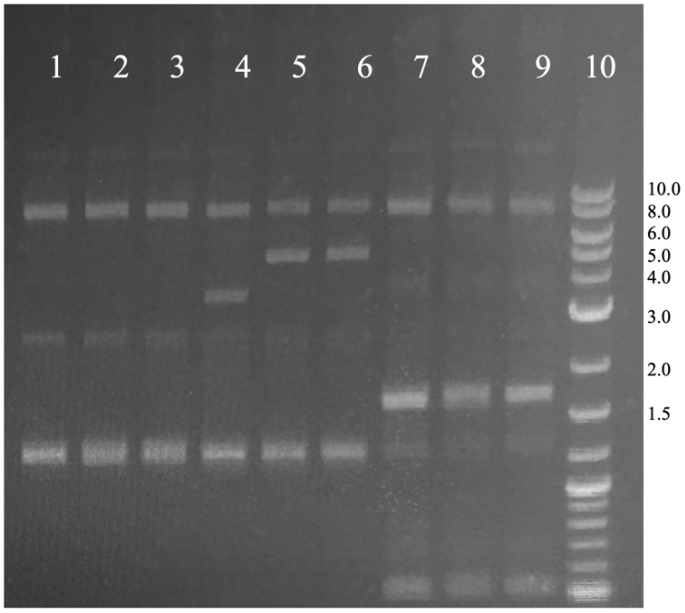


Figure 34: Agarose Gel of Restriction Digest of AI with SW8-EGF Plasmid DNA from Miniphagemid Production

DNA extracted from the JM109 cell pellet during AI miniphagemid production was digested using EcoRI-HF RE and subsequently run on a 0.8% agarose gel for 1hr and 30 min.
Lane 10: 1kb plus DNA Ladder labelled in kb.
Lane 1: undigested pAI1 with SW8-EGF, lane 2&3: pAI1 with SW8-EGF digested with EcoRI-HF.
Lane 4: undigested pAI2 with SW8-EGF, lanes 5&6: pAI2 with SW8-EGF digested with EcoRI-HF.
Lane 7: undigested pAI3 with SW8-EGF, lanes 8&9: pAI3 with SW8-EGF digested with EcoRI-HF.

Figure 35 illustrates AGE results for digested JL and SW8-EGF plasmids. The assay confirmed the expected sizes for the precursor and helper plasmids, as well as RF dsDNA, but not ssDNA. pJL1 with SW8-EGF plasmids produced four bands as anticipated. The expected band sizes are: SW8-EGF (8399 bp), pJL1 (8893 bp), RF dsDNA (7064 bp), and ssDNA (3532 bp), the resulted fragments have matched the expectations except for the ssDNA which was smaller than expected. Similarly, pJL2 with SW8-EGF produced four bands. The expected band sizes are: SW8-EGF (8399 bp), pJL2 (7726 bp), RF dsDNA (5897 bp), and ssDNA (2948 bp), the resulted

fragments have matched the expectations except for the ssDNA which was smaller than expected. pJL3 with SW8-EGF produced also four bands. The expected band sizes are: SW8-EGF (8399 bp), pJL3 (7711 bp), RF dsDNA (5880 bp), and ssDNA (2940 bp), the resulted fragments have matched the expectations except for the ssDNA which was smaller than expected. While the number of bands was as anticipated, the smaller-than-expected sizes of ssDNA suggest a problem with miniphagemid production.

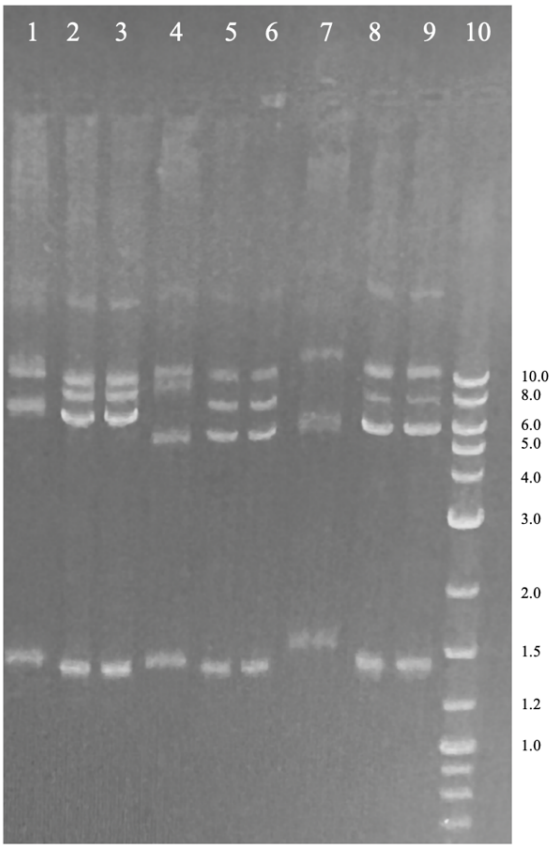


Figure 35: Agarose Gel of Restriction Digest of JL with SW8-EGF Plasmid DNA from Miniphagemid Production

DNA extracted from the JM109 cell pellet during JL-EGF miniphagemid production was digested using EcoRI-HF restriction enzyme and subsequently run on a 0.8% agarose gel for 1hr and 30 min.
Lane 10: 1kb plus DNA Ladder labelled in kb.
Lane 1: undigested pJL1 with SW8-EGF, lane 2&3: pJL1 with SW8-EGF digested with EcoRI-HF.
Lane 4: undigested pJL2 with SW8-EGF, lane 5&6: pJL2 with SW8-EGF digested with EcoRI-HF.
Lane 7: undigested pJL3 with SW8-EGF, lane 8&9: pJL3 with SW8-EGF digested with EcoRI-HF.

Figure 36 illustrates AGE results for digested JL and SW8-IRL1620 plasmids. The assay confirmed the expected sizes for the precursor and helper plasmids. pJL1 with SW8-IRL1620 plasmids produced two bands. The expected band sizes are: SW8-IRL1620 (8281 bp), pJL1 (8893 bp), RF dsDNA (7064 bp), and ssDNA (3532 bp), the resulted bands matched the sizes for the precursor and helper plasmids. Similarly, pJL2 with SW8- IRL1620 produced two bands. The expected band sizes are: SW8- IRL1620 (8281 bp), pJL2 (7726 bp), RF dsDNA (5897 bp), and ssDNA (2948 bp), the resulted bands matched the sizes for the precursor and helper plasmids. JL3 with SW8- IRL1620 also produced two bands. The expected band sizes are: SW8- IRL1620 (8281 bp), pJL3 (7711 bp), RF dsDNA (5880 bp), and ssDNA (2940 bp), the resulted bands matched the sizes for the precursor and helper plasmids. The absence of RF dsDNA and ssDNA doesn't necessarily mean that there is a problem with miniphagemids since the presence of those intermediate forms depends on where cells are in the miniphagemid production cycle.

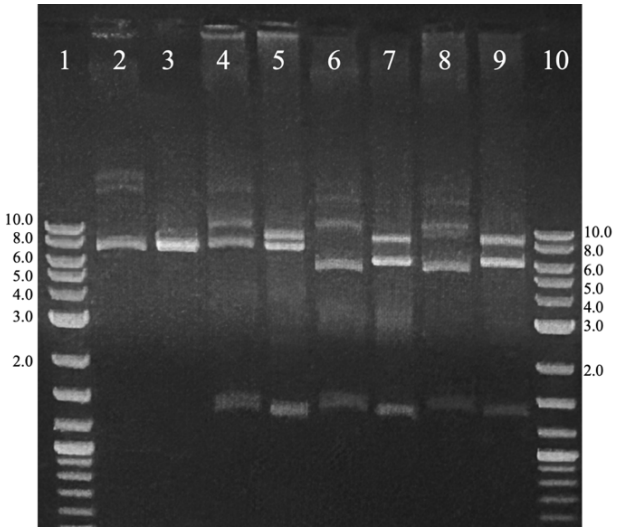


Figure 36: Agarose Gel of Restriction Digest of JL with SW8-IRL1620 Plasmid DNA from Miniphagemid Production

DNA extracted from the JM109 cell pellet during JL-IRL1602 miniphagemid production was digested using HindIII-HF RE and subsequently run on a 0.8% agarose gel for 1hr and 30 min.
Lane 1&10: 1kb plus DNA Ladder labelled in kb.
Lane 2: undigested p326 (positive control), lane 3: p326 digested with HindIII-HF.
Lane 4: undigested pJL1 with SW8- IRL1620, lane 5: pJL1 with SW8- IRL1620 digested with HindIII-HF.
Lane 6: undigested pJL2 with SW8- IRL1620, lane 7: pJL2 with SW8- IRL1620 digested with HindIII-HF.
Lane 8: undigested pJL3 with SW8- IRL1620, lane 9: pJL3 with SW8- IRL1620 digested with HindIII-HF.

Figure 37 illustrates AGE results for digested Flex Switch and SW8-IRL1620 plasmids. The assay confirmed the expected sizes for the precursor and helper plasmids. Flex Switch with SW8-IRL1620 plasmids produced 2 bands. The expected band sizes are: SW8-IRL1620 (8281 bp), Flex Switch (9501 bp), RF dsDNA (7675 bp), and ssDNA (3837 bp), the resulted bands matched the sizes for the precursor and helper plasmids. The absence of RF dsDNA and ssDNA doesn't necessarily mean that there is a problem with miniphagemids since the presence of those intermediate forms depends on where cells are in the miniphagemid production cycle.

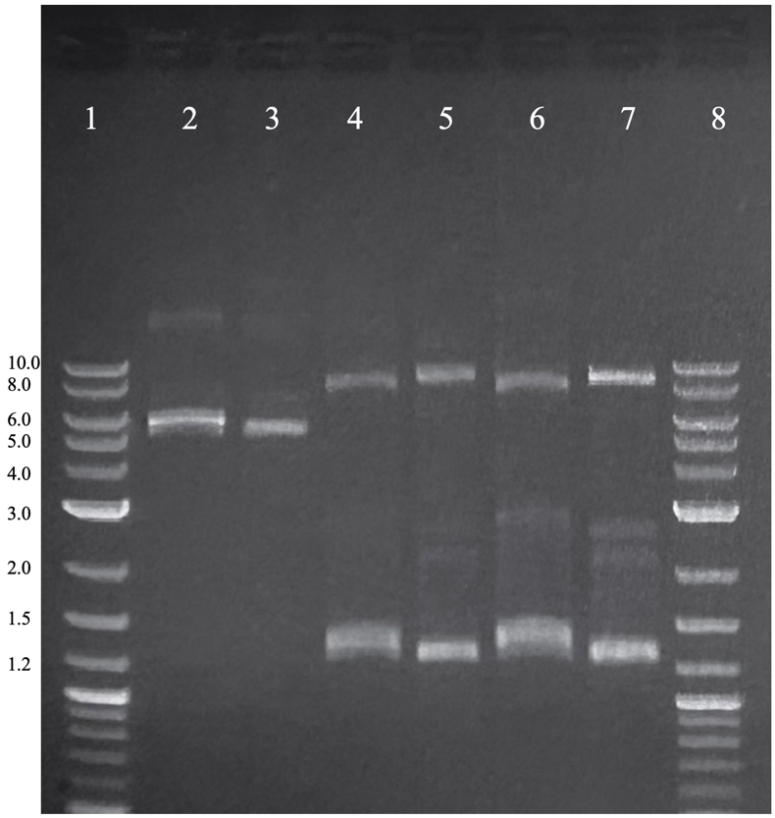


Figure 37: Agarose Gel of Restriction Digest of Flex Switch with SW8-EGF and Flex Switch with SW8-IRL1620 Plasmid DNA for Miniphagemid Production

DNA extracted from cells co-transformed with Flex Switch precursor plasmid (along with the SW8-EGF as well as SW8-IRL1620 helper plasmids) was digested using XhoI RE and subsequently run on a 0.8% agarose gel for 1hr and 30 min.
Lane 1&8: 1kb plus DNA Ladder labelled in kb.
Lane 2: undigested p326, lane 3: p326 digested with XhoI.
Lane 4: undigested Flex Switch with SW8-EGF, lane 5: Flex Switch with SW8-EGF digested with XhoI.
Lane 6: undigested Flex Switch with SW8-IRL1620, lane 7: Flex Switch with SW8-IRL1620 digested with XhoI.

Figure 38 illustrates AGE results for digested JL with SW8-SF, SW8-SG, and SW8-SL plasmids. The assay confirmed the expected sizes for the precursor and helper plasmids. pJL1 with SW8-SF plasmids produced multiple bands. The expected band sizes are: SW8-SF (8.3 kbp), pJL1 (8.9 kbp), RF dsDNA (7.1 kbp), and ssDNA (3.5 kb), the resulted bands matched the sizes for the precursor and helper plasmids. Similarly, pJL2 with SW8-SF produced multiple bands. The expected band sizes are: SW8-SF (8.3 kbp), pJL2 (7.7 kbp), RF dsDNA (5.9 kbp), and ssDNA (2.9 kb), the resulted bands approximately matched the sizes for the precursor and helper plasmids. pJL3 with SW8-SF also produced multiple bands. The expected band sizes are: SW8-SF (8.3 kbp), pJL3 (7.7 kbp), RF dsDNA (5.9 kbp), and ssDNA (2.9 kb), the resulted bands approximately matched the sizes for the precursor and helper plasmids, since there could be an overlap between the bands produced by the precursor and helper plasmids due to the similarity in their sizes. pJL1, pJL2, and pJL3 with SW8-SG also produced multiple bands. The expected band size for SW8-SG is 8.4 kbp, the same as for SW8-SF since the only difference between the 2 plasmids is the peptide that will be displayed on the capsid protein pIII. The display peptides SF, SG, and SL are 8-mers (consist of 8 amino acids) resulting in no difference in the helper plasmid sizes. Sizes for the pJL1, pJL2, and pJL3 also remain unchanged. The results have showed that produced bands approximately matched the sizes for the precursor and helper plasmids. pJL1, pJL2, and pJL3 with SW8-SL produced between 1 to 2 bands. Again, it is possible that the helper and precursor plasmid DNA has overlapped due to similarity in sizes, this could explain why some lanes have only 1 visible band. These results differ from the previous two sets of precursor-helper combos. It is unclear why the band number is lower but could be due to insufficient RF DNA and ssDNA present in the sample to be visible on the gel. The absence of RF dsDNA and ssDNA doesn't necessarily mean that there is a problem with miniphagemids since the presence of those intermediate forms depends on where cells are in the miniphagemid production cycle. In addition, traditional DNA

extraction methods in microbiology are optimised for dsDNA isolation, suggesting that ssDNA could get washed away during the DNA purification process.

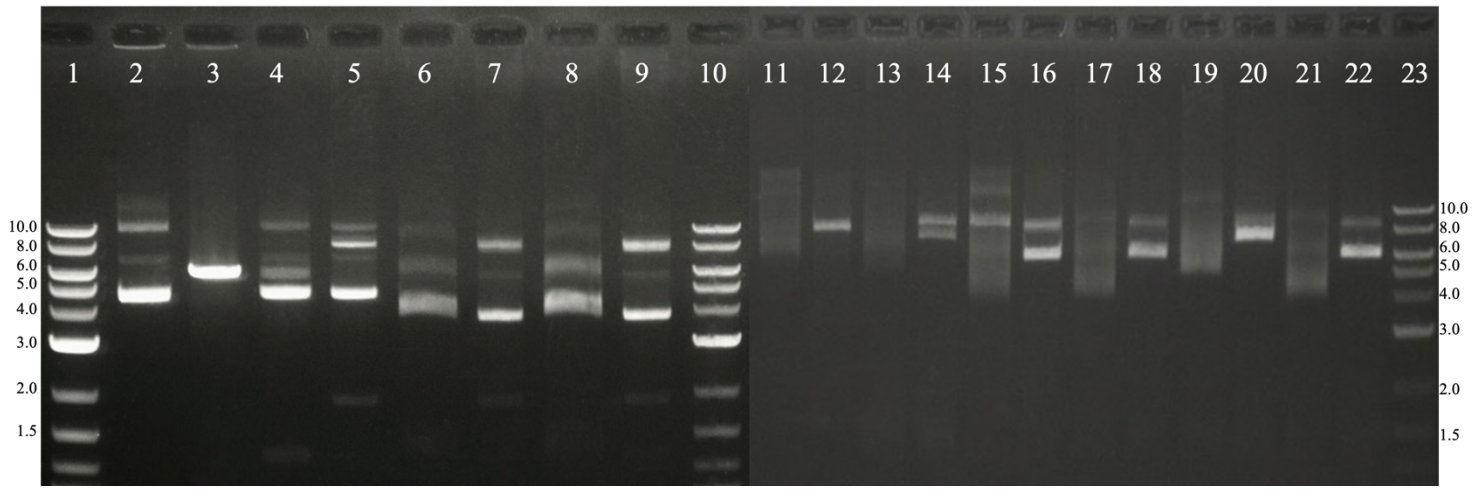


Figure 38: Agarose Gel of Restriction Digest of JL with SW8-SF, SW8-SG and SW8-SL Plasmid DNA for Miniphagemid Production

DNA extracted from cells co-transformed with pJL1, pJL2, and pJL3 precursor plasmids (along with the SW8-SF, SW8-SG, and SW8-SL helper plasmid) was digested using HindIII-HF RE and subsequently run on a 0.8% agarose gel for 1hr and 30 min.
Lane 1, 10 & 23: 1kb plus DNA Ladder labelled in kb.
Lane 2: undigested p326, lane 3: p326 digested with HindIII-HF.
Lane 4: undigested pJL1 with SW8-SF, lane 5: pJL1 with SW8-SF digested with HindIII-HF.
Lane 6: undigested pJL2 with SW8-SF, lane 7: pJL2 with SW8-SF digested with HindIII-HF.
Lane 8: undigested pJL3 with SW8-SF, lane 9: pJL3 with SW8-SF digested with HindIII-HF.
Lane 11: undigested pJL1 with SW8-SG, lane 12: pJL1 with SW8-SG digested with HindIII-HF.
Lane 13: undigested pJL2 with SW8-SG lane 14: pJL2 with SW8-SG digested with HindIII-HF.
Lane 15: undigested pJL3 with SW8-SG, lane 16: pJL3 with SW8-SG digested with HindIII-HF.
Lane 17: undigested pJL1 with SW8-SL, lane 18: pJL1 with SW8-SL digested with HindIII-HF.
Lane 19: undigested pJL2 with SW8-SL, lane 20: pJL2 with SW8-SL digested with HindIII-HF.
Lane 21: undigested pJL3 with SW8-SL, lane 22: pJL3 with SW8-SL digested with HindIII-HF.

Figure 39 illustrates AGE results for digested JL with SW8-EGFSF plasmids. The assay confirmed the expected sizes for the precursor and helper plasmids. pJL1 with SW8-EGFSF plasmids produced 2 bands. The expected band sizes are: SW8-EGFSF (8.4 kbp), pJL1 (8.9 kbp), RF dsDNA (7.1 kbp), and ssDNA (3.5 kb), the resulted bands matched the sizes for the precursor and helper plasmids. Similarly, pJL2 with SW8-EGFSF produced 1 bold band. The expected band sizes are: SW8-SF (8.4 kbp), pJL2 (7.7 kbp), RF dsDNA (5.9 kbp), and ssDNA (2.9 kb), the results have approximately matched the sizes for the precursor and helper plasmids, since there could be an overlap between the bands produced by the precursor and helper plasmids due to the similarity in their sizes. pJL3 with SW8-EGFSF also produced 2 bands. The expected band sizes are: SW8-SF (8.4 kbp), pJL3 (7.7 kbp), RF dsDNA (5.9 kbp), and ssDNA (2.9 kb), the resulted bands approximately matched the sizes for the precursor and helper plasmids.

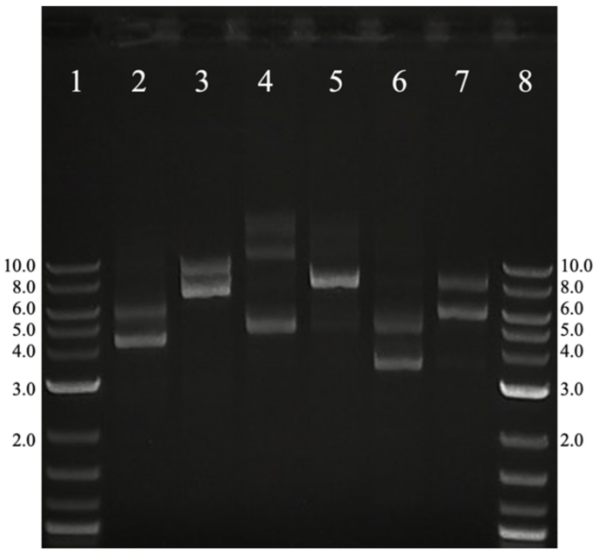


Figure 39: Agarose Gel of Restriction Digest of JL and SW8-EGFSF Plasmid DNA for Miniphagemid Production

DNA extracted from cells co-transformed with pJL1, pJL2, and pJL3 precursor plasmids (along with the SW8-EGFSF helper plasmid) was digested using HindIII-HF RE and subsequently run on a 0.8% agarose gel for 1hr and 30 min.
Lane 1 & 8: 1kb plus DNA Ladder labelled in kb.
Lane 2: undigested pJL1 with SW8-EGFSF, lane 3: pJL1 with SW8-EGFSF digested with HindIII-HF.
Lane 4: undigested pJL2 with SW8-EGFSF, lane 5: pJL2 with SW8-EGFSF digested with HindIII-HF.
Lane 6: undigested pJL3 with SW8-EGFSF, lane 7: pJL3 with SW8-EGFSF digested with HindIII-HF.

Figure 40 illustrates AGE results for digested pLuNe with SW8-SF plasmids. pLuNe with SW8-SF plasmids produced 1 visible band. The expected band sizes are: SW8-SF (8.3 kbp), pLuNe (8.1 kbp), RF dsDNA (6.2 kbp), and ssDNA (3.1 kb). The observed results could be explained through the overlap of DNA fragments. Similarly, pLuNe with SW8-SG also produced 1 band. The expected band size for SW8-SG is 8.3 kbp the results have approximately matched the sizes for the precursor and helper plasmids. pLuNe with SW8-SL also produced 1 band. The expected band size for SW8-SL is 8.3 kbp, the resulted bands approximately matched the sizes for the precursor and helper plasmids. There was absence of RF dsDNA and ssDNA which could be due to insufficient amounts of those DNA types in the digested sample.

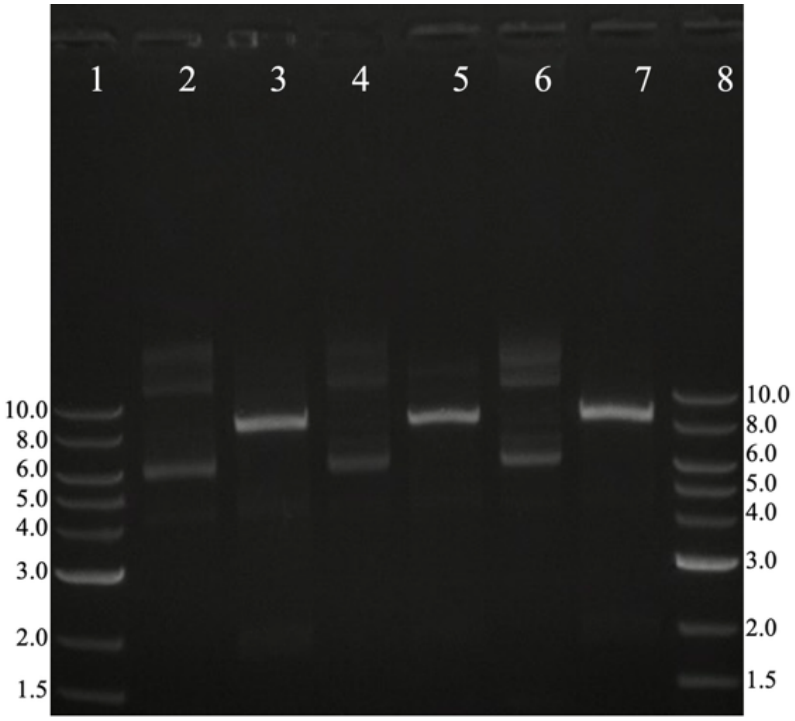


Figure 40: Agarose Gel of Restriction Digest of pLuNe with SW8-SF, SW8-SG, and SW8-SL Plasmid DNA for Miniphagemid Production

DNA extracted from cells co-transformed with pLuNe precursor plasmids (along with the SW8-SF, SW8-SG, SW8-SL helper plasmids) was digested using PvuI-HF RE and subsequently run on a 0.8% agarose gel for 1hr and 30 min.
Lane 1 & 8: 1kb plus DNA Ladder labelled in kb.
Lane 2: undigested pLuNe with SW8-SF, lane 3: pLuNe with SW8-SF digested with PvuI-HF.
Lane 4: undigested pLuNe with SW8-SG, lane 5: pLuNe with SW8-SG digested with PvuI-HF.
Lane 6: undigested pLuNe with SW8-SL, lane 7: pLuNe with SW8-SL digested with PvuI-HF.

Appendix E: Assessing DNA Uptake by A7 Cells During Transfection Through PI Staining

Since observed transfection efficiencies in A7 cells were quite low (usually <10%), an additional experiment was performed to determine whether this was due to inefficient plasmid DNA uptake or poor gene expression. To address this, pLuNe plasmid encoding the mNeonGreen reporter gene, was stained with PI dye prior to transfection to allow direct visualization of DNA internalization independent of the gene expression. Lipofectamine was used as the transfection reagent to form DNA-Lipofectamine-PI complex. In this experiment, detection of red PI fluorescence within the cells without green mNeonGreen signal would indicate that DNA was successfully taken up but not expressed. In addition, untreated PI-stained cells were using as a control to account for naturally dead or compromised cells that could take up unbound PI dye.

In order to form DNA-Lipofectamine-PI complexes 150ng of pLuNe DNA was transferred into a microcentrifuge tube and combined with 0.15 µL of Lipofectamine 3000 Reagent and 0.10 µL of the Enhancer Reagent, P3000. The mix was then incubated for 10-15 min to allow for Lipofectamine-DNA complexes to form. Then, 1-2 µL of PI dye was added to each DNA sample and mixed gently. Samples were incubated for 15 min at room temperature in the dark and combined with 10% FBS DMEM and added to the wells pre-seeded containing A7 cells. The plate was gently swirled for even distribution and incubated at 37 °C + 5% CO_2 for 24 h until transfection efficiency evaluation with flow cytometry where PI was detected using PE channel and mNeonGreen was detected using a FITC (Fluorescein Isothiocyanate) channel.

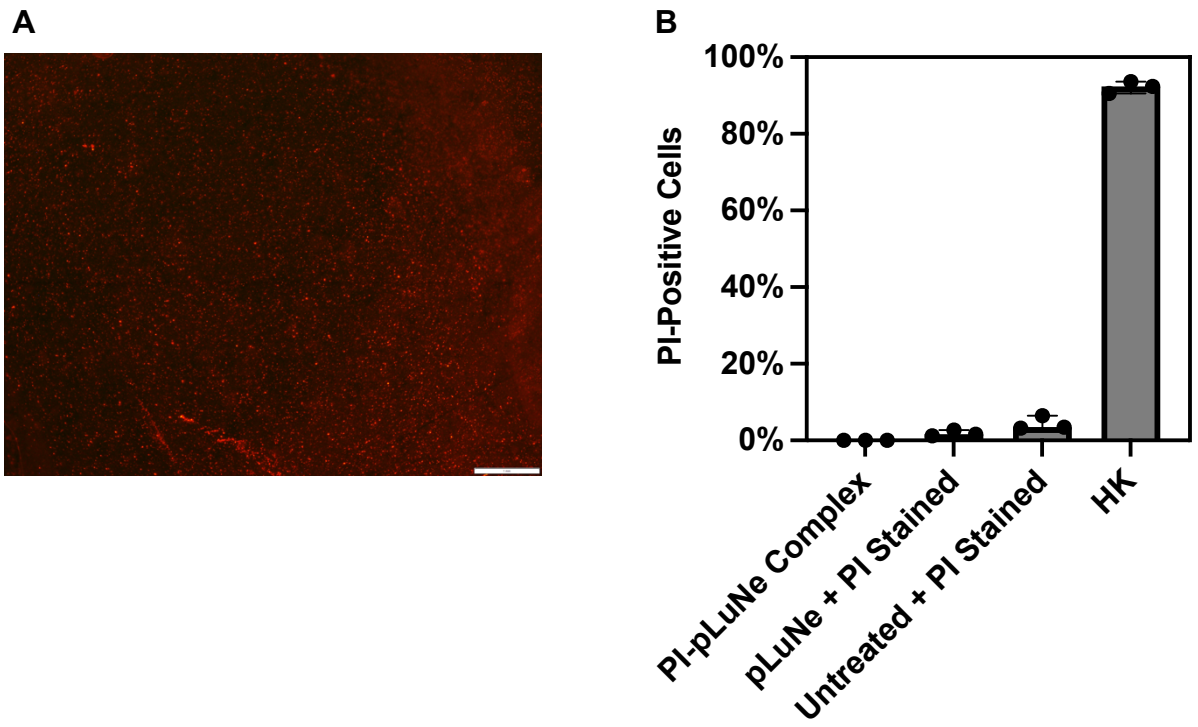


Figure 41: Assessing DNA Uptake by A7 Cells Through PI-Staining

DNA-Lipofectamine-PI complexes viewed using fluorescence microscope with a TRITC (Tetramethylrhodamine) filter at 40X magnification (A). Quantification of intracellular PI fluorescence following transfection of A7 cells with PI-stained pLuNe plasmid DNA using Lipofectamine (n = 3). Negative control cells showed ≤1% PI-positive cells and are not shown. Data are presented as data points with bars at the median percentage of fluorescent cells.

Quantification of PI-positive cells showed very little PI-stained pLuNe DNA present in A7 cells, while heat killed cells showed strong PI signal due to loss of membrane integrity. Low levels of PI fluorescence were also observed in untreated PI-stained controls, suggesting little background signal from membrane compromised cells. The lack of detected PI signal in live A7 cells does not indicate that plasmid DNA was not taken up in other transfection experiments. Rather, this outcome is most likely due to an expected limitation of the approach, as propidium iodide is membrane-impermeable and therefore unable to enter healthy cells. It was hypothesised that in combination with transfection reagent PI-stained DNA would be able to enter the cell, potentially showing that DNA uptake does happen in A7. However, this was not the case. As a result, this assay cannot be used to assess DNA uptake in live cells, and no conclusions can be drawn regarding whether

plasmid DNA internalization has occurred. Instead, these results highlight the limitation of PI as a DNA-labeling dye for uptake studies and emphasize the need for alternative labeling strategies compatible with live-cell transfection.